Charge Carrier Transport and Photogeneration at Very High Electric Fields in Amorphous Selenium

Nour Hijazi

A Thesis

In the Department

of

Electrical and Computer Engineering

Presented in Partial Fulfillment of Requirements

For the Degree of

Doctor of Philosophy (Electrical and Computer Engineering) at

Concordia University

Montreal, Quebec, Canada

December 2017

CONCORDIA UNIVERSITY

SCHOOL OF GRADUATE STUDIES

This is to certify that the thesis prepared

By: Nour Hijazi

Entitled: Charge Carrier Transport and Photogeneration at Very High Electric Fields
                in Amorphous Selenium

and submitted in partial fulfillment of the requirements for the degree of

                Doctor Of Philosophy (Electrical & Computer Engineering)

complies with the regulations of the University and meets the accepted standards with respect to
originality and quality.

Signed by the final examining committee:

_____Chair
Dr. Zhenhua Zhu

_____ External Examiner
Dr. Stephen K. O'Leary

_____ External to Program
Dr. Anjan Bhowmick

_____ Examiner
Dr. Mojtaba Kahrizi

_____ Examiner
Dr. Pouya Valizadeh

_____Thesis Supervisor
Dr. M. Zahangir Kabir

Approved by
            Dr. Wei-Ping Zhu, Graduate Program Director

 Friday, February 2, 2018   _____
                        Dr. Amir Asif, Dean
                         Faculty of Engineering and Computer Science

ABSTRACT

Charge Carrier Transport and Photogeneration at Very High Electric Fields in Amorphous Selenium

Nour Hijazi, Ph.D.
Concordia University, 2017

The flat-panel digital X-ray detectors (e.g. amorphous selenium, a-Se, based detectors) are replacing the film-based technology in various diagnostic medical imaging modalities such as mammography and chest radiography. Whereas, there is a huge demand for lowering the irradiation dose in various medical imaging modalities, the present flat-panel digital X-ray imaging technology is severely challenged under low dose conditions. To date, amorphous selenium (a-Se) is one of the most highly developed photoconductors used in digital X-ray imaging, which exhibits impact ionization and usuable carrier multiplication. The viability of avalanche multiplication can increase the signal strength and improve the signal to noise ratio for application in low dose medical X-ray imaging detectors. In spite of the interesting outlook of a-Se, some of its fundamental properties are still not fully understood. Specifically, an understanding of carrier transport at extremely high field in a-Se is in a very premature state. Therefore, an extensive research work is vital to clearly understand the fundamental underlying physics of carrier generation, multiplication, and transport mechanisms in a-Se.

In this dissertation, a physics-based model is developed to investigate the mechanisms of the electric field and temperature dependent effective drift mobility of holes and electrons and also the impact ionization in a-Se. The models consider the density of states distribution near the band edges, field enhancement release rate from the shallow traps, and carrier heating. The lucky-drift model for a-Se is developed based on the observed field dependent microscopic mobility. The validation of the developed models via comparison with the experimental data verifies the mechanisms behind the electric field and temperature dependent behaviours of impact ionization coefficient in a-Se. The density of state function near the band edges,

consisting of an exponential tail and a Gaussian peak, successfully described the electric field and temperature-dependent effective drift mobility characteristics in a-Se.

The photogeneration efficiency in a-Se under optical excitation strongly depends on photon wavelength and electric field. A physics-based model is proposed to investigate the physical mechanism of charge carrier photogeneration in a-Se under high electric fields. The exact extension of Onsager theory can explain the photogeneration efficiency in a-Se at extremely high electric field.

The mechanism of carrier recombination following X-ray excitation and hence the evaluation of electric field and X-ray photon energy dependent electron-hole pair (EHP) creation energy (amount of energy needed to produce a detectable free EHP upon the absorption of an X-ray photon) in a-Se have been topics of a very vital debate over the last two decades. These issues are addressed in this thesis. Towards this end, a physics-based analytical model is developed via incorporating a few valid assumptions to study the initial recombination mechanisms of X-ray generated EHPs in a-Se. The analytical model is later verified by a full phase numerical model, considering three-dimensional coupled continuity equations of electrons and holes under carrier drift, diffusion and bimolecular recombination. The corresponsding calculations of EHP creation energy with wide variations of X-ray energy, electric field and temperature are verified with respect to the available published experimental data. According to this, it is found that the columnar recombination model is capable of describing the electric field, temperature and photon energy dependent EHP creation energy in a-Se for high-energy photons.

The theoretical work of this thesis unveil the physics of the charge carrier transport and photogeneration mechanisms in a-Se at very high electric fields, which is vital to optimum design of avalanche a-Se detectors. This work will also provide a guideline for further improvement of the radiation imaging detectors.

ACKNOWLEDGEMENTS

TABLE OF CONTENTS

LIST OF FIGURES

LIST OF TABLES

LIST OF ABBREVIATIONS

Abbreviation		Description
α-Se	-	α-monoclinic Selenium
A/D	-	Analog to digital
AMA	-	Active matrix array
AMFPI	-	Active matrix flat panel imager
a-Se	-	Amorphous selenium
a-As$_2$Se$_3$	-	Amorphous arsenic triselenide
a-Si:H	-	Hydrogenated amorphous silicon
As	-	Arsenic
CdSe	-	Cadmium selenide
CB	-	Conduction band
Cl	-	Chlorine
CMOS	-	Complementary metal oxide semiconductor
DECs	-	Deviant electron configurations
DOS	-	Density of states
EHP	-	Electron-hole pair
γ-Se	-	Trigonal selenium
Ge	-	Germanium
HARP	-	High-gain avalanche rushing photoconductor
HDTV	-	High definition television
HgI$_2$	=	mercuric iodide
ITO	-	Indium tin oxide
IVAP	-	Intimate valence alternation pair
keV	-	Kilo electron volt
kVp	-	Kilo volt peak
LD	-	Lucky drift
LP	-	Lone pair
meV	-	Milli electron volt
NB	-	Nonbonding

NH	-	Noolandi Hong
NSB	-	Normal structure bonding
PPM	-	parts per million
PbI_2	-	Lead Iodide
PbO	-	lead oxide
Poly-PbO	-	polycrystalline lead oxide
RIL	-	Resistive Interface layer
Si	-	Silicon
SNR	-	Signal to noise ratio
TOF	-	Time of flight
TFT	-	Thin film transistor
VAP	-	Valence alternation pair
VB	-	Valence band

LIST OF SYMBOLS

Symbol		Description
α_h	-	Impact ionization coefficient for holes
α_{at}	-	Linear attenuation coefficient
a_{eff}	-	Effective tunnelling distance
a_r	-	reaction radius
b_g	-	Radius of the gaussian distribution
C_t	-	Capture coefficient of holes
C_r	-	Recombination coefficient
C_L	-	Langevin recombination coefficient
C_0	-	Recombination coefficient constant value
D	-	Diffusion coefficient of charge carriers
d	-	Column length
ΔE_m	-	Standard deviation of the gaussian curves
δE_i	-	Change in potential barrier
ε_0	-	Permittivity of vacuum
ε_r	-	Relative permittivity
E_g	-	Band-gap energy
E_c	-	Energy of conduction band edge
E_v	-	Energy of valence band edge
E_f	-	Energy of Fermi level
E_t	-	Energy depth of the shallow traps from E_v
E	-	Energy of X-ray photon
E_{phonon}	-	Average phonon energy loss
E_m	-	Peak Energy
E_i	-	Ionization threshold energy
$E^{\grave{}}$	-	Vibration energy
E_p	-	Optical phonon energy
e_{n0}	-	Emission rate without field
e	-	Elementary charge

φ	-	Dissociation efficiency
F	-	Electric field
F_{th}	-	Avalanche multiplication threshold electric field
$g(E)$	-	Density of states at energy E
g_v	-	Density of states at the valence band edge
g_c	-	Density of states at the conduction band edge
$\hbar$	-	Modified Plank constant
h	-	Plank constant
k_B	-	Boltzmann constant
λ	-	Wavelength
λ_m	-	Momentum relaxation mean free path
$\lambda_m(0)$	-	Zero-field momentum relaxation mean free path
λ_E	-	Energy relaxation mean free path
λ_{op}	-	Optical phonon mean free path
L	-	Layer thickness
l_0	-	Electron mean free path
M_a	-	Number of rows in the active matrix array
m_0	-	Free electron mass
m^*	-	Effective mass of the carrier
η	-	Photogeneration efficiency
η_0	-	Production efficiency
η_{cc}	-	Charge collection efficiency
N_a	-	Number of columns in the active matrix array
N_t	-	Shallow trap concentration
N	-	Number of electron-hole pairs
N_m	-	Peak value of shallow traps
$N(E)$	-	Density of states of a-Se at energy E
N_0	-	Ionization line density
θ_r	-	Mobility reduction factor
θ	-	Angle fromed by the separation of an electron and hole
ρ	-	Material density

p_{free}	-	Concentration of carriers in the transport band
$p_{trapped}$	-	Concentration of carriers occupying shallow traps
p	-	Reduced reactivity parameter
Q	-	Collected charge
$R\,(F)$	-	Field enhancement release rate
r_0	-	Initial separation of a geminate electron and hole
r_c	-	Onsager length
τ	-	Carrier lifetime
τ_e	-	Electron lifetime
τ_h	-	Hole lifetime
τ_{av}	-	Average phonon scattering time
T	-	Absolute Temperature
T_{eff}	-	Effective Temperature
T_r	-	Room Temperature
T_0	-	Characteristic Temperature
t	-	Time
μ	-	Effective drift mobility
μ_e	-	Electron mobility
μ_h	-	hole mobility
μ_0	-	Microscopic mobility
ν	-	Frequency of the incident optical photon
ν_r	-	Recombination frequency
ν_{th}	-	Thermal frequency
ν_p	-	Phonon frequency
ν_0	-	Attempt to escape frequency
v_s	-	Sound velocity
V	-	Interaction potential
W_{ehp}	-	Average energy needed to create a single free electron hole pair
W_0	-	Average energy needed to create an electron hole pair
$W\,(r,\,t)$	-	Probability density function
Y	-	Charge extraction yield

Z   -   Atomic number

Chapter

1. Introduction

1.1 Overview

Solids in terms of regularities in their atomic structure are broadly categorized into three groups: *crystalline, polycrystalline* and *amorphous*. Crystalline materials are solids in which atoms are arranged in a perfect periodic order throughout the solid. Whereas, polycrystalline materials are composed of many small crystals known as grains that are randomly oriented in different directions. On the other hand, amorphous materials are the ones in which the constituent atoms lack such periodicity. Their lattice structure contains some deviations from the perfect periodic lattice arrangement that acts to destroy the overall periodicity of the solid.

The theory of quantum mechanics was developed in the 1920s and 1930s. The theory was readily applied to the study of crystalline solids due to the mathematical simplifications that resulted when dealing with periodic structures. This resulted to the development of many crystalline-based electronic devices. One of the most prominent inventions was the solid-state transistor, which literally revolutionized electronic devices. Amorphous materials, on the other hand did not experience the same rapid growth due to the complexities of applying quantum mechanical models to non-periodic structures. For a long period of time, amorphous materials were not considered to behave as semiconductors, although experimental facts proposed otherwise. In mid-1950s, amorphous semiconductors were considered as an era of growth in the microelectronics industry [1].

One of the main motivations for research on amorphous semiconductors has been and still is, the economical preparation of these materials in large areas for applications such as displays, scanners, solar cells, image sensors, and other similar large area applications. This fact

provides amorphous semiconductors a tremendous economical advantage over their crystalline counterparts. This is since the preparation of amorphous solids does not usually require the same careful control over the growth conditions.

Diagnostic radiography is an area where amorphous semiconductors are poised to make a tremendous impact. In the next section, the development of radiography and how amorphous semiconductors are used and the impact they are having in this field will be described.

1.2 Radiographic Imaging

The discovery of X-ray approximately 100 years ago by Wilhelm Roentgen lead very quickly to the development of radiology and medical imaging. Radiographic imaging still remains as one of the most useful diagnostic tools aiding the physicians. Although radiography is one of the most common medical diagnostic tools, it remains largely a film based, analog technology, especially in developing countries. Imaging techniques have undergone widespread changes resulting from the combination of new X-ray imaging methods with powerful computers, hardware for displaying high-resolution images, and lower expensive mass storage devices. Digital imaging modalities such as MRI and ultrasound are replacing the film-based systems since they result in higher resolution images to be obtained than conventional film-screen combinations. A digital radiographic system can monitor the quality of the image, adjust the exposure settings as required, and display the image right after the X-ray exposure on a display monitor. Moreover, the digital image files may be stored on centralized file servers and shared over computer networks, where specialists who are offside can analyze them [2].

Extensive research has shown that the self-scanned active matrix array (AMA) based flat panel X-ray image detector is the most promising digital radiographic medium for replacing the conventional X-ray film/screen cassettes in diagnostic X-ray imaging (e.g. mammography, chest radiography and fluoroscopy) [3, 4]. The flat panel displays are also called active matrix arrays due to the fact that active devices, i.e. thin-film transistors (TFT) or complementary metal oxide semiconductor (CMOS), are arranged in arrays forming a large matrix. The physical form of active matrix flat panel imagers (AMFPI) that incorporates active matrix arrays are similar to a film/screen cassette and hence easily fit into current medical X-ray systems. The dynamic range

of the AMFPI systems is much higher than the film/screen imaging systems, where they are able to read out an entire image in 1/30 seconds, sufficient to perform fluoroscopy [5, 6].

1.3 Flat-panel detectors

The AMFPI concept is illustrated in Figure 1-1, where a flat panel X-ray image detector is used instead of the film-screen cassette that converts the incident X-ray photons into an electrical signal, which is digitized by an analog to digital (A/D) converter and finally recorded on a digital memory. In general, a high-energy radiation that is partly transmitted through the body and partly absorbed in the irradiated object provides an image of the interior of the body. The patient is placed between the radiation source and the detector will acquire the image [7].
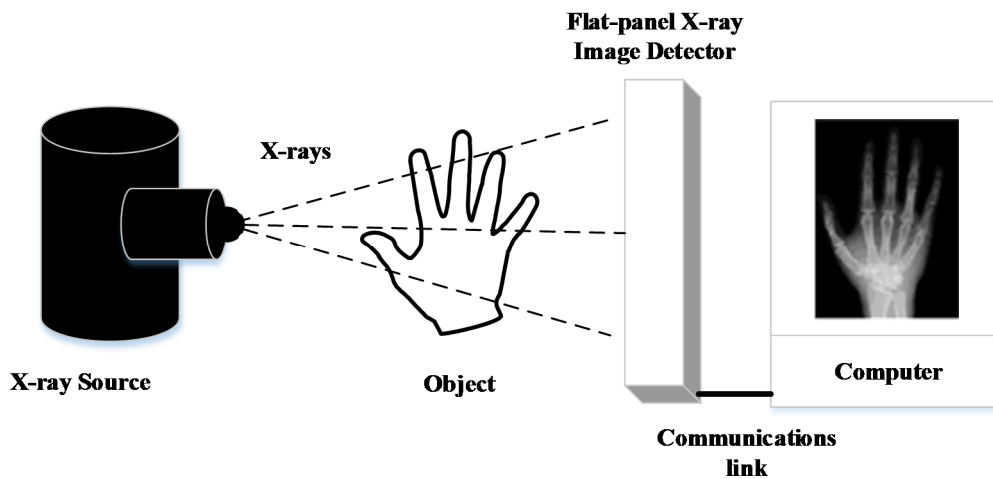
Figure 1-1 Schematic illustration of a flat panel X-ray image detector [7].

1.3.1 Indirect conversion detector

There are two general approaches in digital X-ray radiography. The first approach is a phosphor-based technique where a phosphor screen is coupled to a photo-detector and a storage capacitor [8]. In this setting the digitization of the signals acquired from the storage capacitor is performed to provide an instant readout. This type of detection is referred to as indirect conversion, since the electronic signal is indirectly generated from the pattern of visible light given off when X-rays strike the phosphor screen. The structure of an indirect conversion X-ray image sensor is illustrated in Figure 1-2. The bottom metallic contact is chromium. This is followed by a ~ 10 to 50 nm thick n^+ blocking layer, a ~ 0.5 to 1.0 μm thick intrinsic

hydrogenated amorphous silicon (a-Si: H) layer, a ~ 10 to 20 nm thick p^+ µc-$Si_{1-x}C_x$: H blocking layer, a ~ 50 nm layer of transparent indium tin oxide (ITO), and finally a surface passivation layer of oxy-nitride (a mixture of silicon oxide and silicon nitride phase: SiO_xN_y). The term passivation denotes the process of chemically or physically protecting a semiconductor surface from degradation.
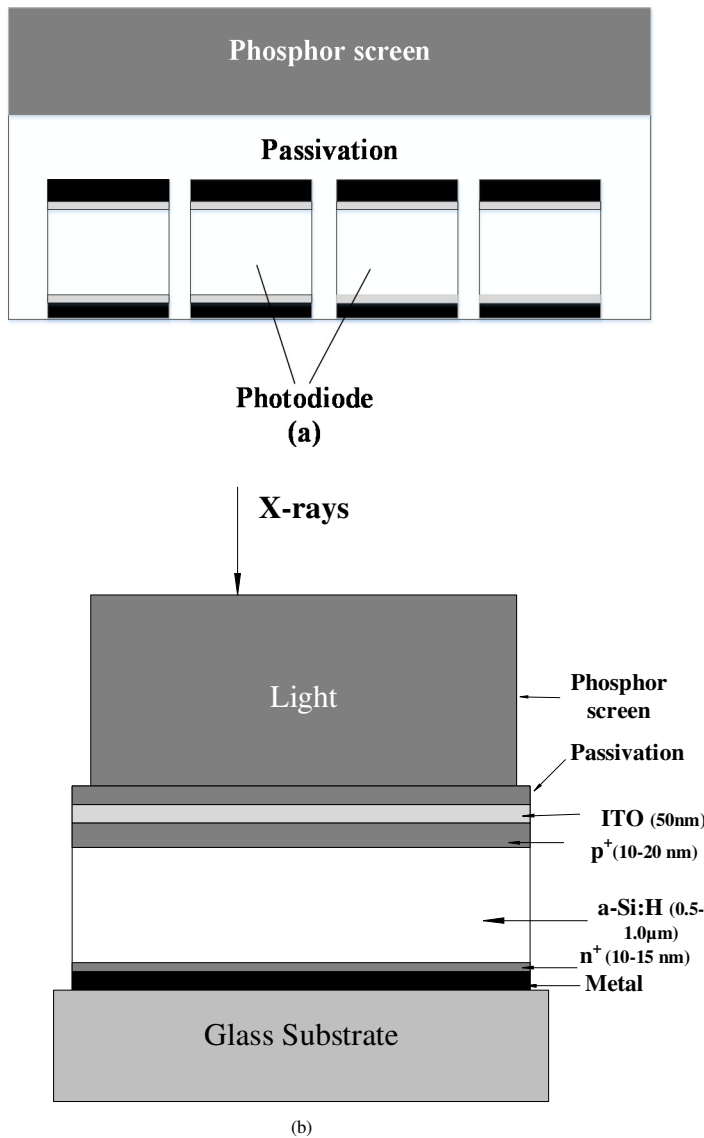
Figure 1-2 a) A simplified cross-section of an indirect conversion X-ray image detector. Photodiodes are arranged in a two-dimensional array. (b) A cross-section of an individual hydrogenated amorphous silicon (a-Si: H) P-I-N photodiode. The phosphor screen absorbs X-ray photons and creates visible light. These visible lights create electron-hole pairs in a-Si: H layer and the charge carriers are subsequently collected [3].

It has been found that the indirect conversion technique lacks the possibility of providing high image resolution compared to the second approach, which is based on the so called a direct conversion technique [9]. The systems based on direct conversion technique have now become one of the most promising digital radiographic systems. The term direct refers to the fact that the electrical charge carriers are directly generated in the photoconductor layer by the incident X-ray photons.

1.3.2 Direct conversion detector

Direct conversion flat panel X-ray detectors offer the promise of revolutionizing the field. Rowlands and co-workers [4] widely discussed in the literature this digital radiographic system. This direct conversion detector contains a photoconductive material, such as amorphous selenium (a-Se), that converts the incident X-rays directly to electrical charge. This is achieved based on a large-area, thin-film transistor (TFT) active-matrix array (AMA) coupled with the X-ray photoconductive detector. A biasing voltage is applied to the electrodes of the detector to create an electric field across the photoconductor. In the photoconductor, the charge carriers are released due to the absorption of X-rays and then guided to the electrodes under the effect of the electric field having negligible lateral spreading, and hence resulting in higher resolution.

In a flat panel X-ray photodetector, a large bandgap (> 2 eV), high atomic number semiconductor or X-ray photoconductor (e.g. amorphous selenium, a-Se) layer is used to coat the active matrix array in order to serve as a photoconductor layer as shown in Figure 1-3 [10]. An electrode is then deposited on top of the a-Se layer to enable the application of a positive bias potential, which will create an almost uniform electric field F across the photoconductor layer. Upon irradiation, the photoconductor absorbs the X-rays and the generated electron-hole pairs (EHPs) travel along the field lines and are collected by the electrodes. Electrons are collected by the positive electrode, labeled here as A_e, and holes are accumulated in the storage capacitor C_{ij} attached to the pixel electrode, and thereby providing a charge-signal Q_{ij} that can be read during self-scanning. The pixel capacitance C_{ij} is chosen to be much larger than the capacitance of the photoconductor layer on each pixel, so that most of the applied voltage drops across the photoconductor. Each pixel electrode accumulates an amount of charge Q_{ij} that is proportional to

the amount of incident X-ray radiation in the photoconductor layer over the given pixel area. To readout the latent image charge, Q_{ij}, the appropriate TFT is turned on every Δt seconds and the charge signal is transferred to the data line and hence to the charge amplifier. These signals are then multiplexed into serial data, digitized, and fed into a computer for producing an image [10, 11].
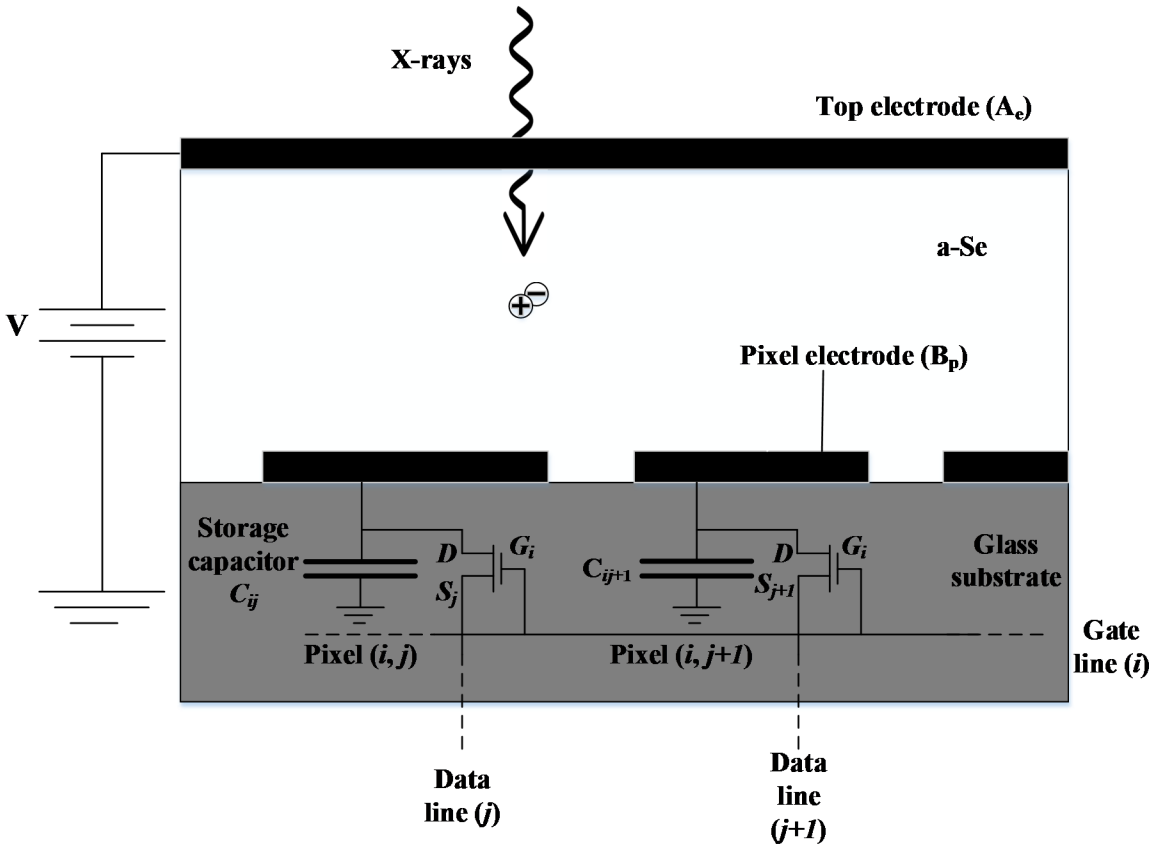
Figure 1-3 Cross sectional view of an a-Se direct conversion X-ray detector (exaggerated scale). Pixel size is typically $150 \, \mu$m $\times 150 \, \mu$m in size [10].

1.3.3 Active matrix readout

Large area integrated circuits or active matrix arrays have been developed as the basis for large area displays. Figure 1-4 is a simplified schematic of an AMA. In general, an AMA is based on $M_a \times N_a$ TFT based pixels, where M_a is the number of rows and N_a is the number of columns in the array. The gate terminals of each TFT in row i are connected to a control line,

and the source terminals in column *j* are connected to a common data line. All the TFTs in row *i* are turned on when the control line *i* is activated and the charge signal on each row capacitor is read out on the N_a data lines. Following this step, the parallel data streams are digitized, multiplexed, and transmitted to a computer. The charge read out is then continued to the next row till all the rows are covered.
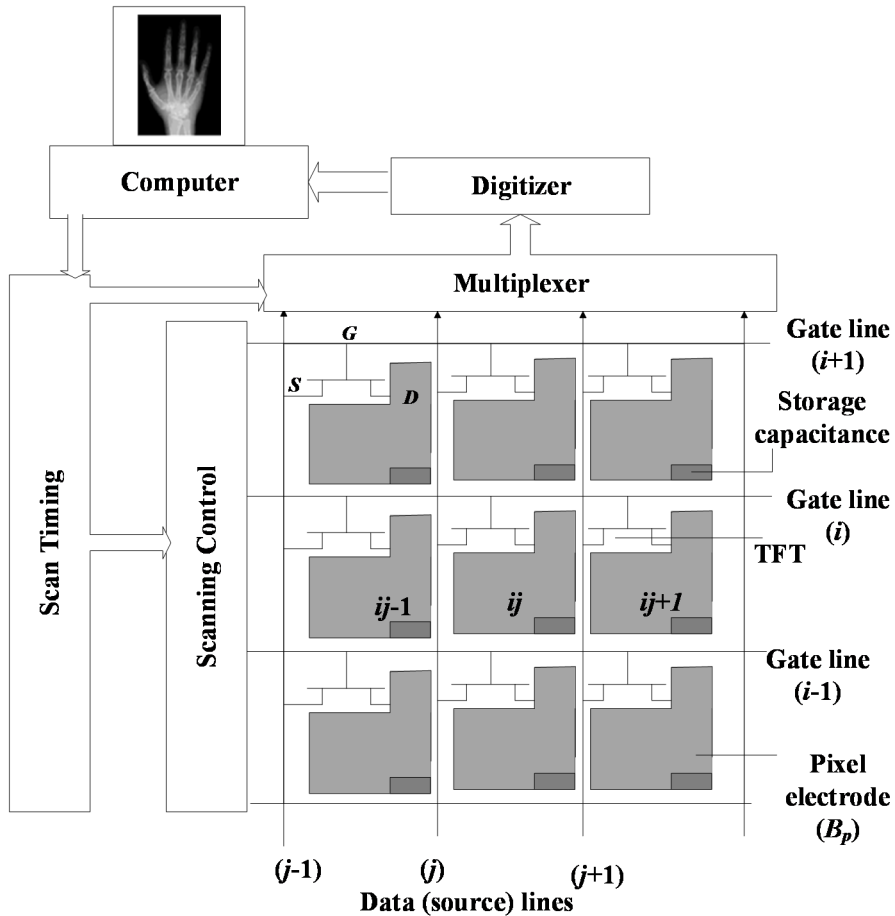
Figure 1-4 A thin film transistor (TFT) active matrix array (AMA) used in flat panel X-ray image detectors with self-scanned electronic readout [10].

1.3.4 General requirements of X-ray imaging systems

Any flat panel X-ray image detector design must first consider the required specifications based on the clinical need of the particular imaging modality, (e.g., mammography, chest radiography, and fluoroscopy). The combination of an a-Se layer and an AMA results in a

compact, self-scanning detector that is proper for radiographic imaging applications. The pixel dimensions determine the resolution in digital radiographic detectors, which is, at present, typically 200-250 µm for applications like chest radiography and fluoroscopy, and 50 µm for mammography [11]. Table 1-1 summarizes the specifications for flat panel detectors for chest radiography, mammography and fluoroscopy.

Table 1-1 Parameters for digital X-ray imaging systems. kVp is the maximum kV of bias applied across the X-ray tube during the time of duration of the exposure, and the maximum energy of the emitted X-ray photons is equal to the kVp value. (Data are taken from Rowlands and Yorkston [4]).

Clinical Task	Chest radiology	Mammography	Fluoroscopy
Detector size	35 cm × 43 cm	18 cm × 24 cm	25 cm × 25 cm
Pixel size	200 µm × 200 µm	50 µm × 50 µm	250 µm × 250 µm
Number of pixels	1750 × 2150	3600 × 4800	1000 × 1000
Readout time	~ 1 s	~ 1 s	1/30 s
X-ray spectrum	120 kVp	30 kVp	70 kVp
Mean exposure	300 µR	12mR	1 µR
Exposure range	30 – 3000 µR	0.6 – 240 mR	0.1 - 10 µR

1.3.5 Practical advantages of amorphous selenium X-ray Photoconductor

Amorphous selenium (a-Se) is a well-known photoconductor and has been used for a variety of applications, such as X-ray image detectors, and UV sensitive photodetectors [12]. One of its distinct advantages is that it can be easily coated as a thick film onto an AMA panel using conventional vacuum deposition techniques without the need to raise the substrate temperature beyond 60 - 70° C, which is well below the damaging temperature of the AMA (e.g., ~ 300°C for a-Si: H based TFTs). The resulting photoconductive layer exhibits an acceptable X-ray absorption coefficient, good electron and hole transport properties, and a small dark current compared with some of the competing polycrystalline materials, such as PbI_2 [11]. Hence, a-Se

is ideally suited for large area radiographic applications, such as chest radiography and mammography.

1.4 Avalanche multiplication phenomenon in amorphous semiconductors

The ability to acquire avalanche gain within a-Se is of high importance to the development of medical image sensors. Though impact ionization is a great often-observed phenomenon in crystalline materials, it is not very probable in amorphous materials. This is because of their short mean free path caused by frequent scattering. To date, a-Se remains one of the exceptional amorphous semiconductors where holes drifting at high electric fields can avoid excessive energy dissipation and thus can acquire enough energy in order to initiate impact ionization and secondary charge creation [13, 14].

In general, impact ionization at high electric fields results in avalanche multiplication, which depends exponentially on the photoconductor layer thickness. At very high electric fields, in a-Se, incident light/X-ray causes the generation of a primary electron-hole pair (EHP). The generated electron and hole will then drift in opposite directions and the holes will acquire enough energy from the field during its transit to create a secondary EHP due to an ionizing collision. Again, these secondary electrons and holes will drift in opposite directions and some of the holes will create new carriers as shown in Figure 1-5 [15]. This process is well known as impact ionization, and it will result in carrier multiplication and gain. Most materials have different electron and hole mobilities, hence the avalanche process is asymmetric and the probability of avalanche initiation is greater for one type of carrier. The higher mobility of holes in a-Se favours impact ionization for this kind of carrier. The hole impact ionization process in a-Se is shown in Figure 1-5. Impact ionization for holes starts at an electric field of 70 V/μm, whereas for electrons it starts at 115 V/μm.
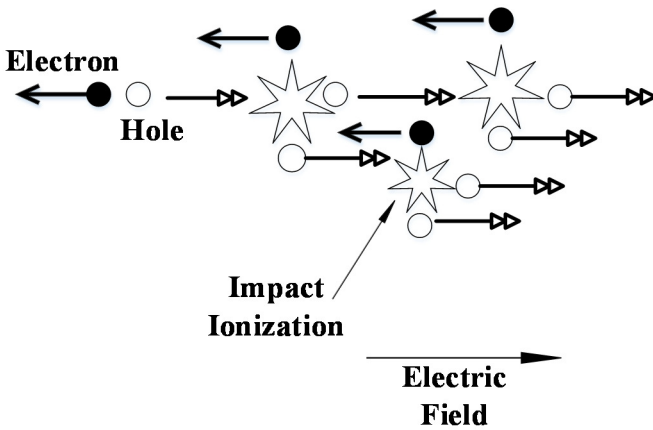
Figure 1-5 A schematic illustration of avalanche breakdown through impact ionization within the a-Se layer. One photogenerated hole results in many EHPs to be generated through impact ionization in the a-Se layer where a high electric field is applied.

Experiments on hole impact ionization within a-Se indicate that avalanche is initiated at electric fields exceeding a certain avalanche multiplication threshold, F_{th}. This threshold electric field is about 70 V/μm for an a-Se layer thicker than 15 μm, while F_{th} depends only slightly on the a-Se thickness. A a maximum avalanche gain of 1000 has been demonstrated for a 30 μm thick a-Se layer at a field of 92 V/μm [12]. The avalanche multiplication increases the signal strength and improve the signal to noise ratio (SNR) in low-dose X-ray imaging applications. The often used a-Se in photoconductor applications is usually alloyed with a small fraction of arsenic (As) to stabilize it against crystallization, and doped with a few parts per million (ppm) of chlorine (Cl) [16]. The signal strength increases and quantum noise decreases with increasing the applied electric field, which can improve the SNR monotonously below the threshold electric field for avalanche multiplication [17]. The excessive dark current has been one of the factors that limits the highest operating electric fields in X-ray photoconductors. An acceptable level of dark current up to the electric field as high as 70 V/μm in some detector structures has recently been reported [18].

Amorphous semiconductors have low carrier mobilities due to the random potential fluctuations in their structures. Hence, it is quite surprising that avalanche multiplication is actually observed in a-Se, and thus created some controversy at the time. It turns out that the impact ionization in a-Se can be explained by invoking the lucky drift (LD) model in which

carriers may be scattered by potential fluctuations, and hence, can still gain sufficient energy at high fields to cause impact ionization. Moreover, although the LD model clarifies the origin of avalanche multiplication in amorphous solids, it is still unclear why a-Se shows avalanche multiplication much more clearly than other amorphous materials, even among those with much narrower band gaps. For example, impact ionization seems much more probable in hydrogenated amorphous silicon (a-Si: H), since the charge carrier mobility in a-Si: H is much higher than that in a-Se and the amount of energy needed for ionization of secondary carriers in a-Si: H is lower than that in a-Se. Most attempts to reach avalanche multiplication in a-Si: H failed [19-21]. While in a-Se, F_{th} ~ 70 V/μm, F_{th} in a-Si: H was found to be above ~110 V/μm. The difference between F_{th} in a-Si: H compared to a-Se was contributed to the difference between the optical phonon energies (80 meV in a-Si: H and 31 meV in a-Se). Due to higher optical phonon energy in a-Si: H, the acquired energy from the electric field is almost totally lost by inelastic scattering processes [14]. Hence, the higher optical phonon energy in a-Si: H compared to a-Se is responsible for the less efficient gain of energy by the primary charge carriers in the electric field. In fact, the energy gain is impeded by the inelastic scattering processes. Thus, impact ionization and avalanche multiplication can be observed in a-Si: H only at much higher electric fields (above 110 V/μm) than in a-Se (about 70 V/μm) and therefore a-Si: H may not compete with a-Se for practical avalanche photodetectors.

1.5 High-gain avalanche rushing photoconductor (HARP) technology

The avalanche gain capability of a-Se photoconductors potentially provides practical solutions to a number of important applications in the field of medical image detectors, in as much as it promises to increase a-Se's X-ray to charge conversion efficiency and lead to a-Se detectors that are effectively quantum noise limited in operation at all exposure levels. A further advantage of avalanche multiplication is to increase the dynamic range of system by permitting the maximum signal capacity to be adjusted by changing the effective multiplication gain.
After the discovery of avalanche multiplication in a-Se in 1980, a highly sensitive optical image sensor, high-gain avalanche rushing photoconductors (HARP) optical image sensor has been developed and later commercialized [15]. a-Se HARP structures have been developed by NHK

in Japan as photoconductive targets of broadcast video cameras and are now used routinely for electronic gathering in high definition television (HDTV), i.e., operation at low light conditions [22]. In optical imaging application, a-Se HARP structures are deposited on a glass substrate covered with an ITO (indium tin oxide) coating that serves as a transparent anode. The back of the a-Se HARP structure is free which means, it has no physical electrode, thus a latent charge image will be formed (Figure 1-6). The scanning electron beam is used as a virtual cathode which will bias the free surface. The light photons that are incident on the front a-Se surface through a positively biased ITO electrode are absorbed, and thus, will create electron hole pairs (EHPs). The freed holes drift to the free surface of the a-Se layer, and if the electric field exceeds F_{th}, the drifting holes undergo avalanche multiplication. The holes accumulate as a latent charge image at the free surface in an amount proportional to the incident light intensity. An electron beam scans the free surface, completing the circuit, and enabling the accumulated positive charge to be sensed by the ITO electrode as a current.
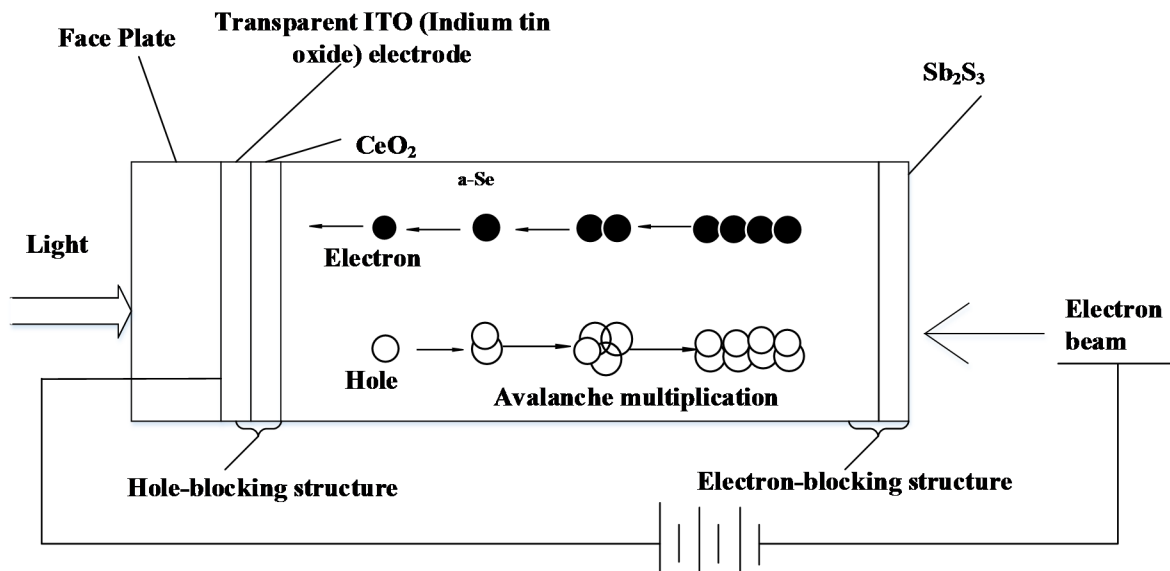
Figure 1-6 Diagram illustrating the principle of operation of a HARP camera tube. Optical photons create electron hole pairs in the a-Se layer. Holes undergo avalanche multiplication as they are swept through the layer under the influence of an electric field. A scanning electron beam is used to read out the resulting charge image on the free surface [14].

While the electron beam readout is compatible with HDTV, there has been an intense attempt to replace the electron beam of high-gain avalanche rushing photoconductors by a two-

dimensional array of pixel electrodes for low dose medical X-ray imaging [12]. Unfortunately, if metal electrodes are deposited directly on a HARP device, a dielectric breakdown occurs at the contact edges due to the local enhancement of the electric field. An incipient breakdown causes a high current flow that can induce irreversible damage of an area adjacent to the contact due to Joule heating. To overcome this problem with a modified HARP structure, a thin resistive interface layer (RIL) is introduced between the avalanche a-Se structure and the pixel electrodes. Recent work, carried out at Lakehead University and the Thunder Bay Regional Research Institute, showed that both the modified (with the RIL) and the original HARP devices exhibit almost identical charge transport, thus the RIL does not degrade the a-Se transport properties while enabling stable operation in the avalanche region without a full breakdown. Hence, modified a-Se HARP structures are considered to be the future of a-Se photodetectors in medical X-ray imaging in both direct conversion detectors for low energy applications, and in indirect conversion detectors for fluoroscopic applications [14, 23].

1.6 Motivation and literature review

In medical imaging, patient safety is considered of prime importance. The minimization of the patient exposure to radiation is highly required to achieve minimal biological damage. In addition, obtaining a good quality image with lowest expenses is another desirable objective. Hence, there is a huge demand for lowering irradiation doses for various medical imaging modalities, especially in general X-ray radiography and real-time imaging, such as fluoroscopy. This can be achieved by improving the overall detector performance.

After two decades of extensive research, a-Se based direct conversion X-ray detectors are commercialized for digital mammography [12]. However, the a-Se detector is not perfect where the main drawback of the conventional a-Se detector under normal operation (~10V/μm) is its low conversion gain (X-rays into free charge carrier generation) compared to other potential photoconductors, such as polycrystalline lead oxide (poly-PbO) or mercuric iodide (poly-HgI$_2$) [24], which reduces the signal to noise ratio in low-dose imaging (e.g., in fluoroscopy) and thus severely affects the diagnostic features of the image. One of the solutions to acquire very low-dose medical X-ray imaging could be achieved by utilizing a carrier multiplication process at a

very high electric field in the a-Se layer for higher charge signals. The avalanche multiplication of the signal improves the signal strength and improves the signal to noise ratio, which permits the lowering of the X-ray exposure/dose. However, developing a practical a-Se avalanche detector needs extensive research work to clearly understand the fundamental underlying physics of carrier generation, multiplication, and transport mechanisms.

Therefore, this research work is based on developing physics-based models to investigate the charge carrier generation, transport, and multiplication mechanisms in a-Se photoconductors. The investigation of the mechanisms of the photoconductive detector are based on analyzing the functionality of an a-Se detector at extremely high fields. The need for this investigation specifically at high fields rather than low fields is that hole transport at comparatively low electric field is controlled by trapping into localized states within the band tails. However, at high fields, in the avalanche regime, the probability of hole trapping is considered to be very low where the effective drift mobility saturates at 0.8 cm^2/Vs.

The research on avalanche a-Se solid state imaging detector is in a very premature level. Some of the most relevant scientific challenges are highlighted below.

a) Carrier transport at extremely high electric fields in a-Se

The optimum design of avalanche a-Se detector structures depends on an accurate understanding of the carrier transport mechanisms, impact ionization and carrier generation. In a-Se, the effective hole drift mobility at room temperature varies from 0.1 cm^2/Vs to 0.9 cm^2/Vs for the electric field variation of 10 V/μm to 100 V/μm [13]. The effective mobility of holes in a-Se increases with increasing electric field and temperature [25, 26]. The effective drift mobility is believed to be shallow trap-controlled and thermally activated [27]. The field enhancement of the release rate from the shallow traps, and hence, the increase of the effective mobility has been speculated to be due to either the thermally activated tunneling (TAT) or a Poole-Frenkel (PF) effect [28]. A debate which has not been resolved yet. Moreover, the exact mechanism of field dependent microscopic mobility is not clearly understood.

The lucky-drift model accurately describes the impact ionization mechanism in crystalline semiconductors. Rubel et al. [29] proposed a lucky-drift model to describe field-

dependent impact ionization coefficient of holes in a-Se by relating the momentum relaxation mean free path with the energy relaxation mean free path in the original lucky drift model of McKenzie and Burt [30]. However, the model assumed field-independent momentum relaxation mean free path and showed a stronger field dependence of impact ionization than the experimental observations [29]. The question still remains: what is the physics based model that can accurately describe the temperature and field dependent impact ionization in amorphous materials ? And, what are the exact mechanisms that can quantitatively describe the temperature and field-dependent drift mobility?

b) Carrier generation at extremely high electric fields in a-Se

In many semiconductors, a single EHP is created by an optical photon if the photon energy is higher than the bandgap energy of the photoconductor. The electron-hole pair will either escape under the influence of an applied electric field or it will recombine due to its mutual coulomb attraction. Therefore, one can define the photogeneration efficiency as the fraction of electron-hole pairs that do not recombine relative to all of the electron-hole pairs created. The photogeneration efficiency in some low dielectric constant semiconductors, such as a-Se, is less than unity and highly depends on the electric field, temperature and photon wavelength.

The photogeneration efficiency at moderate electric fields in a-Se has been most successfully described by the Onsager theory of dissociations [31]. The Onsager theory essentially calculates the probability that an EHP will diffuse apart for a given electric field F and temperature T. It has been shown that at longer wavelength of incident photon, the initial distance between carriers is smaller, which leads to smaller dissociation efficiency and as a result the quantum efficiency is lower. In the presence of an electric field, the probability of dissociation of electron-hole pairs increases, where higher photogeneration efficiency can be achieved at higher electric fields.

However, at strong F ($F > 50$ V/μm) and longer wavelength λ ($\lambda > 540$ nm), the conventional Onsager model gives considerably lower efficiency than the experimental values [32]. Onsager calculated the probability that a pair of oppositely charged ions separated by some

distance r_0 would escape recombination in the presence of their Coulomb attraction and an applied electric field. The Onsager model for the free carrier photogeneration efficiency assumed that the recombination between an electron and a hole occurs when their separation is zero.

The initial separation r_0 is taken as a fitting parameter in the conventional Onsager model. Knights and Davis [33] proposed a formulation for r_0, where r_0 increases with increasing the applied electric field. However, their model failed to explain the photogeneration efficiency in a-Se because of inaccuracy in calculating r_0. Hence, what should be the appropriate physics based model that can describe the exact-photogeneration efficiency in a-Se ?

c) Electron-hole pair creation energy

A high-energy photon (e.g. X-rays or γ-rays) can create thousands of EHPs, but only a certain fraction of them are free to drift and the rest recombine. The electron-hole pair creation energy is defined as the average energy needed to create a single free EHP by a high-energy photon. In theory, two types of recombination are possible: general and initial recombination. The general recombination is defined as the recombination between any electron and hole generated within a volume (a-Se layer) from different ionizing tracks. This type of recombination is ignored for practical purposes since the dose rate needed to achieve almost 1% of recombination in a-Se is much larger than dose rates used for medical applications [34]. Furthermore, the initial recombination denotes to the recombination between electrons and holes created along a single track of ionizing radiation. Since general recombination is negligible in a-Se, the initial carrier recombination will be only assumed in the remainder of this thesis and is denoted simply by "recombination".

The mechanism of carrier recombination following X-ray excitation, electric field and temperature dependences of the electron-hole pair creation energy (amount of energy needed to produce a detectable EHP upon the absorption of an X-ray photon) remains unclear.

There are two fundamentally different types of recombination for charge carriers: geminate (electrons can only recombine with the other half of their original pair) and columnar recombination (any electrons and holes generated close to each other in the columnar track can recombine together). In both cases, the number of carriers escaping recombination should increase with increasing F that acts to separate the oppositely charged carriers. However, the X-

ray photogeneration efficiency increases significantly with increasing the X-ray photon energy [34] and the geminate recombination model fails to describe this phenomenon [35]. This appears to be due to a reduction of recombination with increasing X-ray energy. The rate of deposition of energy per unit distance travelled by a primary electron decreases as a function of energy, decreasing the density of EHPs in the column around it [36]. This is expected to reduce columnar recombination – as is seen. Thus, it appears that at low energies the contribution from columnar recombination is much higher than that from geminate and thus the columnar recombination theory is more appropriate for the diagnostic X-ray energies (12 to 120 keV). However, the exact nature of this recombination mechanism has yet to be determined. Hence, the mechanisms of X-ray generated free EHP creation energy in a-Se will be studied in this thesis.

1.7 Research Objectives

The success of utilizing avalanche multiplication gain of a-Se in X-ray detectors depends on the clear understanding of charge carrier generation and carrier transport mechanisms at extremely high fields. The charge carrier transport and photogeneration properties are extremely important for optimum design of the detector. Therefore, the main objective of this thesis work is to investigate the charge carrier transport and photogeneration mechanisms at extremely high fields in a-Se. The research objectives are categorized as follows:

a) Investigation of possible physical mechanisms and modeling of temperature and field-dependent effective drift mobility and impact ionization at extremely high fields in amorphous selenium.

b) Investigation of possible physical mechanisms and modeling of the electric field and excitation wavelength dependent photogeneration yield in amorphous selenium under high electric fields.

c) Investigation of possible physical mechanisms of X-ray generated free electron-hole pair creation energy in a-Se at high electric field for a wide variation of X-ray photon energy, electric field and temperature.

The following subsection will describe the detailed tasks and methodology of the research objectives for this work.

1.7.1 Detailed tasks and methodology

a) An analytical model for the microscopic mobility, momentum relaxation mean free path, and hence the effective drift mobility and impact ionization coefficient of carriers will be developed in this thesis by considering the density of states distribution, field enhancement release rate from the shallow traps, and carrier heating. The models for the effective drift mobility of holes will be evaluated considering both the Frenkel-Poole and thermally-assisted tunneling release mechanisms from shallow trap levels combined with the microscopic mobility model. The lucky-drift model for a-Se will be developed based on the observed field-dependent microscopic mobility. These developed models will be verified versus published experimental observations.

b) A formulation will be proposed for calculating the excitation wavelength and electric field dependent initial separation of the photogenerated and thermalized geminate electron and hole and applied to explain the field dependent photogeneration efficiency in a-Se. While the Onsager model for the free carrier photogeneration efficiency assumes that the recombination between an electron and a hole occurs when their separation is zero, the Onsager model will be appropriately extended for a-Se by considering recombination at a non-zero separation with a finite velocity. The theoretical model will be verified with respect to published experimental results.

c) An analytical model will be developed to show the electric field, X-ray energy and temperature dependence of the charge extraction yield limited by the columnar recombination for a-Se having widely unequal drift mobility for electrons and holes. The work has been divided into two parts: the first part is based on the calculation of the free electron hole pair creation energy by analytically solving the carrier continuity equations of two charged species considering only hole drift and bimolecular recombination between non-geminate electrons and holes. The model will be compared with previous columnar recombination models with widely varying field and temperature. In addition, the free EHP creation energy will be calculated by incorporating the initial charge extraction yield and the charge collection efficacy of the free carriers. Also, the results of this model will be compared with the recently published experimental results on EHP creation energy. The second part is based on numerically solving the three dimensional

continuity equations of both electrons and holes for calculating the charge extraction yield limited by the columnar recombination, considering carrier drift, diffusion and bimolecular recombination between non-geminate electrons and holes. The aim of this work is to verify the accuracy of the analytical model without neglecting the electron transport and diffusion. The numerical results will be compared with the published experimental results and with the analytical model. Also, the numerical model will be applied to the published experimental results on electron-hole pair creation energy with wide variations of X-ray energy, electric field and temperature. A comprehensive understanding on EHP creation energy in a-Se for X-ray and gamma ray excitations will be proposed.

1.8 Thesis Outline

This thesis is divided into six chapters. Following the introductory chapter, a discussion of the properties of a-Se that are of significant importance for understanding the results of this work is presented in Chapter 2. This chapter includes a description of the atomic and band structure of amorphous materials and the density of electronic states in the band gap of a-Se. The chapter concludes with the description of the charge transport, charge carrier photogeneration and electron hole pair creation energy mechanisms in a-Se. The model and results on charge carrier transport and impact ionization are presented in Chapter 3. The charge photogeneration at high electric fields in a-Se is presented in Chapter 4. Chapter 5 describes the X-ray generated free electron-hole pair creation energy model in a-Se at high electric fields. The conclusions drawn from the theoretical calculations are presented in Chapter 6, along with some recommendations for future works.

Chapter

2. Properties of Amorphous Selenium

2.1 Introduction

This chapter deals with the physical properties of amorphous selenium. Understanding the properties of a material can be achieved by looking at the arrangement of its constituent atoms and their different bonding possibilities. In this chapter, the atomic structure of amorphous solids, especially amorphous selenium, and their possible bonding arrangements, with attention to their effect on the electronic band structure, will be discussed. These are in turn used to determine the optical and electrical properties that are exhibited by the material. The chapter will begin with a brief description of amorphous solids before narrowing it down to the discussion of amorphous selenium.

2.2 The Atomic Structure of Amorphous Semiconductors

In general, a solid consists of a three dimensional network of atoms that are interconnected by atomic bonds. In a solid the atoms are close enough together that their electrons interact and their wave functions overlap. Covalent bonding can be understood by considering the atom's ground state wavefunction. In semiconductors, atomic bonds are formed when two or more atoms share their valence electrons to complete the sub-shells of each atom. And, the coordination number of a given atom is defined by the number of nearest neighbours for this atom in the solid.

The key features of atomic arrangement in a perfect crystal and an amorphous material are illustrated two-dimensionally in Figure 2-1. The solid spheres and lines in this figure represent the equilibrium position about which the atoms oscillate and the bonds between an atom and its nearest neighbours, respectively. The crystalline structure is characterized by a highly ordered arrangement of atoms as depicted in Figure 2-1 (a). A crystalline structure exhibits the same coordination number, bond lengths and bond angles for all atoms. Therefore, the equilibrium position of each atom in the network is known from any other position in the network. This type

of order is known as a long-range order since the periodicity of the network extends throughout the solid.

(a)

(b)
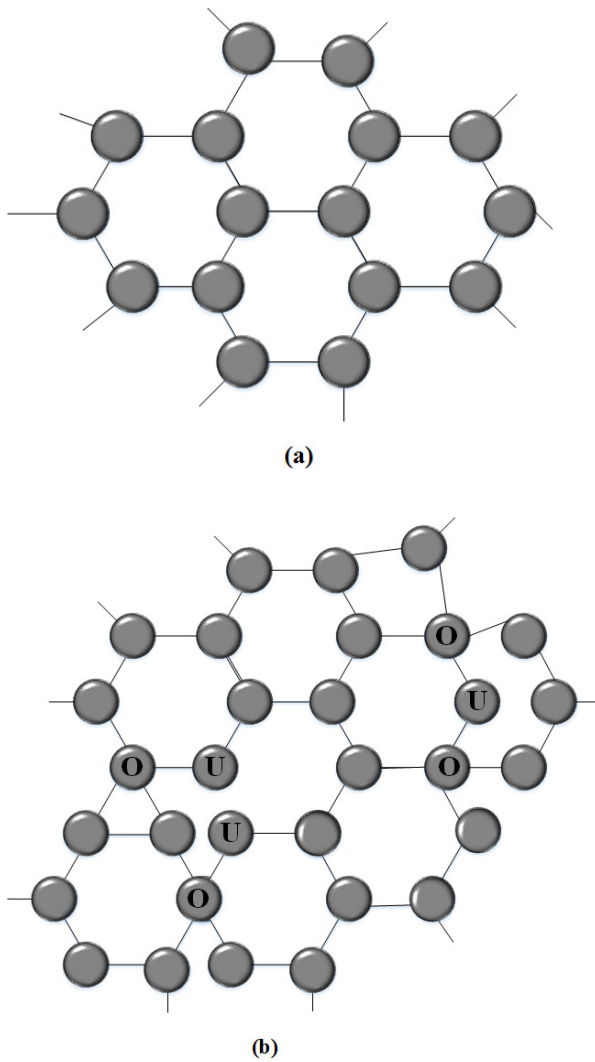
Figure 2-1 A two-dimensional representation of atomic structure for (a) a crystalline semiconductor and (b) an amorphous semiconductor. Over coordinated (O) and under coordinated (U) defects are shown for the amorphous case [37].

In an amorphous semiconductor, atoms have slight variations in their bond lengths and bond angles. These slight variations serve to destroy the spatial periodicity of the structure for distances greater than a few atomic radii, as depicted in Figure 2-1 (b). The amorphous structure therefore exhibits short-range order rather than long-range order characteristic of crystalline states. This type of disorder is known as topological disorder where it introduces localized electronic states, states where the electron wavefunction is localized to a particular position in

the semiconductor. The electronic and optical properties of an amorphous semiconductor are determined by the energy level and density of these localized states.

The atomic structures of crystalline and amorphous semiconductors contain defects that can also affect their electronic and optical properties. In a crystalline network, an atom is considered as a defect if it is not in its equilibrium position. In the amorphous structure, the coordination number of an atom is the only specific structural feature of this atom. It is often referred to as the normal structure bonding (NSB) of the atom. One cannot specify whether a specific structure is a defect or not since there is no correct position of an atom [37]. Therefore, the elementary defect of an amorphous semiconductor is a coordination defect where an atom has too many or too few bonds. The under-coordinated (U) (atoms with less than the usual number of bonds with adjacent atoms) and over coordinated (O) (atoms with more than usual numbers of bonds with adjacent atoms) defects shown in Figure 2-1 (b) introduce additional localized electronic states in the electronic structure of the amorphous material.

2.3 The Band Structure of Amorphous Semiconductors

In solid-state physics, the band model is considered as an important concept that can be used to explain the electronic and optical properties of semiconductors. It is derived from a quantum mechanical treatment of the behaviour of electrons, where a large number of atoms, which interact with each other resulting in a large number of electronic states within a small band of energy, form a solid. In a single atom system, the energy of the electron is quantized into discrete energy levels or states. The interaction of bonding orbitals leads to the formation of an energy band known as the valence band (VB) by the virtue of the valence electrons it contains. Another band that is entirely vacant is known as the conduction band (CB), which is due to the interaction between the anti-bonding orbitals [11]. In semiconductors, the valence and conduction bands are separated from each other by a fixed *energy gap* or *bandgap E_g*. The distributions of band states are described by functions known as density of states $g(E)$, which define the number of energy states per unit volume per unit energy. The density of states for crystalline semiconductors is shown in Figure 2-2 (a).

A quantitative development of the band theory of electronic structure of amorphous materials is much more complex due to the absence of any long-range topological order. Many researchers have believed that the amorphous band diagram is vastly different from the crystalline band diagram due to the disordered structure of amorphous semiconductors. However, as researchers discovered that amorphous solids compared to crystalline counterparts had similar electronic and optical properties, they concluded that only short-range order in the atomic structure is necessary for the band theory to be applicable [38].
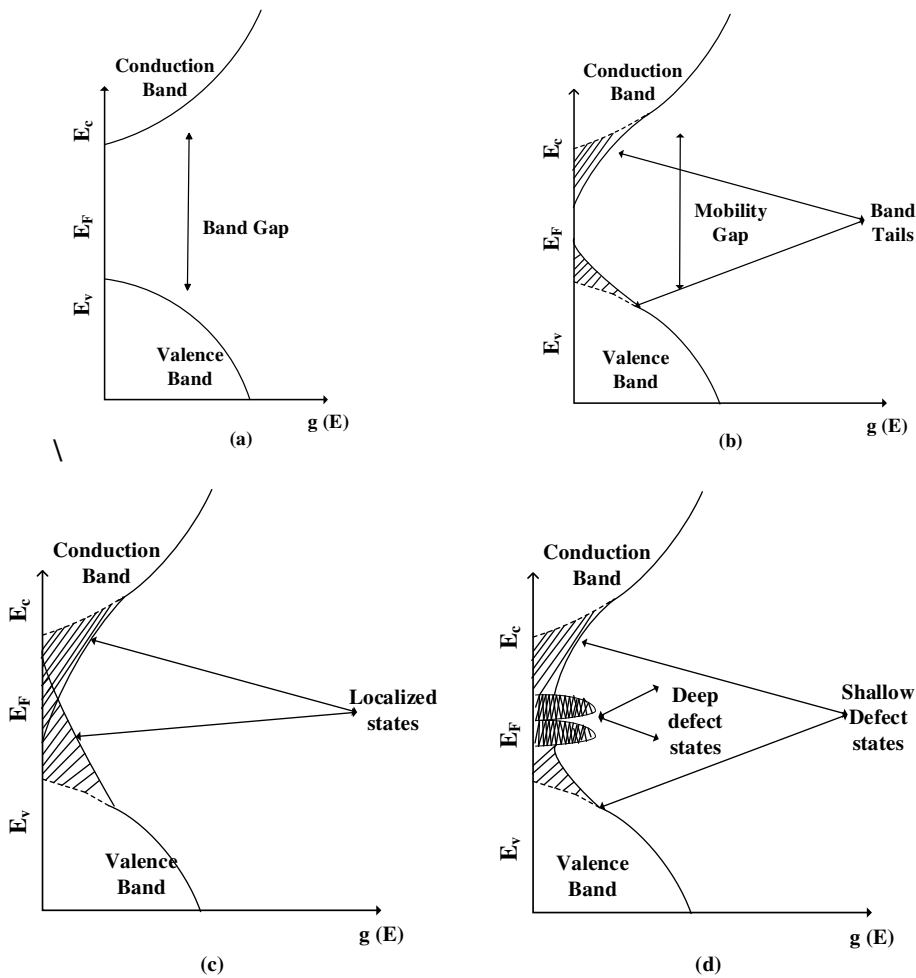
Figure 2-2 Density of States (DOS) models for crystalline and amorphous semiconductors. (a) In the crystalline case, two extended state bands are separated by a forbidden energy region defined by the band gap [38]. (b) The initial DOS model for amorphous semiconductors as proposed by Mott; the disorder of the amorphous network introduces localized states that encroach into the gap region [39]. (c) The CFO model for amorphous semiconductors showing localized states that extend continuously through the gap region [41]. (d) Marshall and Owen argued that defects in the structure would contribute a significant number of localized states deep in the gap region [42].

N.F Mott in 1960's [39] was the first to generalize the band theory of crystalline semiconductors to amorphous materials. He assumed that despite the differences in their atomic arrangement, crystalline and amorphous semiconductors would have similarities in their band structure. He noted that the electronic structure of crystalline semiconductors has the following universal features:

1. The individual electrons within the crystal are described by extended Bloch wave functions possessing long-range order in both amplitude and phase.
2. A gap of forbidden energies, which is well defined, separates the allowable bands of electron energies.

Mott postulated that in amorphous semiconductors, Bloch wavefunctions for electrons have long-range order in their amplitude, but only short-range order in their phases. Therefore, the sharp band edges due to long-range periodicity are replaced by tails of localized states, as shown in Figure 2-2 (b). Mott's hypothesis was based on the work of P. W. Anderson [40], who in 1958, showed that the translational and compositional disorder in amorphous materials resulted in localized states. These Anderson states that lie in the forbidden energy gap have an adverse effect on the carrier drift mobility. Electrons in the extended states have finite band transport mobility determined by the electron's effective mass in the solid. On the other hand, electrons in localized states move with a mobility that is controlled by thermally activated tunnelling between states. The mobility in the localized states disappears as the temperature approaches absolute zero. This transition in the mobility leads to the concept of a mobility gap for amorphous semiconductors, similar to the band gap of crystalline semiconductors.

M. H. Cohen, H. Fritzsche and S. Ovshinsky [41] extended Mott's model based on the assumption that Mott underestimated the degree of disorder. Their band model, known as the CFO model shown in Figure 2-2 (c) is characterized by the formation of localized tail states that extend throughout the mobility gap of the semiconductor and overlap in the region of the Fermi level. However, attempts to apply the CFO model to amorphous semiconductors failed since several amorphous semiconductors posses a significant degree of short-range order.

The structure of solids, amorphous or crystalline contains atoms that are coordinated differently from their normal structure bonding. Since the local connectivity of the network is well defined on a local basis, this may lead to well-defined localized defects such as dangling bonds, chain ends, vacancies, substitutional impurities and interstitials. Such defects are known as deviant electron configurations (DECs) and may lead to additional localized states within the mobility gap of the material. The carrier transport properties in crystalline semiconductors are well-known to be controlled by these defects.

Marshall and Owen [42] performed studies on the charge transport properties of amorphous chalcogenide semiconductors. It was originally assumed that the intrinsic disorder of the amorphous structure introduced a sufficiently large density of states in the gap to obscure any effects from the defect states. However, the Marshall and Owen experiments indicated the presence of localized states in the mobility gap at various well-defined energies in addition to the tail states as shown in Figure 2-2 (d). In their band model, the bands of donor- and acceptor-like states that appear in the upper and lower half of the mobility gap respectively determine the Fermi level. As the solid forms, due to a self-compensation mechanism, these states adjust themselves and the Fermi level remains near the center of the gap. It should be noted that the band model of a semiconductor can be easily affected by even a small concentrations of these states, and hence, their origin is considered with particular interest for specifying the electronic properties of the material.

2.3.1 The Electronic Density of States Model in the Band Gap of a-Se

The electronic properties of amorphous materials largely depends on the nature of the density of states (DOS) distribution within the mobility gap. Although a-Se has been extensively studied, the exact shape of the DOS distribution for a-Se is still surrounded by various uncertainties and controversies. A number of DOS models have been proposed and discussed in the literature [11, 43-48]. A general consensus on the DOS distribution near the mobility edges is that is it not a single exponentially decaying function but that it exhibits certain peaks whose exact positions are still controversial.

One of the most often cited models describing the DOS in the gap of a-Se that has been derived from various experiments, such as time-of-flight (TOF) transient photoconductivity, xerographic cycled-up residual voltage decay, and xerographic dark discharge has been proposed by Abkowitz [43] in 1988. The later model is an extension of the Owen-Marshall DOS model [42] describing the DOS in the gap of the amorphous As_2Se_3. Figure 2-3 illustrates the main features in the DOS proposed by Abkowitz that are a decaying density of localized states from the band edges, with peaks close to the valence and conduction band edges. These peaks are known as shallow hole and electron traps, respectively, and they control the mobilities of holes and electrons in selenium through the process of multiple trapping and de-trapping in these states. Near the Fermi level, there are two additional peaks in the DOS, which are known as deep traps. The deep states are of particular interest for X-ray imaging applications. The concentration of these traps determines the lifetime of charge carriers in amorphous selenium, since the thermal release time from them is much longer than the time scale of the associated experiment. For the DOS shown here, the mobility gap E_c-E_v for amorphous selenium is effectively 2.22 eV as indicated in the diagram.
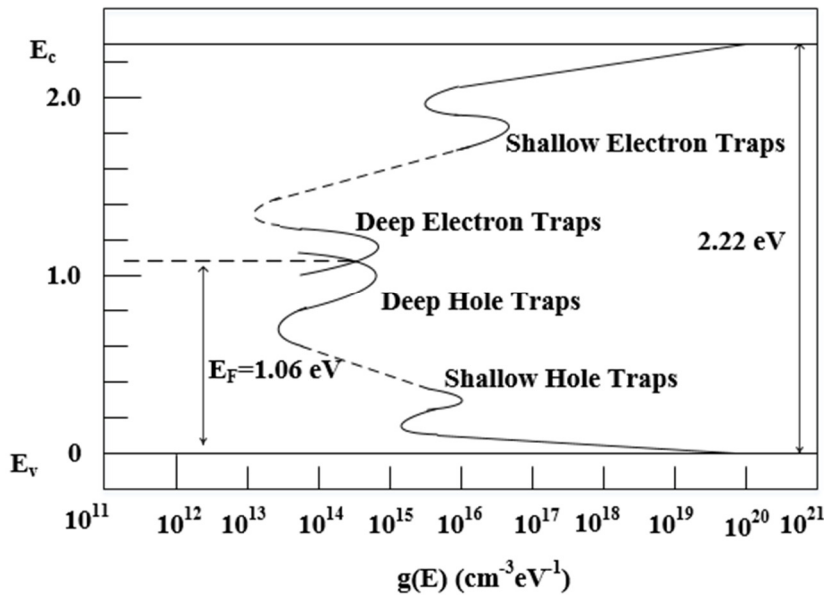
Figure 2-3 The density of states function for amorphous selenium as determined from experimental measurements such as time of flight (TOF) transient photoconductivity, xerographic cycled-up residual voltage decay, and xerographic dark discharge [43].

26

2.4 The Atomic Structure of Amorphous Selenium

Selenium is a member of a family of elements known as the chalcogens, located in the group VI of the periodic table. All elements of the chalcogen family can accommodate up to eight electrons in their outermost shell. The outermost shell consists of two subshells, named *s*-type and *p*-type subshells. The *s*-type states can hold two electrons, while *p*-type can hold up to six allowed states. Selenium, with an atomic number of thirty-four (Z = 34), has twenty eight inner core electrons and six valence electrons in the outer most shell. The two *s*-electrons form a lone pair (LP) and do not participate in bonding. The remaining four electrons reside in the *p*-subshell. Two of the four *p*-state electrons normally form a lone pair and are sometimes referred to as non-bonding (NB) states. The remaining two electrons are available for covalent bonding to other atoms. Therefore, Se atoms in a solid have a two-fold coordinated bonding configuration with an optimum bond angle of 105° [49] representing the lowest energy configuration for selenium.

Selenium exists in both crystalline and amorphous forms. In the crystalline state, selenium has two forms of the crystalline phase of the solid, which are known as *α*-monoclinic Se (*α-Se*) and trigonal (*γ-Se*). The *α*-monoclinic Se is composed of eight member (Se$_8$) rings while the trigonal structure *γ*-Se consists of parallel, spiral Se$_n$ molecule chains (selenium chain). In the amorphous phase of selenium, it was assumed that the amorphous form of Se would consist of a mixture of these ring-like and chain-like formations randomly distributed throughout the solid. However, structural investigation of a-Se and its alloys favours a "random chain model" with all the atoms in a two-fold coordinated chain structure.

The phonon spectra of crystalline trigonal (*γ-Se*) and amorphous selenium phases are very similar [50], with the high-energy peak at 29 and 31 meV for *γ-Se* and a-Se, respectively. The part of the mobility that is controlled by the electron–phonon interactions is the same for amorphous and crystalline state of the material [51]. Trigonal Se is an example of reststrahlen-displaying elemental crystal [52]. The unit cell of *γ-Se* consists of three atoms and it shows a net unit-cell electric moment. Its phonon scattering behaviour is qualitatively similar to the ionic crystals and thus polar-mode scattering has a very significant influence on the carrier transport.

The structure of amorphous solids is not completely random where a degree of order at least between the individual atoms is present. Each individual atom in the solid tends to fulfill its valency requirements. However, due to the lack of periodicity in the amorphous strutcture, not all atoms can meet their requirements. Another important characteristic of amorphous selenium is the presence of some thermodynamically derived charged structrural defects, known as valence alternation pairs (VAP). These defects correspond to some of the chalcogen atoms being under and over-coordinated [53-55]. The most studied defects in a-Se are the over-coordinated atoms of the type Se_3^+ (D^+) and the under-coordinated atoms of the type Se_1^- (D^-) valence-alternation pairs (VAP) [53]. If the atoms of the pair (Se_3^+ and Se_1^-) are in close proximity, they are termed an intimate valence alternation pair (IVAP) and these defects can act like neutral defects. These VAPs or IVAPs are thermodynamically derived structural defects (the defect concentrations are in thermal equilibrium with the ambient) and are considered to be the cause for the creation of localized defect states in the energy gap of a-Se photoconductor films.

2.5 Amorphous Selenium as a Photoconductor

Photoconductors are the materials that show quite low electrical conductivity at dark condition and a significant improvement of conductivity under light illumination. Upon light illumination, free carriers are generated and transported through the photoconductor by the application of an electric field to form a measurable electrical signal. The generation of free carriers in amorphous selenium can be achieved under irradiation with several radiations such as light, X-rays, gamma rays, α- and β- particles. Under the influence of an applied electric field, both electrons and holes can travel in a-Se. Figure 2-4 shows a practical X-ray detector structure which is an electrode/blocking layer /photoconductor/blocking layer/metal type. The X-ray/light absorption, ionization (electron hole pair generation) and charge transport occur in the bulk a-Se photoconductor layer, where both holes and electrons can drift. The blocking layers must block carrier injections from the electrodes and allow photogenerated carrier to flow from the photoconductor layer to the electrodes in order to eliminate carrier accumulation.

The aim of the following subsections is to provide some theoretical background to the photoconductive properties of a-Se.
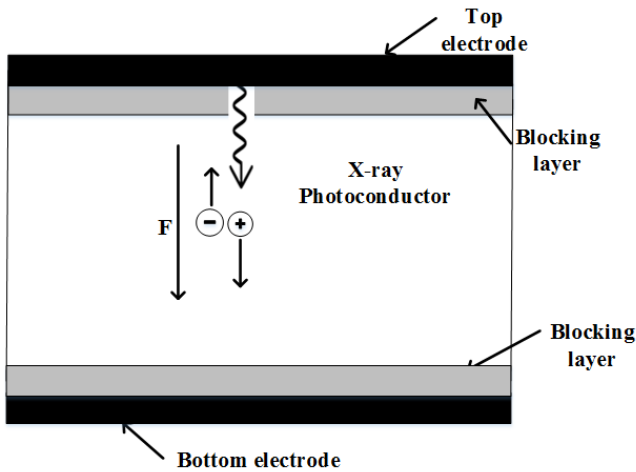
Figure 2-4 The structure of an a-Se X-ray detector.

2.5.1 Random potential fluctuations

Carrier transport in crystalline semiconductors involves motion in extended states, except for the cases with extremely high doping levels or at very low temperatures. Electrons and holes can travel in the conduction and valence bands, respectively. Under the influence of an electric field, free electrons and holes travel in the extended states. However, in the absence of some external source of excitation, such as X-rays or light, random thermal vibrations of the crystalline lattice create electrons and holes. If these vibrations acquire sufficient energy, they can excite electrons from the valence band into the conduction band. Alternatively, photons with energy $hv > E_g$ can also excite the electrons across the bandgap.

Localized states in the mobility gap of amorphous materials have a great effect on the carrier transport process and therefore on the electronic properties of these materials. Considering the form of the band structure shown in Figure 2-2 (c), a number of carrier transport processes are probable. Only the variation of electron mobility in amorphous solids at room temperature is discussed in this section, but the arguments are equally valid for holes after proper modification in terminology and carrier parameters. Considering the states above E_c, which in the corresponding crystalline material lie well within the conduction band. The effect of random

potentials and varying interatomic distances is comparatively low for these states. The mean free path is much longer than the average interatomic distances and carrier transport is interrupted due to random scattering. The predicted minimum value of mobility for electrons in these states is 100 cm^2 V^{-1} s^{-1} [56]. For mobilities less than 100 cm^2 V^{-1} s^{-1}, the mean free path between two scattering events becomes less than the de Broglie wavelength of the electron. Whereas, for mobilites less than 10 cm^2 V^{-1} s^{-1} the mean free path is less than the interatomic spacing. In the extended states just above the mobility gap of the material, effects of the disorder highly dominate the charge transport process that it can no longer be considered as a band motion with random scattering. The motion in these states is considered a diffusive motion, having a mobility of the order of 1 cm^2 V^{-1} s^{-1}[57].

In amorphous semiconductors, a high density of defect states results in localization at energies below E_c. Conduction in these localized states can still occur through direct tunnelling between localized states as if the carriers "hop' from one localized state to another. The drift mobility is in the range of ~10^{-2} cm^2 V^{-1} s^{-1}, or less at room temperature. This sharp decrease in mobilities near E_c and E_v defines the mobility edge of the non-crystalline solids [58].

2.5.2 Charge Carrier Transport in Amorphous Selenium

As mentioned earlier in this chapter, the exact shape of the DOS distribution for a-Se is still surrounded by various uncertainties and controversies. Thus, the exact treatment of the charge transport in a-Se remains a very difficult task. However, for most cases, the electron and hole transport in a-Se can be treated in terms of two effective trapping levels for each type of carrier. In other words, the first of those two trapping levels is close to the band edge and represents a set of shallow traps that controls the effective mobility of the carriers. The other level represents a set of deep traps that controls the effective carrier lifetime, and thus, the average distance that a carrier can travel at a given electric field before being deeply trapped.

The experimental observations of the carrier drift mobility in a-Se indicate that both electrons and holes are mobile and thermally activated at low temperatures [27, 42]. Drift of both electrons and holes involves interactions with shallow and deep traps, as shown in Figure 2-5

Furthermore, it is believed that the carrier drift mobility is shallow trap controlled [59]. This means that the effective drift mobility μ of the carriers is the microscopic mobility μ_0 in the extended states reduced by trapping and release events involving the shallow traps, i.e.,

$$\mu = \theta_r \mu_0 = \frac{p_{free}}{p_{free} + p_{trapped}} \mu_0 \tag{2.1}$$

In Equation 2.1, θ_r is the mobility reduction factor [60], p_{free} is the concentration of carriers in the transport band, and $p_{trapped}$ is the concentration of carriers occupying shallow traps. The mobility reduction factor depends on the shallow trap energy depth, on their concentration, on the temperature and applied electric field. The values for the microscopic mobility for holes and electrons are known to be ~ 0.9 cm^2 V^{-1} s^{-1} [25] and ~ 0.5 cm^2 V^{-1} s^{-1} [26], respectively. At room temperature, the most commonly observed effective mobility of holes is in the range of 0.12 to 0.14 cm^2 V^{-1} s^{-1} for the applied field of less than 20 V/ μm. As for electrons, the observed effective mobility ranges from 0.003 to 0.006 cm^2 V^{-1} s^{-1} [27]. The values of the mobility reduction factor under such conditions can be calculated to be ~ 0.4 - 0.5 for holes and about one order of magnitude smaller for electrons.
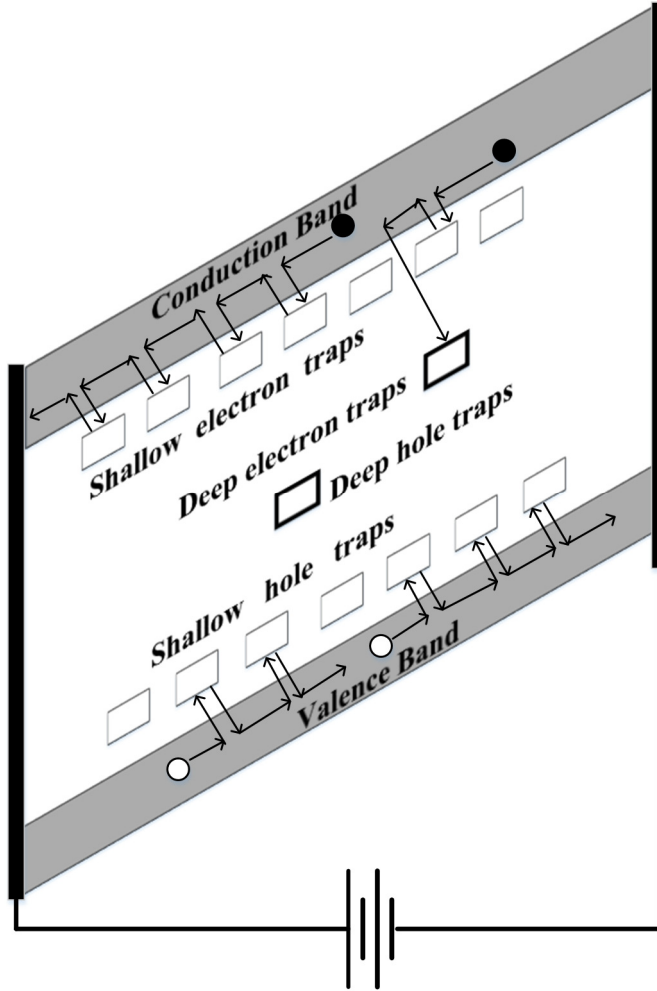
Figure 2-**5** Diagram illustrating the band gap of a photoconductor with an applied electric field, which tilts the bands encouraging drift of holes in the direction of the field and electrons counter to the field. Drift of both electrons and holes involves interactions with shallow and deep traps. Shallow traps reduce the drift mobility and deep traps prevent the carriers from crossing the photoconductor.

For a discrete set of monoenergetic shallow hole traps, the equation that describes the effective hole mobility at different temperatures is

$$\mu = \mu_0 [1 + \frac{N_t}{g_v} \exp(\frac{E_t}{k_B T})]^{-1} \approx \mu_0 \frac{g_v}{N_t} \exp(-\frac{E_t}{k_B T}) \tag{2.2}$$

where N_t is the shallow trap concentration, g_v is the density of states at the VB mobility edge E_v, and E_t is the energy depth of the shallow traps from E_v. At sufficiently low temperatures where $p_{trapped} \gg p_{free}$, the effective mobility $\mu \approx (p_{free}/p_{trapped}) \mu_0$ and equation (2.2) has a clear Arhenius form. As the temperature is increased, μ approaches μ_0. If equation (2.2) is fitted to the

experimental mobility versus temperature data [27], one can determine the location of the shallow traps in Figure 2-3. It has been shown that the peak concentration of shallow hole traps occurs at $E_t - E_v \approx 0.28$ eV, while the peak in the shallow electron trap occurs at $E_c - E_t \approx 0.35$ eV [48].

It has been shown that the shallow and deep localized states in the mobility gap are due to various defects in the structure of a-Se that are thermodynamically stable at room temperature [61, 62]. The deep states are of particular interest as they control the carrier lifetimes, or trapping times, and hence determine the carrier schubweg $\mu\tau F$ and thus the photoconductor performance. Experiments at Xerox in the 1980s showed that these states are derived from equilibrium defects [61] and, hence, cannot be eliminated through careful preparation methods or by the purification of the source material.

The effects of impurities and alloying elements on the transport properties of a-Se have been extensively studied in the literature. Pure amorphous selenium is unstable and crystallizes over time, which varies from months to years depending on the ambient conditions and the origin of the a-Se [11]. Small amounts of As (0.2 %-0.5 %) are alloyed with a-Se in order to control the crystallization process. The viscosity of amorphous structure is increased since trivalent As atoms are triply bonded and link with Se chains, and hence, crystallization is prevented. However, the addition of As affects also the electronic transport in a-Se: the hole lifetime decreases while electron lifetime increases. Adding a halogen (e.g. Cl) in parts per million (ppm) range may overcome this problem, which will improve the hole lifetime and deteriorates the electron lifetime slightly [63].

A thermally stable film with balanced hole and electron transport can be achieved by adjusting the amount of As and Cl in the material. The resulting material is known as stabilized a-Se, and the nominal compensation is indicated, for example, as a-Se: 0.3% As +20 ppm Cl. Table 2-1 summarizes the transport properties of a typical stabilized a-Se photoconductor film.

Table 2-1 The transport properties of stabilized a-Se (0.2-0.5% As + 10-40ppm Cl) photoconductor films [27, 62].

Property	Typical Range	$\mu\tau F$ @ 5 V/ μm	Comment
Hole mobility μ_h (cm²/ Vs)	0.12 – 0.14		Well reproducible, probably shallow trap controlled
Electron mobility μ_e (cm²/ Vs)	0.003 – 0.006		Decreases rapidly with As addition, probably shallow trap controlled
Hole lifetime τ_h (μs)	20 - 200	1.2 – 12 mm	Depends on the substrate temperature
Electron lifetime τ_e (μs)	200 - 1000	0.13 – 1.5 mm	Sensitive to small quantities of impurities
Hole range $\mu_h\tau_h$ (cm²/ V)	2 x 10⁻⁶ to 2 x 10⁻⁵		Substantially higher than PbI₂
Electron range $\mu_e\tau_e$ (cm²/ V)	1 x 10⁻⁶ to 6 x 10⁻⁶		Somewhat higher than PbI₂

2.5.3 Optical Photogeneration in Amorphous Selenium

The conductivity of semiconductor materials (e.g. a-Se) increases with exposure to light due to an increase in the charge carrier density in the material. This phenomenon is recognized as photoconductivity where an incident optical photon with sufficient energy can (with certain probability) excite an electron from the VB into the CB. The probability that photon will be absorbed within the photoconductor layer is determined by the optical absorption coefficient of the material. This value depends on the incident photon energy and the magnitude of the DOS at the band edges. The absorption probability is extremely small if the energy of the incident

photon is less than the band gap of a-Se. As the energy of the incident photons exceeds the band gap energy, the magnitude of the absorption coefficient abruptly rises.

The generation of an electron-hole pair is due to the absorption of an optical photon where an electron excited to the CB leaves a hole in the VB. These optically generated charge carriers may contribute to the conduction current in the presence of an electric field only if the electron and hole are separated by the applied electric field before having a chance to recombine. The quantum efficiency η determines the probability that a generated EHP is separated due to the application of the electric field. The electron-hole pairs that are not separated by the field quickly recombine in a-Se and do not contribute to the conduction current.

The photogeneration efficiency (known as the fraction of the free EHPs to all the EHPs created) in a-Se is much less than unity and depends on the electric field and photon wavelength [31]. The simultaneously photogenerated electron and its hole twin (known as a geminate pair) are attracted to each other by their mutual Coulombic force and may eventually recombine (this recombination is known as geminate recombination). The excess kinetic energy carried by the photogenerated electron or hole is dissipated by phonons and thus, they are thermalized. After this thermalization process, the geminate electron and hole are separated by a distance r_0 at an angle θ with the applied field F. Then the geminate pair dissociates to free charge carriers with probability φ. The fraction of the absorbed photons that results in bound thermalized pairs is usually referred to as the production efficiency (η_0). The dissociation efficiency (φ) depends on the initial distance between the two carriers. The larger the initial distance, the greater the dissociation efficiency would be for any given electric field.

Furthermore, the mechanism behind the field dependent photogeneration efficiency observed in a-Se has been explained so far by the Onsager theory for the dissociation of photogenerated EHPs [31]. The Onsager theory calculates the probability that an EHP will dissociate, as a result of diffusion, under the action of an a electric field F. The photogeneration efficiency ($\eta = \eta_0 \, \varphi$) can be expressed as a product of two quantities. The first one is the efficiency (η_0) of the intrinsic photogeneration process that depends strongly on the energy of the incident photons and the second one is the probability (φ) that the generated EHP is separated

which depends on the applied field, temperature and on the initial separation between the electron and the hole in the pair.

2.5.4 X-ray Photogeneration in Amorphous Selenium

A good candidate photoconductor for X-ray imaging must have an excellent X-ray photoconductivity. The creation of electron-hole pairs (EHPs) by an incident energetic particle or an X-ray photon first involves the generation of an energetic primary electron. As this energetic photoelectron travels in the solid, it causes ionizations along its track and creates many EHPs. In this way, one X-ray photon can create hundreds or thousands of EHPs.

The number of EHPs, N that is generated by the absorption of an of X-ray photon of energy E is defined by

$$N = \frac{E}{W_{ehp}}$$

(2.3)

where W_{ehp} is the average EHP creation energy, the amount of radiation energy required to create a single free EHP. This value must be kept as low as possible in order to maximize the sensitivity of the detector. It should be noted that, not all the created electrons and holes are collected. Carriers can be lost through trapping or through a recombination process. This means that the measured electron-hole pair creation energy is an effective energy for creating free EHPs, W_{ehp}.

For many semiconductors, the energy W_{ehp} required to create an EHP has been shown to depend on the energy bandgap E_g via *Klein's rule* by $2.8E_g + E_{phonon}$ [64]. The phonon energy term E_{phonon} is expected to be small (~0.1 eV) so that typically W_{ehp} is close to $2.8E_g$. Further in many crystalline semiconductors, W_{ehp} is field independent and well defined. This W_{ehp} is so well defined in crystalline semiconductors, such as high purity Silicon (Si) and Germanium (Ge) crystals, that they are used in spectometers to measure the energy of X-rays [65]. W_{ehp} can be easily calculated for various crystalline solids, but there are also a number of solids such as hydrogenated amorphous silicon (a-Si:H), mercuric iodide (HgI_2) and lead iodide (PbI_2) that have W_{ehp} values less than that predicted by Klein's rule.

For amorphous semiconductors, as suggested by Que and Rowlands [66], the relaxation

of conservation of momentum rule leads to $W_{ehp} = 2.2E_g + E_{phonon}$. For a-Se, which has a band gap of about 2.2 eV, Klein's formula predicts a W_{ehp} of about 7 eV. However, experiments have found that the average energy required to create a free electron and a free hole in a-Se is not only much larger than 7 eV, but also depends on the applied electric field. For example, at F=10 V/μm, each measured electron-hole pair corresponds to about 50 eV deposited X-ray energy which clearly disagree with Klein's formula. Therefore, the free electron and hole pair creation energy W_{ehp} does not follow the Klein nor the Que-Rowlands rules at practical electric fields. The W_{ehp} exhibits a very pronounced field dependence that tends towards an intrinsic value W_0 at very high electric field. In other terms, W_{ehp} in a-Se, as in a number of other low mobility solids, has a strong dependence on electric field F and a relatively weak dependence on the X-ray photon energy E and temperature T [67, 68].The incident X-ray photon first creates an energetic primary electron and it generates many EHPs along its path but only a certain fraction of these are free to drift and the rest recombine before they have the chance to separate into a free electron and a free hole, and hence are not measured by experiments.

There are various explanations for the field dependence of the EHP creation energy. The primary electron generates many EHPs but only a certain fraction of these are collected because some disappear through recombinations and some become trapped as they drift across the photoconductor. Practically, if no carriers are lost due to trapping, which will be the case for device-quality photoconductor material, then the recombination losses may be attributed to three sources. First, is simple bulk recombination or bimolecular recombination, between drifting electrons and holes. The recombination rate is proportional to both the hole and electron concentrations so that the collected charge Q does not increase linearly with the intensity of the radiation. Actually, it depends linearly on the square root of the intensity. However, experiments show that Q increases linearly with the intensity. Thus, this type of recombination is ruled out.

The second source is known as geminate recombination (Gemini-the twins). In this case, the simultaneously generated electron and its hole twin are attracted to each other by their mutual Coulombic force and may eventually recombine [66, 69]. The third source which is another possible mechanism is columnar recombination that involves the recombination of non-geminate electrons and holes generated close to each other in the columnar track of the single high energy

electron (primary) created by the absorption of an X-ray photons as shown in Figure 2-6. This columnar recombination assumes that ionization along the path of the primary ionizing particle is dense enough that the geminate recombination is negligible and the mean separation between electron-hole pairs is much less than the column diameter.
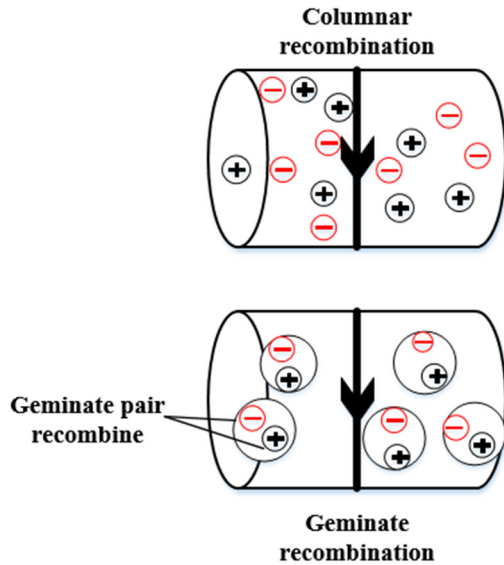
Figure 2-6 Figure illustrating the mechanisms that reduce the number of collected (free EHPs) and hence reduce the sensitivity. Columnar recombination (bimolecular recombination within primary electron tracks) and geminate recombination (recombination of an EHP created at the same time and bound by their mutual Coulomb attraction).

2.6 Summary

In this chapter, the structure and electronic properties of amorphous selenium were described. The atomic arrangement in amorphous semiconductors has a certain short-range order and is not completely random. The variations in the periodic lattice structure lead to replace the sharp band edges in the DOS diagrams by tail states extending into the mobility gap. VAP type defects introduce additional localized states into the band gap. The DOS models for amorphous selenium proposed by different researchers were briefly described.

At the end of this chapter, the charge transport, optical and X-ray photogeneration properties of amorphous selenium have been outlined.

Chapter

3. Mechanisms of temperature- and field-dependent effective drift mobilities and impact ionization coefficients in amorphous selenium

3.1 Introduction

As mentioned earlier in this thesis, although avalanche multiplication in a-Se has been experimentally confirmed, a clear understanding of carrier transport at extremely high fields and its effect on the impact ionization process remain unresolved. In this thesis, the mechanisms of electric field and temperature dependent effective drift mobility and impact ionization coefficient of both holes and electrons in amorphous selenium are investigated. An analytical model for the microscopic mobility, momentum relaxation mean free path, and hence the effective drift mobility and impact ionization coefficient of carriers is developed in this thesis by considering the density of states distribution, field enhancement release rate from the shallow traps and carrier heating. The results of the model are fitted with the published experimental results on the effective mobility and the impact ionization coefficient with wide variations of the applied electric field and temperature.

3.2 Analytical Models

3.2.1 Effective drift mobility

The charge carrier transport in amorphous semiconductors largely depends on the nature of density of states (DOS) within the mobility gap. A general consensus on the DOS distribution near the mobility edges is that is it is not a single exponentially decaying function but exhibits certain peaks whose exact positions are still controversial. Though there are controversies on the magnitude and position of the peak, the DOS function for the shallow traps near valence (or conduction) band can be approximated as the sum of the exponential tail and a Gaussian peak at E_m as [70]

$$N(E) = g_v \exp(-E/k_B T_0) + N_m \exp\left\{-(E-E_m)^2/\Delta E_m^2\right\}, \tag{3.1}$$

where T_0 is the characteristic temperature and N_m is the peak value of shallow traps at $E=E_m$ and g_v is the DOS at the valence band edge.

The carrier release phenomenon from a shallow trap is much faster, and the carrier trapping is balanced by the carrier release process. Therefore, neglecting the trap saturation effect, the kinetic equation for the trapped holes (p_t) at energy E from the valence band edge is:

$$\frac{dp_t(E)}{dt} = C_t N(E) p_h - v_0 p_t R(F) \exp(-E/k_B T) \tag{3.2}$$

where C_t is the capture coefficient of holes, $N(E)$ is the DOS of a-Se at energy E in the midgap, p_h is the free hole concentration, T is the absolute temperature, k_B is the Boltzmann constant, t is the time, and v_0 is the attempt to escape frequency. The relation between v_0 and C_t can be determined by the principle of detailed balance, which gives $v_0 = (g_v k_B T) C_t$, where $(g_v k_B T)$ is approximately the effective DOS at the valence band.

Furthermore, $R\ (F)$ is the field-dependent enhancement factor for the carrier release event that can be due to either a thermally activated tunneling (TAT) or a Poole-Frenkel (PF) effect. Starting with the PF effect, a classical mechanism in which the electron is thermally emitted over the top of a potential barrier, which has been lowered by the presence of an electric field as illustrated in Figure 3-1.
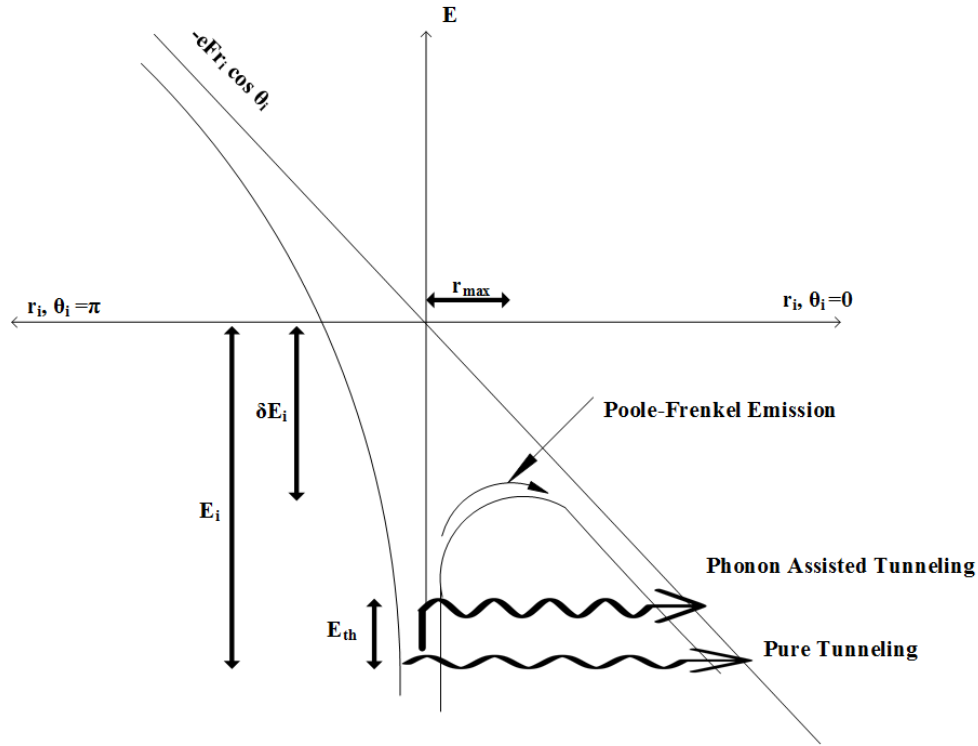
Figure 3-1 Figure illustrating mechanisms of field-enhanced emission: Poole-Frenkel emission, Phonon assisted tunneling, and Pure tunneling [70].

For the three-dimensional (3D) PF trap release, the field dependent enhancement factor is described by the following equation [71]

$$R_{PF}(F) = (1/\gamma^2)\left[(\gamma-1)\exp(\gamma)+1\right] + \frac{1}{2}$$

(3.3)

where $\gamma = \sqrt{eF/\pi\varepsilon_s}/k_BT$, $\varepsilon_s = \varepsilon_0\varepsilon_r$, ε_0 is the absolute permittivity, and ε_r is the relative permittivity of a-Se.

As for the TAT process, the potential barrier for a trapped carrier is essentially a triangular barrier, as shown in Figure 3-2 [69]. As the vibration energy $E`$ increases, the tunneling barrier decreases and hence the release probability increases. On the other hand, the population of the energy level $E`$ decreases with increasing $E`$ proportionally to $exp\ (-E`/k_BT)$, where T is the absolute temperature and k_B is the Boltzmann constant. Thus, there exists an

optimum vibrational energy E' for which the resultant escape probability is maximised, which is proportional to $\exp(\beta F^2/k_B T)$ [72]. The expression of β is determined by considering the tunneling probability through a triangular barrier together with the Boltzmann occupation probability in crystalline materials and given by $e\hbar^2/(24m^*k_B^2T^2)$, where $\hbar$ is the modified Plank constant and m^* is the effective mass of the carrier [72].

Conduction band edge
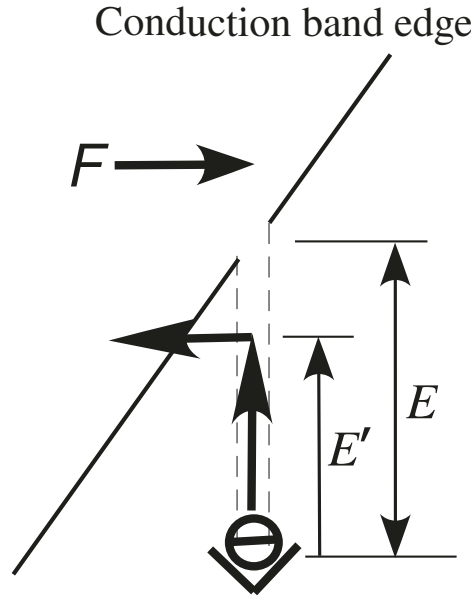
Figure 3-2 Schematic presentation of an electron release from localized states at high external electric field by the thermally assisted tunneling to the conduction band.

Thus, considering the wide variation of the vibrational energy E', the enhancement factor for the carrier release can be written as,

$$R_{TAT}(F) = \exp[(a_{eff}F + b_tF^2)/k_BT] \tag{3.4}$$

where a_{eff} is the effective tunneling distance in the direction of the electric field and $b_t = f\beta$, f is a fitting parameter for amorphous materials.

At steady state, Equation (3.2) gives

$$\frac{p_t}{p_h} = \frac{N(E)}{R(F)g_vk_BT}\exp(E/k_BT) \tag{3.5}$$

The shallow trap controlled effective hole mobility μ can be written using equation (2.1)

$$\mu_h(F,T)=\mu_{0h}(F,T)[\frac{p_h}{p_h+\int\limits_0^\infty p_t(E)dE}]=\mu_{0h}(F,T)[1+\int\limits_0^\infty \frac{N(E)}{R(F)g_v k_B T}\exp(\frac{E}{k_B T})dE]^{-1} \qquad (3.6)$$

where e is the elementary charge, μ_{0h} is the free carrier mobility (microscopic mobility), F is the electric field. The subscript "h" stands for holes. Considering $\mu_{0h}\sim 2$ cm^2/V s, F=100V/μm, and $\mu_{0h}F = 2 \times 10^6$ cm/s. The parameter $\mu_{0h}F$ is higher than the sound velocity v$_s$ (~2×10^5 cm/s in a-Se) [73] and much less than the average thermal velocity at room temperature (~10^7cm/s). At high field regime, as the field increases, the average energy of the carriers also increases and they acquire an effective temperature T_{eff} that is higher than the lattice temperature T. The effective temperature T_{eff} of holes can be described by the Shockley formula [74]

$$\frac{T_{eff}}{T} =\frac{1}{2}[1+\sqrt{1+(\frac{C\mu_{0h}(0)F}{v_s})^2}] , \qquad (3.7)$$

where $\mu_0(0)$ is the zero-field μ_0 , and $C=\sqrt{(3\pi/8)}$ in crystalline semiconductors and it can be a fitting parameter for amorphous or other materials (for simplicity, $C=\sqrt{(3\pi/8)}$ is assumed in this work). Thus, the microscopic mobility at the lattice temperature T [75]

$$\mu_{0h}(F,T)= \mu_{0h}(0)\left(\frac{T_{eff}}{T}\right)^{-1/2} , \qquad (3.8)$$

Substituting Equation (3.1) into Equation (3.6) and integrating gives,

$$\mu_h \approx \left[1+\left\{R(F)(\frac{T}{T_0}-1)\right\}^{-1}+\left\{\frac{\sqrt{\pi}\Delta E_m r_{tv}}{k_B T R(F)}\right\}\exp\left\{(\frac{\Delta E_m}{2k_B T})^2+E_m/k_B T\right\}\right]^{-1}\mu_{0h}(F,T) \qquad (3.9)$$

where $r_{tv} = N_m/g_v$. Note that the expression for the effective electron mobility will be similar to Equation (3.9) with appropriate parameters for electrons and density of states near the CB.

3.2.2 Impact Ionization phenomenon

In 1980 Juska and Arlauskas [26] reported the first clear experimental observations of impact ionization in an amorphous semiconductor (a-Se), which was confirmed by further experimental studies [76, 77]. Due to these studies, the phenomenon of impact ionization in amorphous solids has found an application in photosensors for high sensitivity TV camera tubes [76]. The combination of the unique photoconducting properties of a-Se with the impact ionization has a high potential in X- and γ-ray detectors for medical imaging applications [12, 78]. Even though the experimental evidence for avalanche multiplication in a-Se is clear cut, the theoretical understanding of the origin and nature of this phenomenon in amorphous semiconductors has remained unresolved. The mean free paths in these semiconductors are so short (compared to the typical mean-free path in crystalline materials) that impact ionization has been difficult to understand.

It has been possible to formulate an explanation for the avalanche multiplication mechanism in a-Se in terms of the modified lucky-drift (LD) model [79], which had been originally proposed for crystalline semiconductors by Ridley [80], Burt [81], Shockley [82], and Mckenzie and Burt [30]. Shockley introduced the ionization probability distribution in the context of lucky electrons. He proposed that if an electron obtains sufficient threshold energy E_i, it is able to generate an electron-hole pair via the impact ionization process. To do so, the carrier should gain the required energy in a ballistic motion. In such a motion the electron avoids any scattering event until it reaches the ionization threshold energy [79]. The mean free path describes the distance that such a carrier travels. The lucky electron model gives no explanation to the quantitative value of ionization threshold energy [79]. It is kept as a fitting parameter. Therefore, the weakness of Shockley's assumption is that either the charge carrier is lucky and travels in a ballistic motion a distance of l_0 ($=E_i/eF$) avoiding any scattering until its energy reaches E_i, or it suffers a sufficient number of collisions to keep its energy near zero [83-85]. Therefore, an attempt to apply Shockley's theory to explain the field dependence of the impact ionization coefficient in a-Se failed, resulting in unrealistic material parameters [86]. The main difference between the lucky drift model and the conventional (Shockley) model is that the lucky drift allows carriers to scatter between impact ionization events. This results in a higher

probability for build-up sufficient energy (by drifting in the electric field) to initiate impact ionization.

Kasap et al. [87] proposed that the lucky drift model of McKenzie and Burt [30] should be applied to a-Se to understand the mechanism of impact ionization in this material. They were able to demonstrate that band-to-band excitation can explain the general observations with an energy relaxation length of ~ 4nm. Rubel et al. [29] extended the theory to describe field-dependent impact ionization coefficient of holes in a-Se by relating the momentum relaxation mean free path with the energy relaxation mean free path in the original lucky-drift model of McKenzie and Burt [30]. However, this model assumed field-independent momentum relaxation mean free path and showed a stronger field dependence of impact ionization than the experimental observations [29].

Assuming energy-independent scattering mean free paths and utilizing Mckenzie and Burt's formulation of the lucky drift model, the impact ionization coefficient (for both holes and electrons) is given by [29, 30]

$$\alpha = \frac{1}{\lambda_E} \frac{\exp\left(-\frac{l_0}{\lambda_E}\right) - \frac{\lambda_m}{\lambda_E}\exp\left(-\frac{l_0}{\lambda_m}\right)}{1 - \exp\left(-\frac{l_0}{\lambda_E}\right) - \left(\frac{\lambda_m}{\lambda_E}\right)^2\left[1 - \exp\left(-\frac{l_0}{\lambda_m}\right)\right]} \tag{3.10}$$

where λ_m is the momentum relaxation mean free path and λ_E is the energy relaxation mean free path . If only holes undergo impact ionization, the avalanche multiplication gain g_{av} depends exponentially on the a-Se layer thickness L and α_h that is the impact ionization coefficient for holes, by $\exp(\alpha_h L)$ [14, 26].

Let us assume that initially a charge carrier is located at the origin of a coordinate system and has no kinetic energy, as illustrated in Figure 3-3. While drifting under the influence of an applied electric field, the charge carriers undergo two scattering mechanisms: (i) elastic scattering by the disorder potential, which is characterized by the energy independent elastic mean free path λ_m and (ii) inelastic scattering via phonon emission where the kinetic energy of the charge carriers becomes greater than the optical phonon energy E_p. The specific distinction

between the rate of momentum relaxation and energy relaxation is that after elastic scattering, the electron relaxes its momentum without relaxing its energy. On the other hand, after inelastic scattering, both momentum and energy of carriers are relaxed. The scattering due to the disorder potential is the dominant mechanism for the momentum relaxation for energetic carriers. The impact ionization takes place immediately after the carriers gain the kinetic energy equal to the ionization threshold energy E_i. The energy relaxation mean free path λ_E is defined as the average distance traveled by a carrier in the field direction prior to the full energy relaxation (i.e., $eF\lambda_E$ is the average carrier energy).
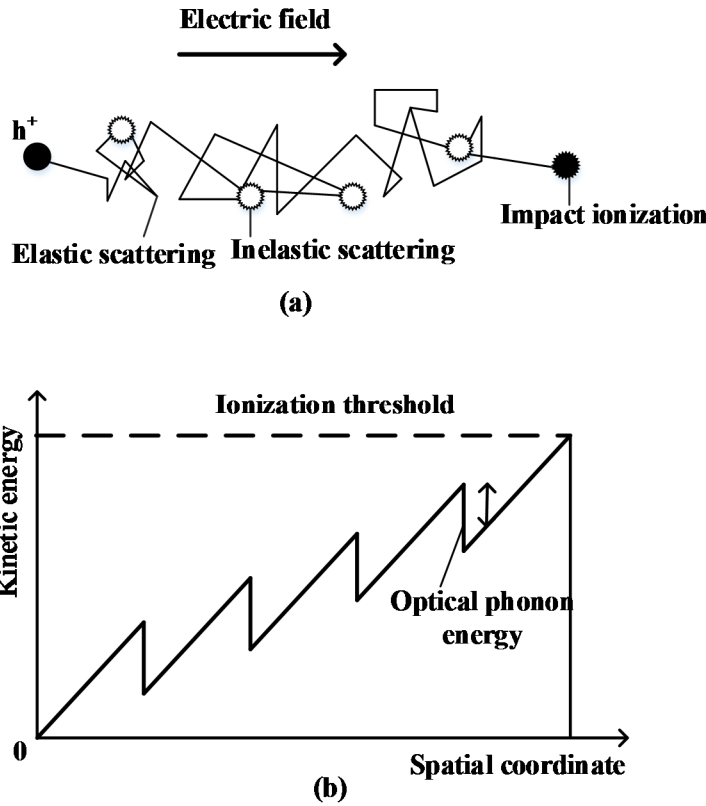
Figure 3-3 (a) Carrier trajectory with relevant scattering processes and (b) the corresponding energy diagram [29].

The energy relaxation mean free path λ_E is related to λ_m as [29]

$$\lambda_E = \frac{eF\lambda_m\lambda_{op}}{2E_p}, \tag{3.11}$$

where E_p is the optical phonon energy and λ_{op} is its corresponding mean free path ($\lambda_{op} \geq \lambda_m$).

Ridley proposed a simple empirical expression relating λ_{op} and E_p as [80]

$$\lambda_{op} \approx 60 \frac{\rho E_p}{\sqrt{E_i}} nm \tag{3.12}$$

where ρ (material density) is in g cm^{-3} and the energies are in eV.

The drift mobility is proportional to the momentum relaxation mean free path. Because the drift mobility increases with temperature, so does λ_m. The extended state carriers have higher kinetic energy and a higher rate of collisions at extremely high fields, and thus, have a lower momentum relaxation mean free path λ_m. The field and temperature-dependent λ_m for the carrier can be written as

$$\lambda_m(F,T) = \lambda_m(0) \frac{\mu(F,T)}{\mu(F,T_r)} \left(\frac{T_{eff}}{T} \right)^{-1/2}, \tag{3.13}$$

where $\lambda_m(0)$ is the zero-field momentum relaxation mean free path without considering carrier heating at room temperature (T_r). At T_r, the field-dependent λ_m can be expressed as

$$\lambda_m(F,T_r) = \lambda_m(0) \left(\frac{T_{eff}}{T_r} \right)^{-1/2} \tag{3.14}$$

3.3 Results and discussions

3.3.1 Effective Hole mobility

The proposed model for the shallow trap-controlled effective hole mobility is compared with the published measured data in order to validate the mechanisms of the field-dependent effective mobility versus field. The DOS at the conduction band edge, $g_c = g_v = 4 \times 10^{20}$ cm^{-3} eV^{-1}, $\varepsilon_r = 6.7$, $T_0 = 275$ K (for both band edges) [46, 70], and $\Delta E_m = 0.05$ eV are taken in all calculations. Figure 3-4 shows the effective hole drift mobility as a function of the applied electric field. The symbols, solid, and dashed lines represent the experimental results, the proposed model fit considering the TAT trap release, and the model fit considering the 3D PF trap release (with $E_m = 0.44$ eV), respectively. The experimental field-dependent effective mobility data have been extracted from Figure 3 of Bubon et al.'s work [25]. The drift mobility

was measured in ITO/CeO$_2$/a-Se/Sb$_2$S$_3$/Au and ITO/CeO$_2$/a-Se/Sb$_2$S$_3$/RIL/Au detector structures, where the RIL (resistive interface layer) layer is ~1 μm thick semi-insulating polymer, namely cellulose acetate. As is evident from Figure 3-4, the proposed model considering the TAT trap release and carrier heating gives the best fit (the solid line in Figure 3-4) to the experimental results whereas the Poole-Frenkel release mechanism fails to fit the experimental data. Therefore, the thermally activated tunneling trap release and carrier heating will be considered in the rest of the calculations of this model. The best-fit parameters are, E_m = 0.265 eV, a_{eff}=1.2 nm, $b_t = \beta/3$, μ_{0h} (0) = 2.6 cm^2/Vs, and r_{tv} = 2.25 × 10^{-5} (e.g., N_m = 10^{16} cm^{-3} eV^{-1}) [70]. The Gaussian peak at 0.265 eV in the present result is consistent with the previous observations [27, 70, 88]. The hole drift mobility in crystalline selenium is in the range of ~20 cm^2/V s [52]. The extended states mobility (microscopic mobility) in a-Se can be reduced (almost an order of magnitude) through elastic scattering due to the disorder potential inherent to amorphous solids. The TAT mechanism applies when the unoccupied defect is neutral, while the PF model applies when the unoccupied defect is a charged defect. The present result indicates that the shallow hole traps close to the band edges are neutral defects in a-Se.
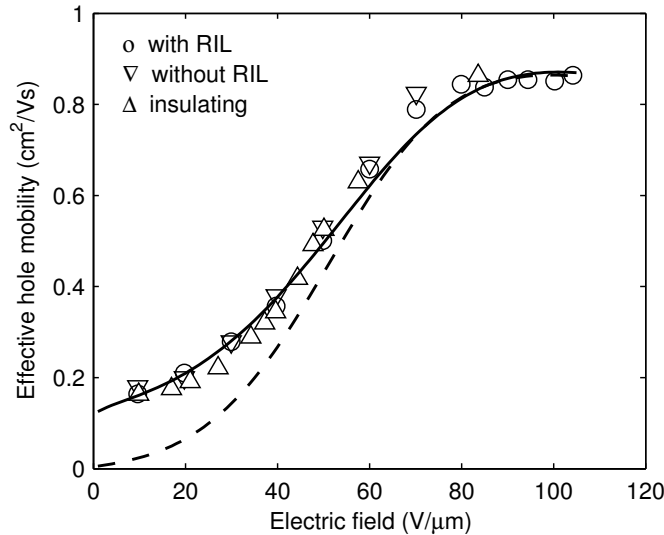
Figure 3-4 The effective hole drift mobility as a function of the applied electric field at room temperature. Symbols: experimental data [25], dashed lines: model fit considering 3D PF trap release and solid lines: model fit considering TAT trap release.

Berashevich et al. [89] calculated the peak energy positions of VAP (D$^-$) and IVAP defects near the VB edge by a first-principle method, which are 0.34 eV and 0.23 eV,

respectively, above the VB mobility edge. Benkhedir et al. [46] reported that the defects at 0.2 eV are neutral whereas those at 0.38 eV are charged defects, which are consistent with the present results (i.e., a Gaussian peak at 0.265 eV is most probably the IVAP type neutral defect [89]).
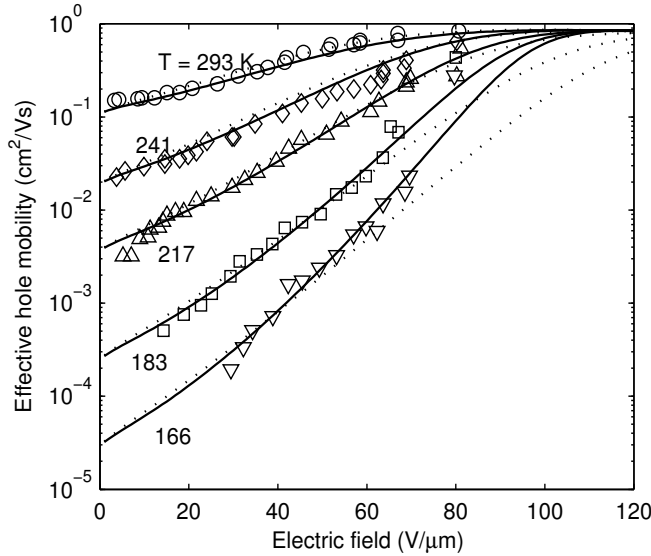
Figure 3-5 Field dependence of the effective hole mobility at five different temperatures. Symbols: experimental data [26], dotted lines: model considering b_t=0 [90], and solid lines: model fit to the experimental data.

Figure 3-5 shows the effective hole mobility versus the electric field at five different temperatures. The symbols, dotted and solid lines represent the experimental data, model considering b_t=0 [90], and the present model fit to the experimental data, respectively. The experimental data are extracted from Figure 2 of [26]. The drift mobility measurement results of [25] and [91] at T_r are surprisingly very close. As is evident from Figure 3-5, the present model considering the TAT trap release and carrier heating gives the best fit (the solid line in Figure 3-5) to the experimental results. The fitting parameters in Figure 3-5 are the same as in Figure 3-4 except for r_{tv} at low temperatures. The fitted values of r_{tv} decrease at lower temperatures (r_{tv} = 1.75×10^{-5}, 0.75×10^{-5} and 0.6×10^{-5} for T = 217, 183 and 166 K, respectively). The mobility gap E_g of a-Se is sensitive to temperature; it decreases with increasing temperature [92]. Therefore, longer tails and an exponential increase of g_v (i.e, lower r_{tv}) with the energy length of the tail states are expected at very low temperatures. The defect densities may also decrease with decreasing temperature [44], which can also reduce r_{tv} at low temperatures. Note that this

temperature-dependent mobility cannot be explained by considering only the exponential tail-state (ignoring the second term in Equation 3.1). The fitted DOS near the VB in a-Se for the above temperatures are shown in Figure 3-6. The slight decrease of defect states at lower temperatures is consistent with the previously reported results [44].
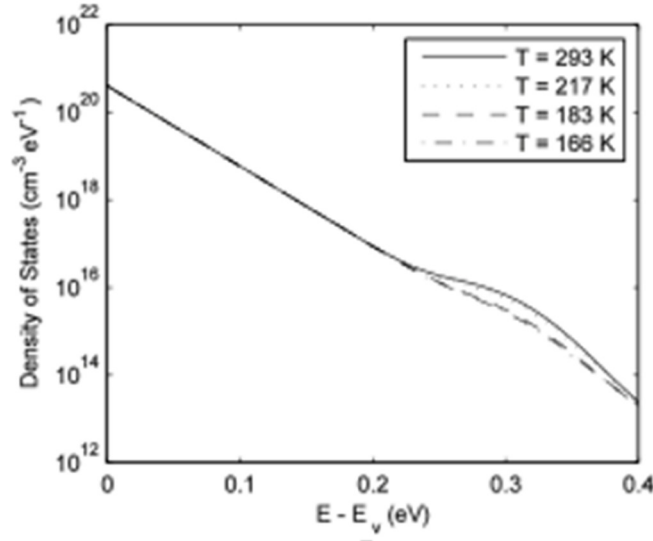
Figure 3-6 The DOS distributions of shallow states near the valence band at different temperatures.

The effective hole mobility at room temperature is well-defined and independent of the preparation of the sample [25, 26]. Therefore, for a faster calculation, it is instructive to propose a relatively simple empirical expression for the effective hole mobility in a-Se at T_r. An empirical relation for the effective hole mobility in a-Se at T_r can be expressed by the fitting experimental results, which is

$$\mu_h(F,T_r) \approx 0.127 + \frac{0.745}{1 + \exp[-(F-48)/11.5]} \tag{3.15}$$

where F is the electric field in V/μm and μ_h is in cm^2/Vs.

3.3.2 Hole Impact Ionization coefficient

The better fitting of the effective mobility considering the field-dependent microscopic mobility indicates that λ_m decreases with increasing F. This point is further strengthened by a fitting of the model with the experimental α versus F curves. Recently, Reznik et al. [14]

vigorously measured α for holes in various samples at room temperature and plotted as α_h vs $1/F$. These sets of experimental results are surprisingly quite close as shown in Figure 3-7. The symbols represent the experimental results, the solid line represents the proposed model considering field-dependent λ_m (Equation 3.13), and the dashed line represents Rubel et al.'s model (field-independent λ_m, with $\lambda_m = 0.5$ nm and $\lambda_{op} = 4.3$ nm) [29]. The experimental data are extracted from the published results of Reznik et al. [14]. The dominant optical phonon energy in a-Se is 31 meV. The ionization threshold E_i for holes is taken as 2.3 eV [29]. Ridley proposed a simple empirical expression relating λ_{op} and E_p [80] which gives $\lambda_{op} = 5.3$ nm. The best fit values are $\lambda_m(F=0) = 1.0$ nm and $\mu_0(0) = 2.5$ cm^2/Vs, in the present model. As evident from Figure 3-7, the present model shows a very good agreement with the experimental results. This indicates that λ_m decreases with increasing F at extremely high fields due to carrier heating. The estimated values of λ_m and λ_E as a function of F at room temperature are shown in Figure 3-8. At a fixed temperature, λ_m decreases with increasing F and the λ_E vs F curve is sublinear.
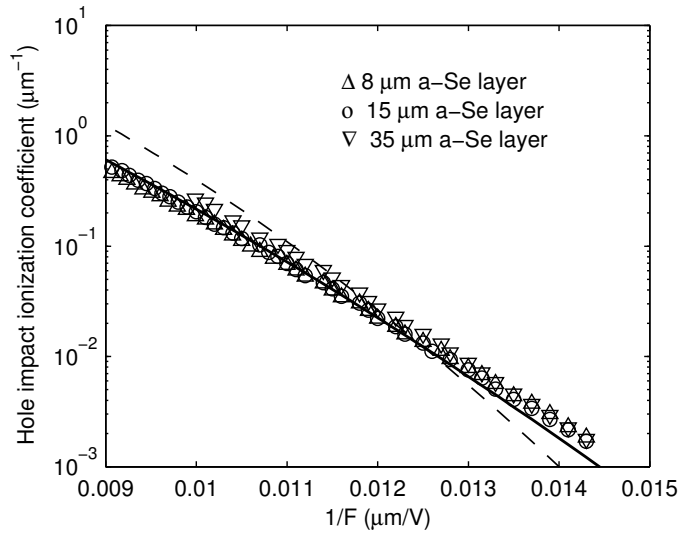
Figure 3-7 The hole impact ionization coefficient as a function of electric field. Symbols: experimental data [14], dashed line: Rubel et al.'s model [29], and solid line: proposed model fit to the experimental data.

51
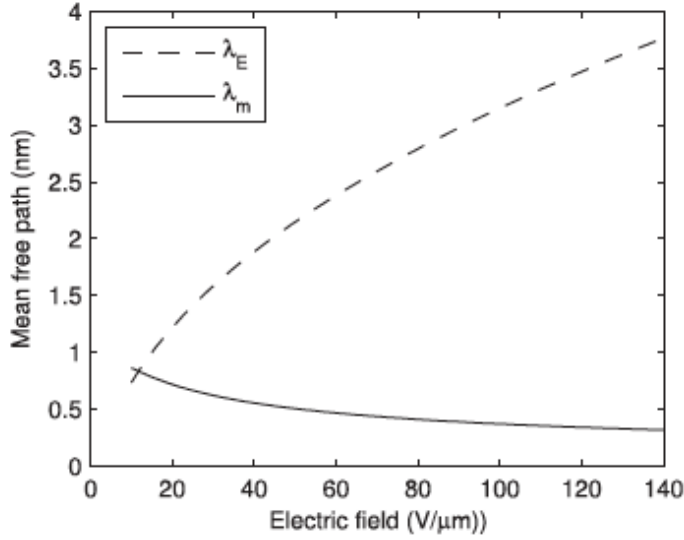
Figure 3-8 Momentum and energy relaxation mean free paths as a function of electric field.

The impact ionization coefficient increases with increasing temperature, which is opposite to that in crystalline semiconductors. The effective drift mobility in a-Se is controlled by shallow traps and thus λ_m increases with increasing temperature as described by Equation (3.13).

Tsuji *et al.* [77] measured α_h at various temperatures. The proposed model is compared with the experimental data on α_h versus temperature curves, which is shown in Figure 3-9. The symbols and solid lines represent published experimental data, and the present model fits to the experimental data, respectively. The ionization threshold E_i is taken as 2.45 eV. The fitted values of r_{tv} = 1.75 × 10^{-5}, 1.75× 10^{-5}, 0.8 × 10^{-5} and 0.55 × 10^{-5} for T = 295, 223, 174 and 148 K, respectively, which are consistent with those in Figure 3-5. All other parameters in Figure 3-9 are the same as in Figure 3-4 except a_{eff}=1.1 nm, and $b_t = \beta/4$. The E_g of a-Se has been reported to be 2.0 − 2.3 eV, and the precise value depends on the particular sample and type of measurement approach [92, 93]. While $E_i \sim 1.5E_g$ in crystalline semiconductors [80], the average E_i in amorphous semiconductors can be close to E_g considering carrier generation from the localized states within the mobility gap. The average value of E_i may vary slightly in different samples because of some variations of the DOS distribution. Therefore, $E_i \approx 2.3 − 2.45$ eV in this work can be considered as a reasonable fit value, and the agreement between the experimental data and theory is satisfactory.
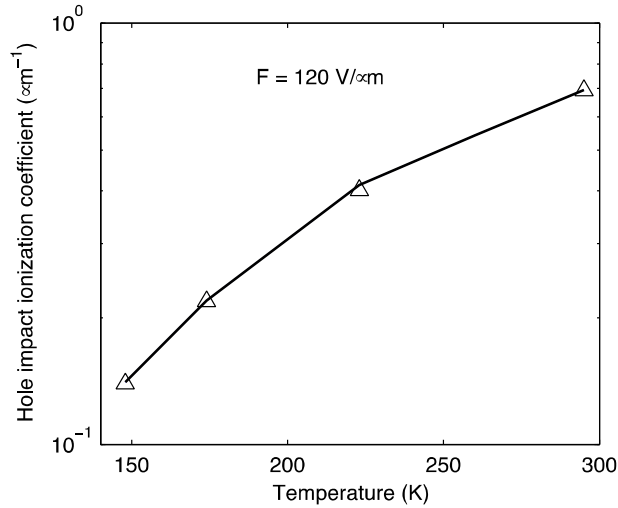
Figure 3-9 The hole impact ionization coefficient as a function of temperature. Symbols: experimental data [77] and solid line: proposed model fit to the experimental data.

3.3.3 Effective electron mobility

Similarly in this section, the proposed model for the shallow trap-controlled effective electron mobility is compared with the published measured data in order to validate the mechanisms of the field-dependent effective mobility versus field. Figure 3-10 shows the effective electron mobility versus electric field at four different temperatures. The symbols and solid lines represent the experimental data and model fit to the experimental data, respectively. The experimental data are extracted from Figure 3 of [26]. As is evident from Figure 3-10, the present model considering the TAT trap release and carrier heating shows a reasonable fit to the experimental results. The best-fit parameters are, $E_m = 0.38$ eV, $a_{eff} = 0.65$ nm, $b_t = C/3.5$, μ_{0e} (0) = 1 cm^2/Vs, and r_{tc} (= N_m/g_c) = 6.75×10^{-6}, 3.63×10^{-6}, 2.38×10^{-6} and 1.5×10^{-6} for T = 293, 265, 247 and 227 K, respectively. The fitted DOS distributions near the CB in a-Se for the above temperatures are shown in Figure 3-11. The DOS distributions for the shallow electron traps are consistent with the measured values [48]. The present result indicates that the shallow electron traps are also neutral defects in a-Se. Benkhedir et al. [94] reported that the defects at 0.28 eV below the CB edge are neutral whereas those at 0.53 eV are charged defects, which are consistent with the present results (i.e., a Gaussian peak occurs at 0.38 eV below the CB edge and these are the neutral defects in present analysis). As evident from Figures 3-6 and 3-11, the

Gaussian peak in the DOS near conduction band is more pronounced than that near the VB, which are consistent with the previous observations [48, 88].
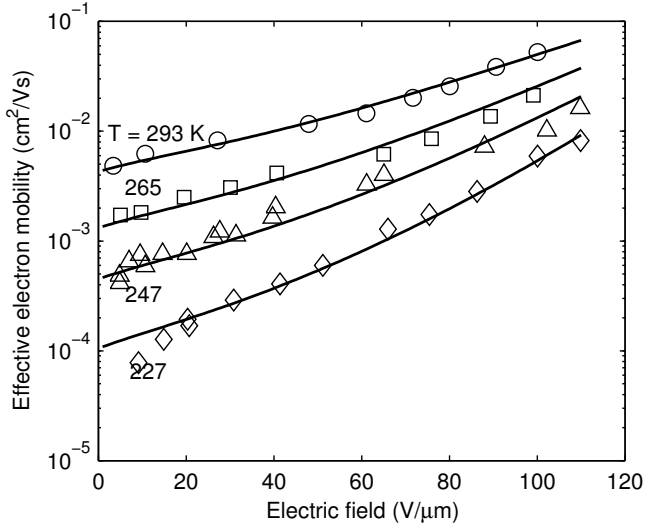
Figure 3-10 Field dependence of the effective electron mobility at four different temperatures. Symbols: experimental data [26] and solid lines: model fit to the experimental data.
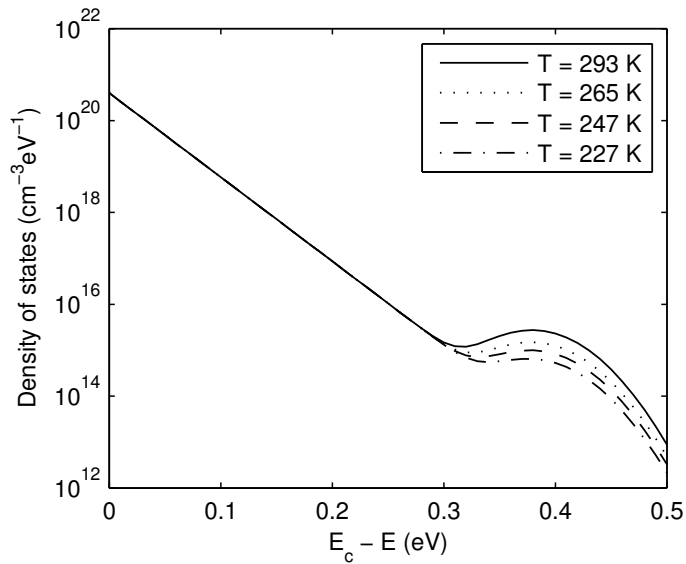
Figure 3-11 The DOS distributions of shallow states near the conduction band at different temperatures.

3.3.4 Electron Impact Ionization coefficient

Tsuji *et al.* [77] measured α for electrons as a function of electric field. Figure 3-12 shows the impact ionization coefficient versus $1/F$ for electrons at T_r. The symbols and the solid line represent the experimental results and the proposed model fit to the experimental data considering field-dependent λ_m (Eq. 3.13), respectively. The best-fit parameters for electrons are $E_i = 2.9$ eV, and $\lambda_m (F=0) = 0.5$ nm. All other relevant parameters in Figure 3-12 are the same as in Figures 3-7 and 3-10. Note that the ionization threshold energy for electrons is higher than that for holes in a-Se because of higher scattering rate (i.e., lower mobility) for electrons. The unequal ionization energies for electrons and holes for other materials are also reported in the literature [80]. As evident from Figures 3-10 and 3-12, the present models also agree well with the experimental electron transport properties.
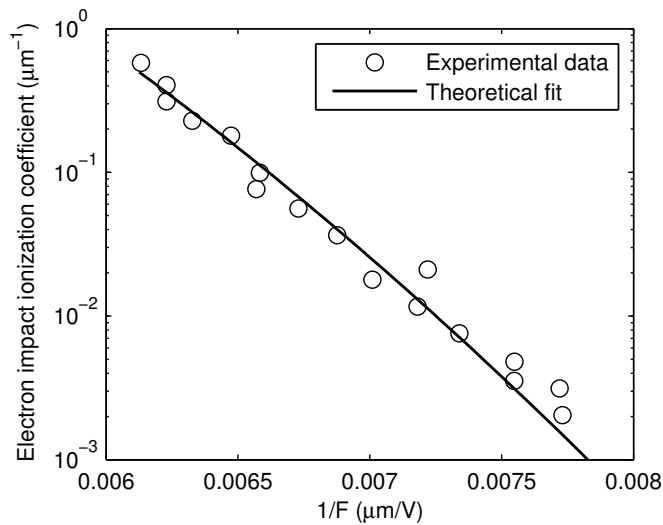
Figure 3-12 The electron impact ionization coefficient as a function of the electric field. Symbols: experimental data [77] and solid lines: model fit to the experimental data.

3.4 Conclusions

The effective drift mobility at extremely high fields is controlled by the shallow traps and carrier heating effects. The field enhancement of the release rate from the shallow traps is due to the thermally assisted tunneling effect, which indicates that the unoccupied shallow traps for both holes and electrons in a-Se are neutral defects. The momentum relaxation mean free path in

a-Se decreases with increasing electric field and decreasing temperature, which has remarkable effects on the field and temperature-dependent impact ionization coefficient in a-Se.

Chapter

4. Mechanisms of charge photogeneration in amorphous selenium under high electric fields

4.1 Introduction

Amorphous selenium is widely used in direct conversion X-ray detectors [12, 95] and a highly promising photoconductor for optical light detection in very high-gain indirect conversion avalanche X-ray detectors [96]. However, charge carrier transport and carrier photogeneration mechanisms in a-Se at very high electric fields are not yet clearly understood [13, 97]. In this thesis, the physical mechanisms for the excitation wavelength and electric field dependent charge carrier photogeneration in amorphous selenium under high electric fields, considering geminate recombination at non-zero reaction radius within the scope of Onsager theory are investigated. Although the photogeneration efficiency at low to moderate electric fields in a-Se has been most successfully described through the conventional Onsager theory of dissociation, this theory fails at very strong electric fields. Therefore, a formulation for calculating the excitation wavelength and electric field dependent initital separation of the photogenerated and thermalized geminate electron and hole is developed, and applied to explain the field-dependent photogeneration efficiency in a-Se. Furthermore, the exact extension of the Onsager model is adapted in order to explain the experimental results at very strong electric fields. The theoretical results are compared with the experimental data.

4.2 Analytical Models

4.2.1 Onsager Model

One of the characteristic features of amorphous semiconductors is the low carrier mobility, which results from small carrier mean free-path due to disorder potential. When the carrier mean free path becomes comparable to the Coulomb radius of an electron hole pair, both photogeneration and recombination process can be affected. The photogeneration process can be

controlled by geminate or initial pair recombination that results in field dependent photogeneration efficiency.

The conventional Onsager theory of dissociation successfully described the photogeneration efficiency at low to moderate electric fields. However, this theory fails at very strong electric fields [32].

Reznik et al. attempted to explain the failure of the Onsager theory at strong electric fields by adapting original Tachiya's model [98] for molecular liquids when the electron mean free path l is much higher than the Onsager length r_c (defined by the distance at which the coulomb energy is equal to k_BT), where $r_c = e^2/4\pi\varepsilon k_BT$, e is the elementary charge, ε is the permittivity of a-Se, k_B is the Boltzmann constant, and T is the absolute temperature. They had to increase the scattering time τ almost exponentially (Figure 4 of [32]) with increasing field from 10 to 110 V/μm in order to fit the experimental results, which is unrealistic (note that the effective mobility of holes saturates at ~ 80 V/μm) [25]. There exists a number of flaws in their adaptation of Tachiya's model in a-Se [98]. These are as follows: (1) they have assumed that the hole is fixed and only the electron is mobile but both are mobile in semiconductors. (2) The mean free path of both electrons and holes in a-Se is less than 0.5 nm [87, 97] at $F > 50$ V/μm and $r_c \approx 9$ nm (for the relative static dielectric constant of 6.3 in a-Se [99]). Therefore, the mean free path is much less than the Onsager length, which contradicts the necessary condition of Tachiya's model [98]. Though the effective mobility μ in a-Se increases with increasing field because of shallow traps, it does not follow the microscopic mobility relation, $\mu = e\tau/m^* = el/m^*v_{th}$, where m^* is the effective mass of the carrier and v_{th} is the thermal velocity [97]. Considering $m^*=m_0$ (free electron mass), $v_{th} = 10^7$ cm/s and $\mu = 1$ cm^2/Vs, the microscopic mobility relation gives $l\sim0.05$ nm, which is 5 times less than the interatomic distance (0.23 nm in a-Se). In fact, the mean free path is in the range of 0.5 nm and it decreases with increasing electric field strength under very strong fields [97]. The scattering time should also follow the same behavior of the mean free path with the field.

The Onsager theory of geminate recombination gives the probability for a geminate pair to dissociate by Brownian motion in the presence of their Coulomb attraction and the applied

electric field [100]. The Onsager model assumes that the carrier mean free path is in the scale of the interatomic distance (which is the case for a-Se and organic materials) and the final step of the geminate recombination takes place at zero reaction radius [101] (reaction radius a_r is the minimum distance required between the bound electron and hole to recombine). However, it is believed that the final geminate recombination step proceeds on a sphere of radius a_r with a finite velocity v_r [102]. Moreover, r_0 is the only input parameter in the conventional Onsager model, which has been considered independent of the electric field.

As mentioned earlier in this thesis, in the theory of optical photons, each absorbed optical photon creates one electron-hole pair in a-Se. The excess kinetic energy carried by the electrons or holes is not sufficient to generate secondary electrons or holes and is presumed to be dissipated by exciting phonons. The process by which the electron-hole pair loses excess energy and reaches an equilibrium state is called the thermalization process. After the electron-hole pair is thermalized, the electron and hole are separated by a distance r_0, at an angle θ with respect to the applied electric field F. According to Onsager's theory, such a thermalized pair can either recombine (geminate recombination), or escape their mutual Coulomb attraction and separate into a free electron and a free hole, as illustrated in Figure 4-1 [103]. One can expect an increase of r_0 with increasing the kinetic energy of electrons or holes, and thus, with increasing the photon energy.
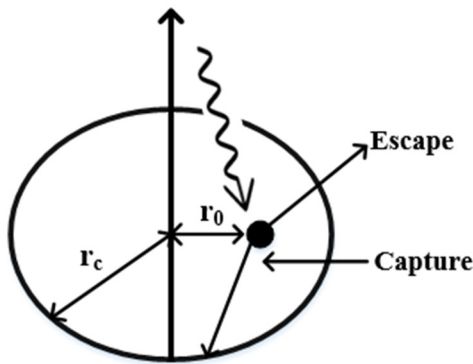
Figure 4-1 Schematic presentation of geminate recombination or initial recombination [103]. If the photoexcited EHP thermalize at a distance r_0 then recombination can occur even before free carrier creation occurs.

When considering a pair of interacting particles performing a diffusive motion, the probability density $w(r, t)$ that these particles are separated by distance r at a time t is described by the Smoluchowski equation [100].

$$\frac{\partial w(r,t)}{\partial t} = D[\nabla^2 w(r,t) + \frac{1}{k_B T} \nabla w(r,t) \nabla V(r)] \tag{4.1}$$

where D denotes the sum of diffusion coefficients of the particles, k_B is the Boltzmann constant, T is the temperature, and $V(r)$ is the interaction potential. If the initial distance between the two particles is r_0, the initial condition takes the form

$$w(r,0) = \frac{1}{4\pi r_0^2} \delta(r - r_0) \tag{4.2}$$

From a practical point of view, the most important quantity to be obtained from a geminate recombination theory is the probability ϕ that the geminate particles avoid mutual recombination and separate to a relatively large distance from each other, thus becoming free particles. This quantity, known as the escape probability, is related to $w(r, t)$ by

$$\phi = \lim_{t \to \infty} \int w(r,t) \, dr \tag{4.3}$$

Onsager solved the time-independent diffusion (Smoluchowski) equation for finding the dissociation probability ϕ and observed that ϕ can be obtained by solving the following equation [100],

$$\nabla^2 \phi - \frac{1}{k_B T} \nabla \phi \nabla V = 0 \tag{4.4}$$

The potential energy, V, is given by,

$$V(r) = -(\frac{e^2}{4\pi\varepsilon r} + eFr\cos\theta) \tag{4.5}$$

where r is the intrapair distance of the geminate pair.

The obvious first boundary condition for solving Equation (4.4) is $\phi\,(r = \infty) = 1$. The second boundary condition $\phi\,(r = 0) = 0$ was assumed by Onsager [100], which implies that the final step of geminate recombination takes place at a sphere of radius, $a_r = 0$. Under these two

boundary conditions, the solution of equation (4.4) is the well-known Onsager model for the dissociation probability [31],

$$\varphi(r, F, T, \theta) = e^{-A-B} \sum_{n=0}^{\infty} \sum_{m=0}^{\infty} \frac{A^m}{m!} \frac{B^{m+n}}{(m+n)!}$$

(4.6)

where $A = e^2/(4\pi \varepsilon r k_B T)$ and $B = eFr_0(1+\cos\theta)/2k_B T$. If the initial separation follows a certain spatial distribution function $g(r, \theta)$, the photogeneration efficiency is,

$$\eta = \eta_0 \int \varphi(r, F, T, \theta) g(r, \theta) d^3 r$$

(4.7)

Pai and Enck [31] have reported that the photogeneration efficiency in a-Se can be explained satisfactorily using a Dirac delta function distribution for r_0. Assuming unity production efficiency of thermalized ion pairs per absorbed photon ($\eta_0 = 1$) and $g(r, \theta) = \delta(r - r_0)/4\pi r^2$, the photogeneration efficiency may be expressed as [104]

$$\eta_{on}(r_0, F, T) = \frac{e^{-a-b}}{b} \sum_{l=1}^{\infty} l \left(\frac{b}{a} \right)^{1/2} I_l \left(2\sqrt{ab} \right)$$

(4.8)

where $a = e^2/(4\pi \varepsilon r_0 k_B T)$, $b = eFr_0/k_B T$ and I_l is the modified Bessel function. At zero field, the Equation (4.8) reduces to, $\eta_{On}(r_0, T) = \exp(-r_c/r_0)$,where $r_c = e^2/4\pi\varepsilon k_B T$ [31].

4.2.2 Modified Onsager Model

In this section, the exact extension of Onsager theory have been considered to study the photogeneration efficiency in a-Se at high fields considering geminate recombination at a nonzero reaction radius instead of a zero separation.

Wojcik and Tachiya [101] derived an expression for the average escape probability in the framework of Noolandi and Hong (NH) [105] by considering the final geminate recombination step proceeds on a sphere of radius a_r with a finite velocity v_r, which is termed as the exact extension of Onsager model (NH model is given in Appendix A). Thus, they solved Equation (4.4) under the boundary conditions, $\phi(r = \infty) = 1$ and D $(\partial\phi/\partial r) = v_r \phi$ at $r = a_r$, where $D = \mu_{\pm}/k_B T$

is the sum of the diffusion coefficients of the two particles. Thus, the photogeneration efficiency of the exact extension of Onsager model is given by [101]:

$$\eta_{NH}(r_0, F, T) = 1 - \frac{a}{\sqrt{2\pi}} \sum_{l=0}^{\infty} a_{l0} \beta_l Z_{2l}(\frac{2}{a}) Z_{2l}(\frac{2}{b}) \qquad (4.9)$$

where T_l is the generalized Legendre function of l order, $a_{l,0}$ are the coefficients of the expansion of T_l functions expanded into series of Legendre polynomials and Z_{2l} stands for the Z special function of the second kind of l order, which can be expressed as a relevant linear combination of Bessel functions [105] and is given by

$$Z_{2l}(\xi) = \frac{1}{\sqrt{F}} \frac{\pi e^{-F\xi/4}}{a_{l0}} \sum_{n=0}^{\infty} (-1)^n a_{ln} I_{n+(1/2)}(\frac{1}{\xi}) \qquad (4.10)$$

where $I_{n+(1/2)}$ are the modified Bessel functions of fractional order.

The approach in this thesis was to apply the Noolandi-Hong model for a-Se semiconductors by extending their model considering the reaction radius different than the initial separation $a_r \neq r_0$. Note that the effect of the reaction sphere radius is contained in β_l through the reduced reactivity parameter p ($p = v_r r_c / D$) and a_r, where v_r is the recombination velocity.

4.2.3 Field dependent geminate pair separation

For photon wavelengths ranging from 400 to 620 nm, Pai and Enck [31] found that the initial separation r_0 obtained by fitting experimental data varies from 7.0 to 0.84 nm. The electron-hole separation r_0 for a given photon energy can also be calculated using the approach of Knights and Davis [33].

Knights and Davis [33] proposed a simple theoretical relationship between r_0 and the excitation wavelength. They assumed that during the thermalization process the motion of carriers is diffusive, the excess kinetic energy to be dissipated is the excess over the local potential (Coulomb) rather than the excess over the bandgap, and the rate of energy dissipation to phonons is $h\nu_p^2$, where h is the Planck constant, $h\nu_p$ is the phonon energy, and ν_p is the phonon

frequency. That means, they have assumed that the average phonon emission rate is equal to v_p, but the phonon emission rate may not be the same as the phonon frequency.

On the other hand, the thermalization time t is related to the separation r_0 and the diffusion constant D through the relation $r_0=(Dt)^{1/2}$. The rate of loss of energy in an amorphous material is expected, from the relaxation of k-conservation in inelastic scattering, to reach its maximum of a phonon frequency times a typical phonon energy. The excess kinetic energy to be dissipated is taken to be in excess over the local potential (Coulomb) rather than the excess over the band gap is given by

$$K.E = (hv - E_g) + \frac{e^2}{4\pi\varepsilon r_0} + eFr_0 \cos\theta \tag{4.11}$$

The time taken to dissipate this energy is then

$$t = \frac{(hv - E_g) + \dfrac{e^2}{4\pi\varepsilon r_0} + eFr_0 \cos\theta}{hv_p^2} \tag{4.12}$$

Therefore, the electron-hole separation r_0 at the end of the thermalization process is a solution of the equation

$$\frac{r_0^2}{D} = \frac{(hv - E_g) + \dfrac{e^2}{4\pi\varepsilon r_0} + eFr_0 \cos\theta}{hv_p^2} \tag{4.13}$$

Considering that the average phonon emission rate is different from v_p, and following the approach of Knights and Davis [33], the Equation (4.13) for r_0 can be modified as,

$$\frac{r_0^2}{D}\frac{hv_p}{\tau_{av}} = \left(hv - E_g\right) + \frac{e^2}{4\pi\varepsilon r_0} + eFr_0 \cos\theta \tag{4.14}$$

where v is the frequency of the incident optical photon, E_g is the mobility gap of a-Se, τ_{av} is the average phonon scattering time and, alternately, $1/\tau_{av}$ is the average phonon emission rate. The phonon DOS in a-Se consists of a strongest peak at 31 meV, which is due to the optical phonon. There are other peaks at 5 meV (acoustic phonon) and 16 meV (optical phonon) [50]. During the thermalization process, one can expect phonon emissions of various energies [106]. The actual phonon emission rates of various phonons are unknown in a-Se. Therefore, the average phonon

energy and emission rate are considered as lumped parameters in Equation (4.14). The term $eFr_0\cos\theta$ is positive in the hemisphere $0 < \theta < \pi/2$ and the electric field enhances the initial separation r_0. Both geminate electrons and holes can move during the thermalization process and the electric field can have only a positive effect on their separation [33]. Considering isotropic carrier motion and averaging the term $eFr_0\cos\theta$, Equation (4.14) becomes

$$\frac{r_0^2}{D}\frac{h\nu_p}{\tau_{av}} = \left(h\nu - E_g\right) + \frac{e^2}{4\pi\varepsilon r_0} + \tfrac{1}{2}eFr_0 \tag{4.15}$$

4.3 Results and discussions

The photogeneration efficiency of the NH model (η_{NH}) are compared with the conventional Onsager model (η_{On}) with application to a-Se. The only parameter in the Onsager model is the initial separation r_0, which is usually chosen as a fitting parameter. The excitation wavelength of 550 nm is considered and the initial separation r_0 is taken as 1.5 nm for this wavelength [31, 32]. The effects of the final recombination radius a_r and velocity v_r on the photogeneration efficiency of NH model is shown in Figure 4-2. The photogeneration efficiency increases with decreasing the recombination velocity and increasing the reaction radius. For faster recombination proceeding on a sphere of small radius, the NH model approaches the Onsager model except at extremely high electric field. At extremely high electric fields (~ 100 V/μm), the NH model gives higher photogeneration efficiency than the Onsager model. The experimental evidences have indicated that the photogeneration efficiency at low to moderate electric field in a-Se follows the Onsager model. This implies that the reaction radius should be smaller where the escape probability is only dependent on p at extremely high fields, as the case in Figure 4-2 (c).

(a)

(b)

(c)
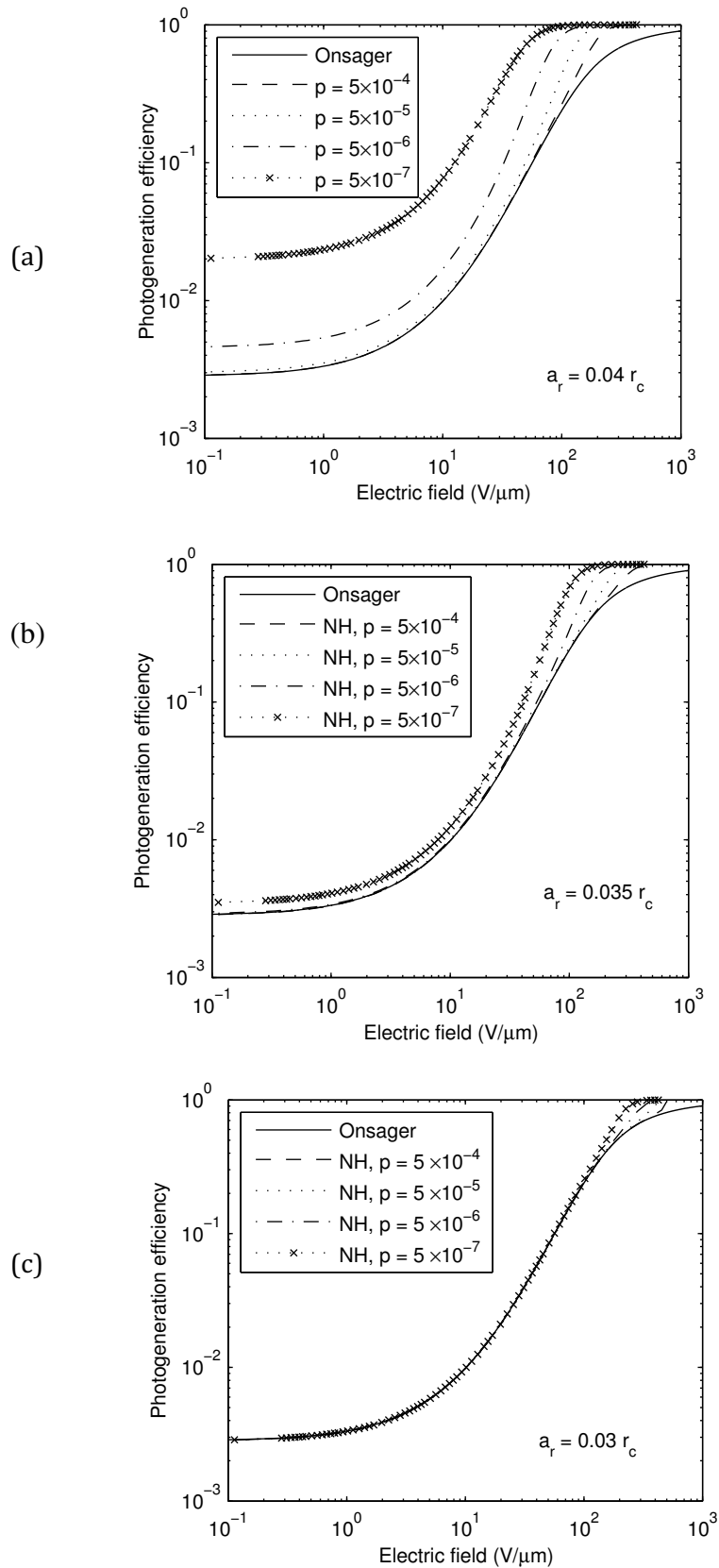
Figure 4-2 Photogeneration efficiency versus electric field obtained using NH model with various values of reduced reactivity parameter p ($p = v_r r_c/D$) and different values of the recombination sphere radii are as indicated in the parts (a), (b) & (c). For comparison, the result (solid line) of the conventional Onsager is also shown.

The results of the NH model are compared with the experimental data. Recently, Reznik et al. [32] measured the photogeneration efficiency at very high fields for excitation wavelengths from 430 nm to 600 nm. Figure 4-3 shows the photogeneration efficiency as a function of the electric field for light excitation at different wavelengths. The symbols, dashed and solid lines represent experimental data, conventional Onsager and NH models, respectively. The experimental data were extracted from Figure 2 of Reznik et al.'s work [32]. Excitation of lower wavelength light leads to higher r_0 and higher η, which agrees with the thermalization mechanism of initial EHPs having higher kinetic energy. The variation of r_0 with wavelengths in the Onsager model are almost exactly the same as in previous publications [31, 32]. The values of r_0 are 5.6, 2.2, 1.53, 1.16 and 0.95 nm for the excitation photon wavelengths of 430, 520, 550, 580 and 600 nm, respectively. The recombination radius is set to 0.28 nm so that the photogeneration efficiency just follows the Onsager model at low to moderate fields, irrespective of p. Note that this recombination radius is close to the average interatomic distance (0.23 nm) in a-Se [101, 102]. The fitted value of p is 7.5×10^{-7} for all the wavelengths. The exact extension of the Onsager model agrees quite well with the experimental results. Taking extended state hole mobility of 2.5 cm^2/Vs (at high electric field, the effect of shallow trapping is negligible) and using Einstein relation, $D = \mu k_B T/e$ at room temperature, the reaction velocity v_r becomes 0.054 cm/s, which is in the same order in some organic materials [107, 108].

Figure 4-3 Photogeneration efficiency as a function of electric field for various wavelengths of light excitation. Symbols: experimental results [32], solid lines: NH model and dashed lines: conventional Onsager model.

The Onsager model fits well for all excitation wavelengths at electric field $F \leq 50$ V/μm and underestimates the photogeneration efficiency at $F \geq 50$ V/μm if the initial separation r_0 is assumed to be independent of the electric field. In fact, r_0 should increase with increasing field if Equations (4.14) or (4.15) are correct. For $F \leq 50$ V/μm, the field-dependent term is much lower than the potential energy term in Equation (4.15) and it becomes significant at $F \geq 50$ V/μm. The experimental results of Reznik et al. [32] considering the field-dependent r_0 are fitted in Equation (4.15), which is shown in Figure 4-4. The symbols, dashed and solid lines, represent experimental data, field-independent and field-dependent r_0 in the conventional Onsager model, respectively. The parameters $E_g = 2.2$ eV and $h\nu_p = 31$ meV are taken in the calculations. As evident in Figure 4-4, the Onsager model considering field dependent r_0 can also fit the experimental results. The corresponding field-dependent r_0 is shown in Figure 4-5. The fitted values of the average phonon emission rates are 5×10^{12}, 1.5×10^{13}, 2×10^{13}, 2.32×10^{13}, 2.5×10^{13} s^{-1} for the excitation photon wavelengths of 430, 520, 550, 580 and 600 nm, respectively. The scattering rate decreases with decreasing photon wavelength and thus it decreases with increasing kinetic energy of the initial EHPs, which is the case in polar optical phonon scattering [109].

67

The phonon spectra of crystalline trigonal (γ-Se) and amorphous selenium phases are very similar [50] with the high-energy peak at 29 and 31 meV for γ-Se and a-Se, respectively. The part of the mobility that is controlled by electron-phonon interactions is the same for amorphous and crystalline state of the material [51]. Trigonal Se is an example of reststrahlen-displaying elemental crystal [52]. The unit cell of γ-Se consists of three atoms and it shows a net unit-cell electric moment. Its phonon scattering behavior is qualitatively similar to the ionic crystals and thus polar-mode scattering has a very significant influence on the carrier transport. The present result agrees well with its polar-mode scattering behaviour.
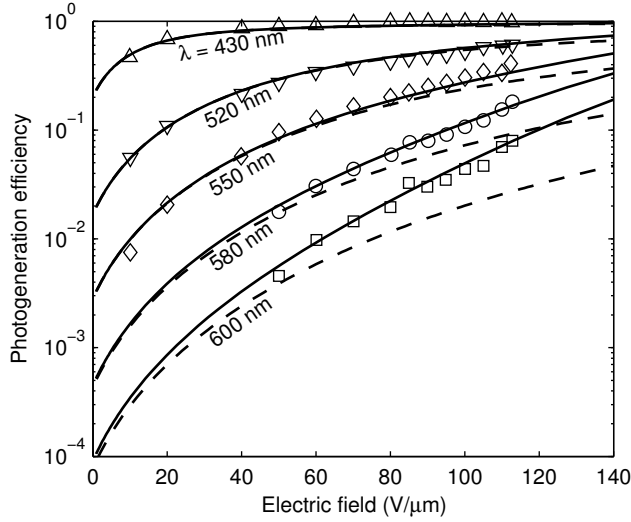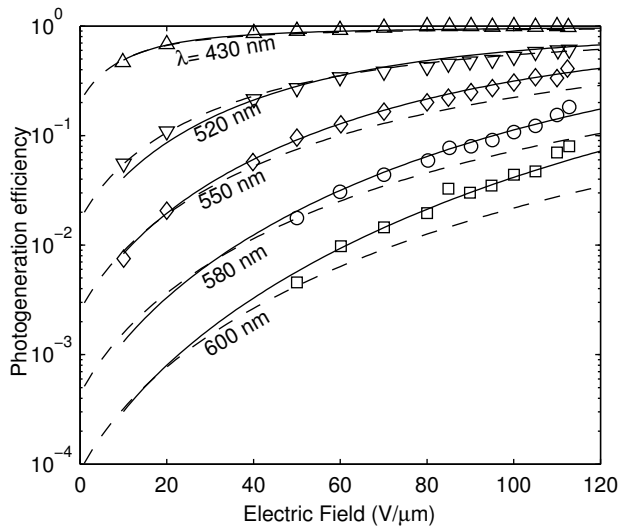

Figure 4-4 Photogeneration efficiency versus electric field for various wavelengths of light excitation. Symbols: experimental results [32], dashed lines: conventional Onsager model with field independent r_0 and solid lines: conventional Onsager model with field dependent r_0 using Equation (4.15).
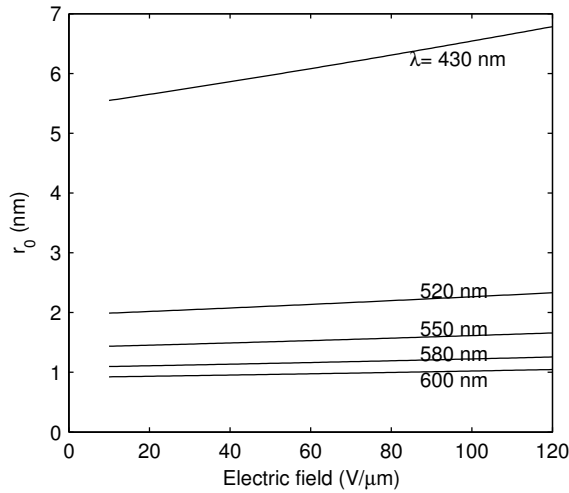
Figure 4-5 Initial EHP separation r_0 as a function of electric field using Equation (4.15) for various wavelengths of light excitation.

As is evident from Figures 4-2 and 4-4, both the exact extension of the Onsager model (NH model), and the conventional Onsager model with field-dependent initial separation, r_0, are able to explain excitation wavelength and field-dependent photogeneration efficiency in a-Se. However, the NH model shows a better fitting with the experimental results and, also, it gives the same results as the conventional Onsager model at low to moderate fields, which is consistent with the previous publications [31, 32]. Although the conventional Onsager model with field-dependent initial separation r_0 shows a quite close fit to the experimental results, one can expect that equation (4.14) is an over simplified formulation to the complicated thermalization process [32]. Still equation (4.15) can give quite close theoretical estimation for the values of r_0.

Lastly, it can be clearly seen from all the above figures, that the wide range of applied electric field strengths used, the shape and magnitude of the quantum efficiency variation is unique at each wavelength. Therefore, the fitting of the experimental data was done without any ambiguities as to the value of r_0 required to obtain the best fit at each wavelength. The physical meaning is that, irrespective of the exciting wavelength, each absorbed photon creates a thermalized pair of carriers, and at a given field, a certain fraction $\eta(F)$ of them dissociate into free carriers and the remaining $[1-\eta(F)]$ recombine. This means, that even for long-wavelength excitation, the number of thermalized pairs is equal to the number of absorbed photons, while the

low efficiency of production of free carriers at any field is due to the small distances between carriers in the thermalized pairs.

4.4 Conclusions

In this project, it has been shown that the exact extension of the Onsager Theory (Noolandi-Hong model) of the photogeneration efficiency justifies the electric field, excitation wavelength dependent photogeneration efficiency in amorphous selenium. In addition, a modification has been done to the model for the initial separation of the thermalized geminate electron and hole originally proposed by Knights and Davis, and has been applied to explain field dependent photogeneration efficiency in a-Se. Both the NH model and the conventional Onsager model with field-dependent initial separation r_0 are able to explain excitation wavelength and field-dependent photogeneration efficiency in a-Se, though the NH model shows a better and logical fitting with the experimental results.

Chapter

5. Modeling of X-ray generated free electron-hole pair creation energy in amorphous selenium at high electric field

5.1 Introduction

Amorphous Selenium is a semiconductor which photoconducts upon irradiation with optical or X-ray photons, which is employed in photocopy technology and medical X-ray imaging [110]. The EHP creation mechanism in a-Se under X-ray photon excitation is not yet clearly understood, and the extensive applications of a-Se in medical X-ray imaging have created the need to understand these properties much better. While there should be no dispute that recombination of electron-hole pairs created by X-rays is present in a-Se, the mechanism of recombination (or dissociation) of the X-ray generated charge carriers remains unclear despite its significance to both the fundamental a-Se science and operation of a-Se flat panel X-ray imaging detectors.

The recombination efficiency defines one of the crucial parameters of a-Se X-ray sensitivity through the effective electron-hole pair creation energy, which describes the amount of energy needed to produce a detectable electron-hole pair upon the absorption of an X-ray photon. Herewith, in this chapter, an analytical model is developed to study the mechanisms of X-ray generated free electron-hole pair creation energy in a-Se at high electric fields. The model is presented to show the electric field and temperature dependence of the charge extraction yield limited by the columnar recombination for the materials that have widely unequal drift mobility for electrons and holes, such as a-Se. The model is compared with Jaffe's columnar recombination model with widely varying field strengths and temperature. In addition, the free EHP creation energy is calculated by incorporating the initial charge extraction yield and the charge collection efficacy of the free carriers. Also, the results of this model are compared with

the recently published experimental results on EHP creation energy and a critical discussion on the appropriateness of various models is described.

Furthermore, the three dimensional continuity equations of both electrons and holes are numerically solved for calculating the charge extraction yield limited by the columnar recombination considering carrier drift, diffusion and bimolecular recombination between non-geminate electrons and holes. The aim of this work is to prove the accuracy of the analytical model since the electron transport and diffusion are neglected while solving the coupled continuity equations of electrons and holes. The numerical results on the EHP creation energy with wide variations of X-ray energy, electric field strengths and temperature are compared with the published experimental results and the analytical model.

5.2 Jaffe's Model

The *columnar recombination* has been explained so far by the formulation of Jaffe's model [111] in order to explain the saturation in the field dependence of the charge extraction yield in gases and liquids ionized by α and β particles. He considered the carrier continuity equations of two charged species considering carrier drift, diffusion and bimolecular recombination between non-geminate electrons and holes. He solved the equations by following an order; i.e., first neglected the drift and recombination terms, got the solution for the diffusion term only, and then reintroduced the drift term and got the solution. He then reintroduced the recombination term. This procedure essentially emphasizes the diffusion term and underestimates the recombination. The diffusion term actually has less effect than the drift and recombination terms at moderate to high electric fields. For this reason, Kramers [112] reversed the Jaffe's procedure by neglecting the diffusion term and obtained an analytical solution for the remaining equations assuming the same mobility for both the carriers (equal mobility highly simplifies the formulation!). The effective mobility of electrons and holes are far different in a-Se. Therefore, the Kramers's formulation is not appropriate for a-Se.

Jaffe assumed that the charge generated by high energy particles is initially (at time $t = 0$) in a dense column with a Gaussian distribution of initial charge carriers from the center of the cylindrical track as shown in Figure 5-1 where,

$$n_0, p_0 = \left(\frac{N_0}{\pi b_g^2} \right) e^{-(x^2+y^2)/b_g^2} \tag{5.1}$$

here N_0 is the ionization line density (charges/cm), b_g is the radius of the Gaussian distribution, and n_0 and p_0 are the initial electron and hole concentrations, respectively.
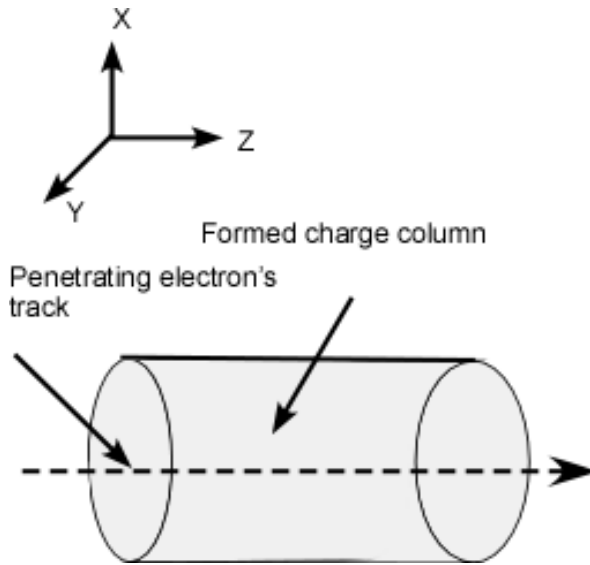
Figure 5-1 Schematic illustrating the cylindrical column formation for the columnar recombination.

The mechanism of recombination (or dissociation) of photogenerated charge carriers in amorphous selenium (a-Se) have been previously described by solving the carrier continuity equations of two charged species considering carrier drift, diffusion, and bimolecular recombination between non-geminate electrons and holes defined by the following differential equations for the time variation of the carrier concentrations,

$$\frac{\partial n}{\partial t} = \mu_e F \frac{\partial n}{\partial z} + D_e \frac{\partial^2 n}{\partial z^2} - C_r np \tag{5.2}$$

$$\frac{\partial p}{\partial t} = -\mu_h F \frac{\partial p}{\partial z} + D_h \frac{\partial^2 p}{\partial z^2} - C_r np \tag{5.3}$$

where F is the electric field, n and p are the electron and hole concentrations respectively, C_r is the recombination coefficient, and $D=\mu/k_BT$ and μ are the diffusion coefficient and mobility of the charge carriers, respectively. The subscript e and h stand for electrons and holes, respectively. Equations (5.2) and (5.3) are written for holes and electrons by replacing the positive and negative charges in the original formulation of Jaffe's model [111]. It is assumed in Equations (5.2) and (5.3) that the electric field is in the z-direction. The recombination rate in a-Se at low or nearby conventional operating field (~10 V/μm) is controlled by the diffusion of recombining carriers as described by the Langevin theory [113]. Thus, in a-Se, $C_r = C_L = e (\mu_h+\mu_e)/\varepsilon$, where C_L is the Langevin recombination coefficient, e is the elementary charge, and ε (= $\varepsilon_o\varepsilon_r$, where ε_o is the absolute and ε_r is the relative permittivity) is the permittivity of the photoconductor. The hole mobility increases by almost an order of magnitude by increasing the electric field from 10 V/μm to 80 V/μm, and saturates at the level $\mu = 0.9$ cm^2/Vs [25]. One can expect the increase of mobility would lead to the gradual deviation of the Langevin recombination mechanism and the recombination coefficient C_r at high fields attains a constant value C_0. Thus, Bubon et al. proposed an empirical expression for C_r, which is [35],

$$\frac{1}{C_r} = \frac{1}{C_L} + \frac{1}{C_0}$$

(5.4)

With a decreasing electric field, the carrier mobility decreases and the recombination coefficient gradually leads to the Langevin's value C_L.

As mentioned previously, Jaffe could not solve Equations (5.2) and (5.3) simultaneously, so he first neglected the recombination and drift terms. He then reintroduced the drift and recombination terms. Assuming that the initial charges were created in column length d and the electric field is parallel to the column axes, Jaffe derived the following analytical expression for charge extraction yield (i.e., the fraction of charges that escaped columnar recombination),

$$Y_{//}(F) = \frac{\mu F b_g^2}{2Dd} c_1 e^{-c_1} [l_i(e^{c_2}) - l_i(e^{c_1})]$$

(5.5)

where $c_1 = \dfrac{8\pi D}{C_r N_o}$ and

where $c_2 = c_1 + \ln(1 + \dfrac{2Dd}{\mu Fb_g^2})$, $\qquad$ (5.6)

here $l_i(x)$ is the logarithmic integral function, D is the diffusion coefficient ($D = D_e + D_h$), N_0 is the ionization line density, and μ is the mobility ($\mu = \mu_e + \mu_h$).

If the electric field is at an angle θ with the column axis, the fraction of electrons that escaped recombination is

$$Y_\theta(F) = \frac{1}{1 + \dfrac{C_r N_o}{8\pi D}\sqrt{\dfrac{\pi}{\zeta}} S(\zeta)} \quad , \qquad (5.7)$$

where $\quad S(\zeta) = \dfrac{1}{\sqrt{\pi}} \displaystyle\int_0^\infty \dfrac{e^{-s}ds}{\sqrt{s\left(1 + \dfrac{s}{\zeta}\right)}} \quad$, and $\zeta = \dfrac{b_g^2 \mu^2 (F\cos\theta)^2}{2D^2}$ $\qquad$ (5.8)

5.3 Analytical Model: Modeling of Columnar Recombination for High Energy Photon Generated Electron-Holes: Application to Amorphous Selenium

Jaffe's full treatment of this problem is very elegant despite the approximations he made as mentioned in section 5.2. Kramers showed that the diffusion term is negligible compared to the drift term in equations (5.2) and (5.3) if $F \gg k_B T/eb_g$, where k_B is the Boltzmann constant. That means, taking the smallest possible value for b_g to be of the order of 10 nm, F has to be much greater than 2.5 V/μm in order to justify the neglection of the diffusion term in Equations (5.2) and (5.3). In fact, the operating electric field in a-Se detectors is 10 V/μm or higher. Thus, Kramers reversed the Jaffe's procedure by neglecting the diffusion term for moderate to high electric field strengths, and obtained an analytical solution for the remaining equations. However, he assumed, the same mobility for both the carriers (equal mobility highly simplifies the formulation!). The effective mobility of electrons and holes are far different in a-Se, and thus, the original Kramers's formulation is not appropriate for the case of a-Se. In this section, a

columnar recombination model is proposed following Kramers assumptions, which are appropriate for the materials having widely unequal drift mobility for electrons and holes.

5.3.1 Electric Field Parallel to the Column Axis

Amorphous Selenium is one of the semiconductors that have been characterized by the different values of the electron and hole drift mobilities (the hole mobility is almost 40 times higher than the electron mobility) [11]. Therefore, the transport of electrons can be neglected within the time domain of the hole transport [114] and the remaining electrons after the hole transport are the escaped electrons from the columnar recombination between non-geminate electrons and holes. Thus, the transport equations for the electric field parallel to the column axis can be simplified as

$$\frac{\partial n}{\partial t} = -C_r np \tag{5.9}$$

$$\frac{\partial p}{\partial t} = -\mu_h F \frac{\partial p}{\partial z} - C_r np \tag{5.10}$$

The expression of $p(z,t)$ from Equation (5.9) can thus be written as [115]

$$p(z,t) = -\frac{1}{C_r} \frac{d}{dt} \{ \ln \frac{n(z,t)}{n_0(z)} \} \tag{5.11}$$

Substituting $p(z,t)$ in Equation (5.10) gives

$$\frac{du(z,t)}{dt} + \mu_h F \frac{du(z,t)}{dz} = -C_r n_0(z) u^2(z,t), \tag{5.12}$$

where . $u(z,t) = \frac{n(z,t)}{n_0(z)}$

The free electron concentration,

$$n_{st}(z) = n_0 [1 + \frac{C_r}{\mu_h F} \int_0^z n_0(z') dz']^{-1} . \tag{5.13}$$

The total number of electrons that escaped the columnar recombination can be expressed as

$$Q = \int_0^\infty 2\pi r \int_0^d n_{st}(z)\,dz\,dr = \frac{2\pi\mu_h F}{C_r} \int_0^\infty \ln\left(1+\frac{C_r dn_0}{\mu_h F}\right) r\,dr \tag{5.14}$$

Hence, the charge extraction yield can be written as

$$Y_{//} = \frac{Q}{N_0 d} \tag{5.15}$$

5.3.2 Electric Field Perpendicular to Column Axis

If the electric field is perpendicular to the Column axis (say along x-direction), the survived electron concentration,

$$n_{st}(x,y) = n_0[1+\frac{C_r}{\mu_h F}\int_{-\infty}^x n_0(x',y)\,dx']^{-1} \tag{5.16}$$

The total number of electrons per unit distance that escaped the columnar recombination can be expressed as,

$$N = \int_{-\infty}^\infty \int_{-\infty}^\infty n_{st}(x,y)\,dx\,dy = \frac{2\mu_h F}{C_r}\int_0^\infty \ln(1+\frac{C_r N_0}{\sqrt{\pi}\mu_h Fb_g}e^{-y^2/b_g^2})\,dy \tag{5.17}$$

Thus, the charge extraction yield can be written as

$$Y_\perp = \frac{2\mu_h F}{C_r}\int_0^\infty \ln(1+\frac{C_r N_0}{\sqrt{\pi}\mu_h Fb_g}e^{-y^2/b_g^2})\,dy \tag{5.18}$$

If the electric field is at an angle θ with the column axis, the fraction of electrons that escaped recombination can be written as,

$$Y_\theta = \frac{2\mu_h F}{C_r}\int_0^\infty \ln(1+\frac{C_r N_0}{\sqrt{\pi}\mu_h Fb_g \sin\theta}e^{-y^2/b_g^2})\,dy \tag{5.19}$$

5.3.3 EHP creation energy

The average energy needed to create a single free EHP is called the EHP creation energy W_{ehp}. The W_{ehp} is usually calculated by W_0/Y, where W_0 is the average X-ray energy needed to create an EHP and Y is the charge extraction yield. In other words, W_{ehp} is the average energy per

electron-hole pair freed, namely those EHPs which dissociate and whose carriers are collected and not the average energy per electron-hole pair created W_0. It is assumed above that the free charge carriers are not lost during their transport across the photoconduction. This assumption is true at higher temperatures (e.g., at room temperature and above) and at higher fields (e.g., at above 10 V/μm), when the charge collection efficiency for the free carriers is close to unity. However, at low temperatures and/or at lower electric field strengths for the electron mobility becomes very low and thus the charge collection efficiency even in a thin detector deviates considerably from unity. Therefore, in general, one can calculate W_{ehp} using the following expression,

$$W_{ehp} = \frac{W_0}{\eta_{cc} Y} \tag{5.20}$$

where η_{cc} is the charge collection efficiency for the free carriers, which is given by [116],

$$\eta_{cc} = \frac{\mu_h F \tau_h}{L} [1 + \frac{1}{\eta(1/\alpha_{at} \mu_h \tau_h F - 1)} (e^{-L/\mu_h \tau_h F} - e^{-\alpha_{at} L})]$$
$$+ \frac{\mu_e F \tau_e}{L} [1 - \frac{1}{\eta(1/\alpha_{at} \mu_e \tau_e F + 1)} (1 - e^{-\alpha_{at} L - L/\mu_e \tau_e F})]$$
.

$$\tag{5.21}$$

Here $\eta = 1 - \exp(-\alpha_{at} L)$ is the quantum efficiency of the detector, τ is the lifetime of the free carriers, L is the a-Se layer thickness, and α_{at} is the linear attenuation coefficient of a-Se.

5.3.4 Results and discussions

In this section, the results of the analytical model are presented to show the field and temperature dependence of the quantum yield limited by columnar recombination and compared with the published models and experimental data in order to validate the mechanisms of X-ray generated free EHP creation energy in a-Se at high electric field strengths. Figure 5-2 shows the electron-hole pair creation energy (W_{ehp}) as a function of the electric field strength at room temperature ($T = 293$ K). The open circles represent the measured electron-hole pair creation energy (W_{ehp}) for 59.5 keV Am[241] gamma rays, which were extracted from the recently published paper [35]. The dashed line represents the model calculation using Jaffe's model (Equation (5.5)) with the electric field parallel to the column axis for $N_0 = 5 \times 10^7$ cm^{-1}, $b_g = 2 \times 10^{-5}$ cm and $d =$

15×10^{-4} cm. The dash-dotted line represents the model calculation using Equation (5.7) (i.e., Jaffe's model with the electric field at an angle of 30° to the column axis) for $N_0 = 5 \times 10^7$ cm^{-1}, and $b_g = 5 \times 10^{-6}$ cm. The dotted and solid lines represent the analytical model calculations of Equations (5.15) and (5.19), respectively. The fitted parameters for both the dotted and solid lines are $N_0 = 3 \times 10^7$cm^{-1}, $b_g = 1.55 \times 10^{-6}$ cm and $d = 10^{-5}$ cm [117]. The parameter W_0 is taken as 7 eV in all calculations and η_{cc} is calculated using Equation (5.21) (Equation (17) of Ref. [116]).
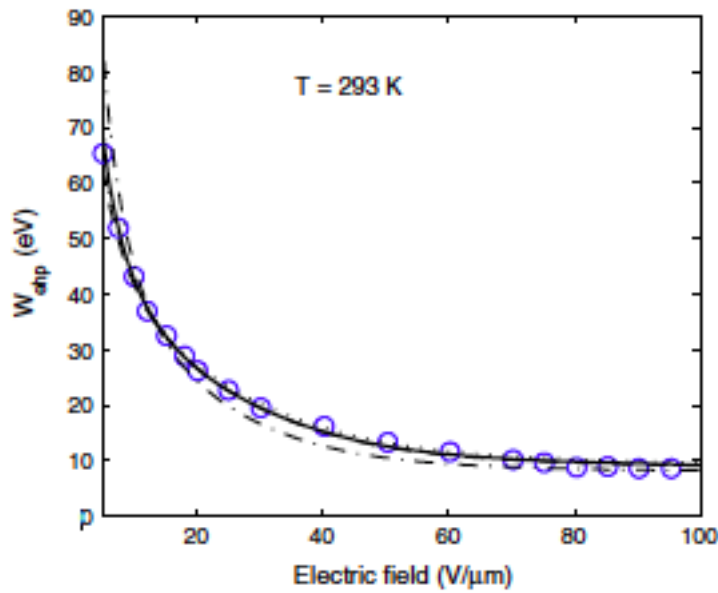
Figure 5-2 The free EHP creation energy (W_{ehp}) as a function of electric field. Symbols: experimental results [35], dashed line: Jaffe's model with electric field parallel to the column axis, dash-dotted line: Jaffe's model with electric field at an angle of 30° to the column axis, dotted line: analytical model with electric field parallel to the column axis and solid line: analytical model with electric field at an angle of 30° to the column axis [117].

The incident X-ray photons create energetic electrons and these electrons interact in discrete collisions resulting in distinct energy deposition events known as *spurs*. In the simplest version of the model, spurs are considered to be uniformly spaced and spherically shaped regions that contain few EHPs. At diagnostic X-ray energies, the linear energy transfer of the primary electrons is high enough that the spurs are overlapped and create a column along the track of the primary electron. Mah et al. [34] estimated the average spur radius to be ~ 10 nm and thus the

79

value of b_g should be of the same order of the spur radius and the value of d should be several times higher than b_g.

As shown in Figure 5-2, the solid line (i.e., the proposed model with electric field at an angle of 30° with respect to the column axis) gives the best fit to the experimental data. For $N_0 = 3 \times 10^7$ cm^{-1}, the mean separation of EHPs is ~0.3 nm (the interatomic separation in a-Se is 0.23 nm), which is reasonable. Again the fitted value of b_g is 15.5 nm, which is close to the average spur radius (10 nm) as mentioned by Mah et al. [34]. Note that Jaffe's model with electric field parallel to the column axis (dashed line in Figure 5-2) gives the next closer fit to the experimental results. However, the fitted values of b_g (200 nm) and d (15 μm) are too high, and thus, far from the reality because of unrealistic assumptions in Jaffe's formulation. Again the proposed model with electric field parallel to the column axis (dotted line in Figure 5-2) also gives a reasonable fit with the experimental results. The fitted value of d is 0.1 μm (this value is ~6 times of b_g, which is quite reasonable) and other fitted parameters are the same as in solid line curve in Figure 5-2. Therefore, the proposed model (Equations 5.14, 5.15, 5.18 & 5.19) gives the best possible explanation for the columnar recombination mechanisms in a-Se. Hence, the reasonable agreement between the theoretical calculations and the experimental data could be considered as a confirmation of the idea that the columnar recombination is the dominant mechanism of the carrier lost in the X-ray irradiated a-Se in the broad range of electric fields. This study shows that this conclusion holds even in the case of extremely high electric field strenghts above the avalanche threshold.

The temperature dependencies of W_{ehp} at various applied fields are shown in Figure 5-3. The symbols (open circles), dashed lines and solid lines represent the experimental data, the model calculation without η_{cc} and the model fit including a correction for η_{cc}, respectively. The experimental data are extracted from Ref. [35]. The model calculation considering the charge collection efficiency (solid lines in figure 5-3) shows a very good fit to the experimental results. The fitted values of carrier lifetimes in calculating the charge collection efficiency (Equation 5.21) are $\tau_e = 52$ μs and $\tau_h = 10$ μs, which are very reasonable for a-Se [11]. The temperature dependencies of drift mobility at various applied fields are adapted from Ref. [26, 118]. All other fitting parameters in Figure 5-3 are the same as in Figure 5-2. The corresponding charge

collection efficiency versus temperature at various applied field strenghts is shown in Figure 5-4. As is evident from Figure 5-4, the η_{cc} at 10 V/µm field decreases abruptly by lowering the temperature below 260 K because of the very low mobility of electrons at low temperatures [26]. At 59.5 keV γ-ray excitation on a 15 µm thin detector, the normalized absorption depth (the absorption depth/thickness) becomes 64 and thus the charge collection of holes and electrons are almost equally important [95]. The electron collection at low temperatures is severely affected by its low mobility, which reduces the overall charge collection efficiency. However, the electron mobility increases abruptly with increasing the applied field strengths beyond 20 V/µm and the charge collection efficacy has a less significant effect on W_{ehp} at higher fields.
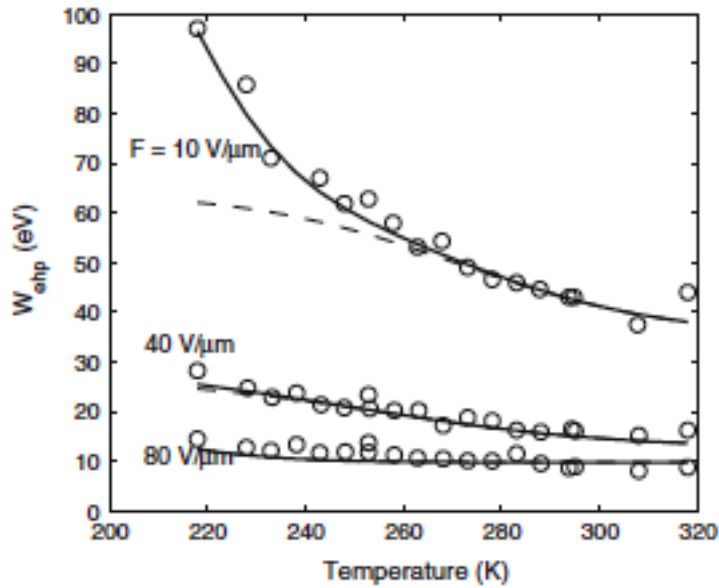
Figure 5-3 W_{ehp} versus temperature at various electric fields. Symbols: experimental results [35], dashed line: W_{ehp} calculation without considering free charge collection efficiency and solid line: the model fit including a correction for free charge collection efficiency (η_{cc}) [117].
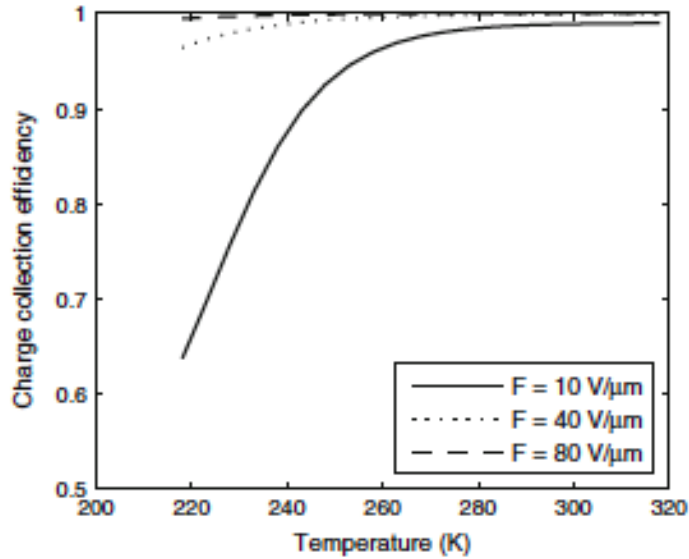
Figure 5-4 Charge collection efficiency of free carriers versus temperature at various electric fields [117].

5.3.5 Conclusions

The theoretical model for describing the columnar recombination at moderate to high electric field strenghts in the materials that have widely unequal drift mobility for electrons and holes has been described. The EHP creation energy has been calculated by incorporating the initial charge extraction yield and the charge collection efficacy of the free carriers. The results of the model have been compared with the recently published experimental results on temperature and field dependent EHP creation energy. The analytical model with electric field at an angle of 30° to the column axis gives the best fit to the experimental data with reasonable fitting parameters. Although Jaffe's model with electric field parallel to the column axis gives the second best fit to the experimental results, the fitted values of b_g and d are too high and unreasonable because of unrealistic assumptions in Jaffe's formulation (i.e., emphasizes diffusion rather than drift even at high fields). The charge collection efficacy for free carriers has a significant effect on determining the EHP creation energy when the carrier mobility is too low (e.g. at low temperature and/or at low field in a-Se). The results of this work, combined with data in [35], have shown that the analytical model gives a possible alternative explanation to the

columnar recombination mechanisms in a-Se. The free EHP creation mechanisms at high-energy photon excitation in a-Se can be described by the columnar recombination.

5.4 Numerical model: Electron-hole pair creation energy in amorphous selenium for high photon excitation.

In the previous section (5.3), an analytical model was developed to show the electric field and temperature dependence of the charge extraction yield limited by the columnar recombination in a-Se having widely unequal drift mobility for electrons and holes [117]. The calculation of the free electron hole pair creation energy was performed by solving the carrier continuity equations of two charged species considering only hole drift and bimolecular recombination between non-geminate electrons and holes. Results have shown that although both the proposed analytical and Jaffe's models can fit the experimental results, the fitted parameters using the proposed model are more reasonable than that using the Jaffe's model. However, the fitting parameters might not be fully accurate because the electron transport and diffusion have been neglected in the analytical model while solving the coupled continuity equations of electrons and holes.

In this section, the three-dimensional continuity equations for both electrons and holes, are numerically solved to show the electric field, X-ray energy and temperature dependencies of the charge extraction yield limited by the columnar recombination considering carrier drift, diffusion and bimolecular recombination between non-geminate electrons and holes. The numerical results are compared with the published experimental results for 59.5 keV Am^{241} γ-rays [35] and the analytical model. Also, the numerical model is applied to the published experimental results on EHP creation energy with wide variations of X-ray energy, electric field and temperature. A comprehensive understanding on EHP creation energy in a-Se for X-ray and γ-ray excitations is thus proposed.

5.4.1 Numerical Model

In this section, using COMSOL Multiphysics 5.2a, the following three dimensional coupled continuity equations of electrons and holes within a cylindrical domain (Figure 5-5) as originally proposed by Jaffe are numerically solved [111] (the model description and simulation setup are given in Appendix B).

$$\frac{\partial p}{\partial t} = -\mu_h F \nabla p + D_h \nabla^2 p - C_r np$$

$$\frac{\partial n}{\partial t} = \mu_e F \nabla n + D_e \nabla^2 n - C_r np$$

(5.22)

where $\nabla(x,y,z)$ is the del operator, μ is the drift mobility , F is the electric field, C_r is the recombination coefficient and D is the diffusion coefficient and, n and p are the concentrations of electrons and holes, respectively. The subscript e and h stand for electrons and holes, respectively.

Similarly, Jaffe assumed that the EHPs are created in a dense column with a Gaussian distribution of initial charge carriers from the center of the cylindrical track by high energy particles, as shown in Figure 5-5. So, the initial condition (at time $t = 0$) of the continuity equations is defined by equation (5.1)
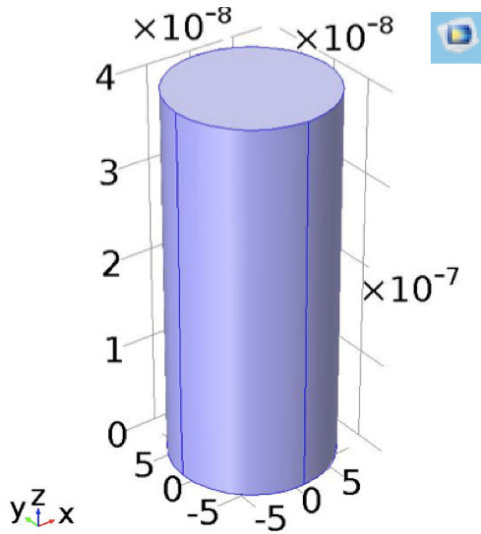
Figure 5-5 Built-in three-dimensional cylinder using COMSOL multiphysics 5.2a (units are in SI standard).

Assuming that the initial charges are created in a column length d and the applied electric field is along the z-axis (i.e., parallel to the column axis), carriers start to drift along the column length. That means, at $t > 0$, the free electron concentration at $z = d$ and the free hole concentration at $z = 0$ are zero. On the other hand, if the applied electric field is perpendicular to the column axis, say along y axis, carriers start to drift perpendicular to the column axis and the free electron concentration at $y = \infty$ and the free hole concentration at $y = -\infty$ are zero. Therefore, the considered boundary conditions are:

$n\ (z = d) = 0$

$p\ (z = 0) = 0$

$$(5.23)$$

Once the electron and hole profiles are practically separated (usually after few transit times of holes in a-Se), the remaining electrons or holes are the escaped carriers from the columnar recombination. The total number of electrons or holes that escaped the columnar recombination can be determined by integrating the remaining hole or electron concentration over the cylindrical volume V,

$$Q = \int_V n(x, y, z) dV$$

$$(5.24)$$

Hence, the charge extraction yield and the electron hole pair creation energy can be found from equations (5.15) and (5.20).

5.4.2 Results and discussions

In this section, the simulation results of the numerical model are presented, analyzed and compared with the analytical model [117] and experimental results on EHP creation energy with widely varying the electric field, X-ray energy and temperature. The parameters, $W_0 = 7$ eV, $d = 10^{-5}$ cm and $C_0 = 4 \times 10^{-8}$ cm^3/s are fixed in all calculations [35, 117].

Figure 5-6 shows the electron-hole pair creation energy (W_{ehp}) as a function of the electric field at room temperature ($T = 293$ K). The open circles represent the measured electron-hole pair creation energy (W_{ehp}) for 59.5 keV Am^{241} gamma rays, which were extracted from a recently published paper [35]. The solid and dashed lines represent the present numerical model fit to the experimental data with the electric field perpendicular and parallel to the column axis, respectively. The common fitted value of b_g is 1.7×10^{-6} cm for both solid and dashed lines. The fitted value of ionization line density, $N_0 = 8 \times 10^7$ and 5×10^7 cm^{-1} for the electric field perpendicular and parallel to the column axis, respectively. One can expect the fitted value of N_0 in between these two values for the applied field making any other angle with the column axis. Both the solid and dashed lines fit the experimental results quite well with a little difference in N_0. Therefore, for simplicity, the electric field parallel to the column axis is considered in the rest of the analysis. The dash-dotted and dotted lines represent results of the analytical model having the same fitting parameters with the electric field parallel and perpendicular to the column axis, respectively [117]. The analytical model slightly over estimates W_{ehp}, especially at low field strengths because of neglecting carrier diffusion. The carrier diffusion process enhances the escaping probability, improves the charge extraction yield, and reduces the EHP creation energy.
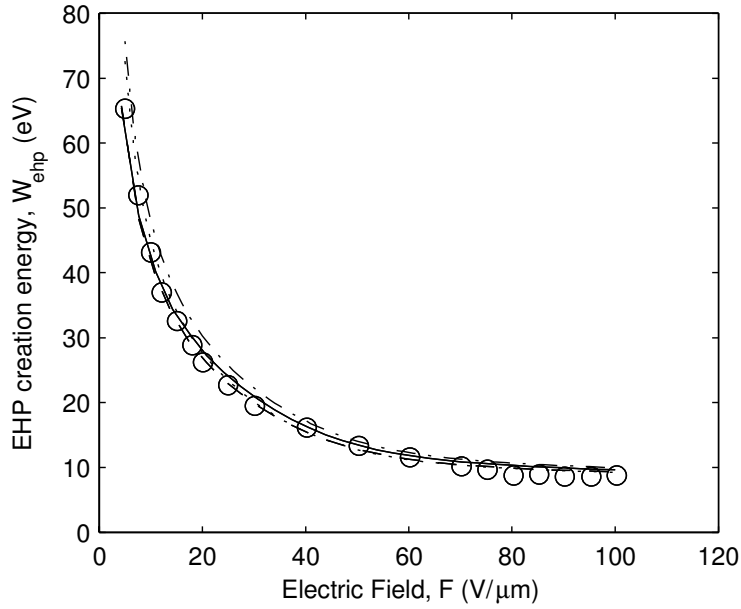
Figure 5-6 The EHP creation energy (W_{ehp}) as a function of the electric field strengths. Symbols: experimental results for 59.5 keV Am[241] gamma rays [35]. The solid and dashed lines: numerical model fit to the experimental results with electric field parallel and perpendicular to the column axis, respectively. The dash-dotted and dotted lines: analytical model with electric field parallel and perpendicular to the column axis, respectively [117].

The temperature dependencies of W_{ehp} at various applied electric field strengths are shown in figure 5-7. The symboles (open circles), dashed lines and solid lines represent the experimental data, the present numerical results results without η_{cc} and the numerical results including η_{cc}, respectively where η_{cc} is calculated using Equation (5.21) (Equation (17) of Ref. [116]). The applied field parallel to the column axis is considered. The experimental data were extracted from Ref. [35]. All of the fitting parameters in Figure 5-7 are the same as those used in Figure 5-6. The temperature dependencies of the drift mobility at various applied field strengths are adapted from Refs. [26, 118]. The drift mobility of both the holes and the electrons increase with increasing temperature. The increase of mobility with temperature improves the charge extraction yield and thus reduces the EHP creation energy (the dashed line in Figure 5-8).

At low temperatures, $T < 260$ K, at an electric field strength of 10 V/μm, the charge collection efficiency deviates from unity considerably [117], since the electron mobility becomes very low [26, 118]. However, increasing the temperature beyond 260 K and/or the applied electric field strength beyond 20 V/μm, the charge collection efficiency has a negligible effect on

87

the measurement of W_{ehp}. The results of the simulation show a very good fit to the experimental results. The fitted values of the mobility-lifetime products in equation (5.21) at $F = 10$ V/µm as a function of temperature are shown in Figure 5-8. The mobility-lifetime products increase with increasing temperature, which is consistent with previous observation [16].
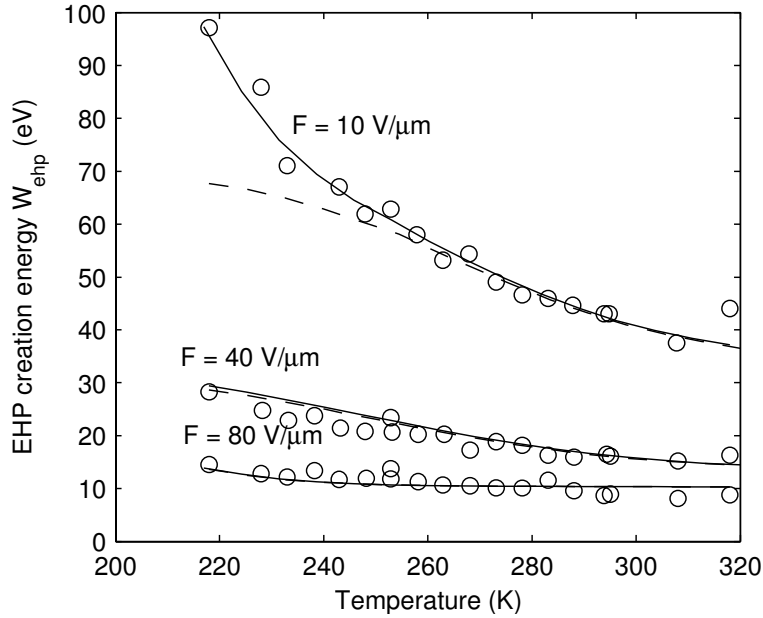
Figure 5-7 W_{ehp} versus temperature at various electric fields. Symbols: experimental results [35], dashed lines and solid lines: numerical model fit to the experimental data without η_{cc} and with η_{cc} respectively.
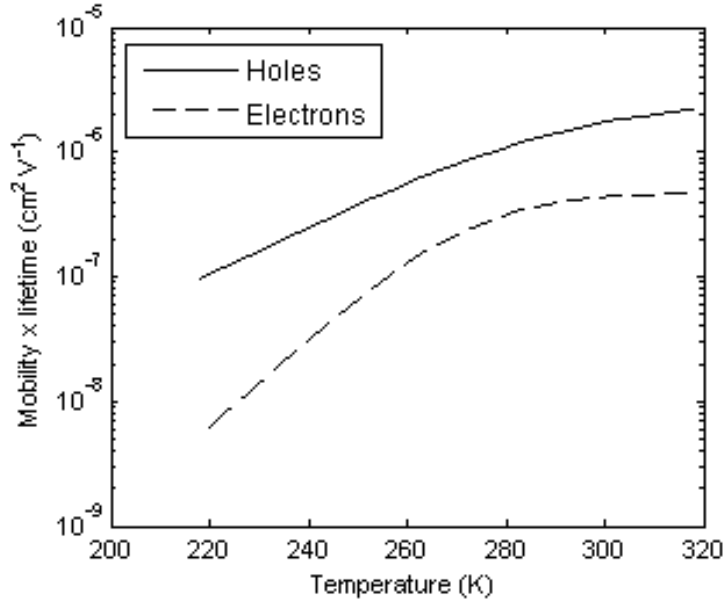
Figure 5-8 The fitted values of mobility-lifetime products of holes and electrons in equation (5.21) at $F = 10$ V/µm as a function of temperature.

Figure 5-9 shows the electron-hole pair creation energy (W_{ehp}) as a function of the electric field at room temperature ($T = 293$ K) for various X-ray energies (16.5 KeV to 1.25 MeV). The symbols represent the measured electron-hole pair creation energy for various X-ray energies, which are extracted from Refs. [34, 67, 119]. The solid lines represent the numerical model fit to the experimental data for the applied fields parallel to the column axis. The fitted values of N_0 and b_g are given in Table 5-1. The numerical results agree well with the experimental data. The W_{ehp} in a-Se has a strong dependence on the electric field, but only a weak dependence on the X-ray photon energy. The EHP creation energy decreases slowly with increasing photon energy in the diagnostic and Megavolt range. The fitted value of N_0 decreases with increasing photon energy, and hence, the average distance between the created EHPs increases. As a result, electrons and holes have a greater probability of escape, which reduces the EHP creation energy. That means, the rate of deposition of energy per unit distance travelled by a primary electron decreases with its energy and so does with the excited photon energy in the X-ray or γ-ray regimes. The explanation is consistent with the Monte Carlo simulation results of Fourkal et al. [36]. The results of this work show that the *columnar recombination model* can describe the electric field, temperature, and photon energy dependent EHP creation energy in a-Se.
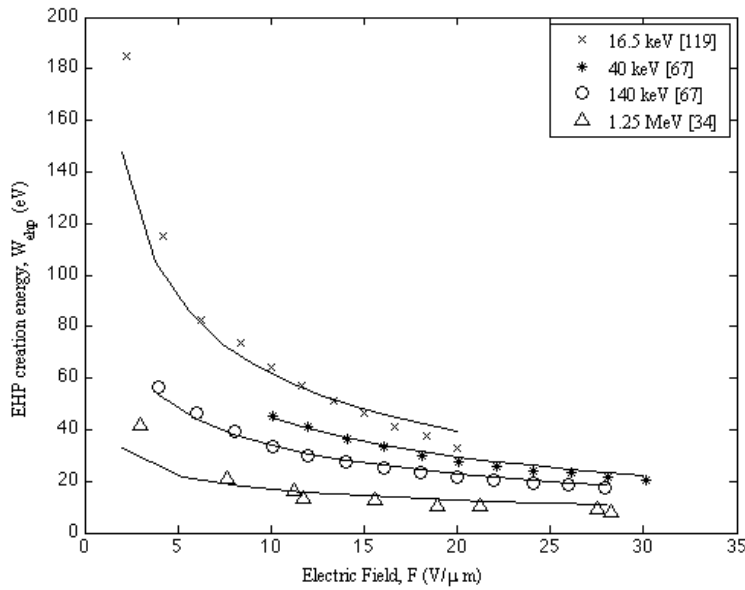
Figure 5-9 Electron-hole pair creation energy as a function of electric field at various photon energies. Symbols: experimental data [34, 67, 119], solid lines: numerical model fit to the experimental data.

Table 5-1 Fitted parameters of Figure 5-9

Photon energy, E (keV)	N_0 (cm^{-1})	b_g (cm)
16.5 keV	8.5×10^7	1.6×10^{-6}
40 keV	5.5×10^7	1.7×10^{-6}
140 keV	3.4×10^7	1.73×10^{-6}
1.25 MeV	1.0×10^7	1.86×10^{-6}

5.4.3 Conclusions

A numerical model has been developed to describe the columnar recombination mechanism in a-Se by solving the three-dimensional coupled continuity equations for electrons and holes, considering carrier drift, diffusion and bimolecular recombination between non-geminate electrons and holes. The numerical simulation results are compared with the published experimental results and the analytical model [117]. Though the analytical model slightly overestimates the EHP creation energy, it is reasonably accurate. The columnar recombination

model has also been applied to the published experimental results on EHP creation energy with widely varying X-ray energy, electric field and temperature. The model shows a good agreement with the experimental results, which indicates that the *columnar recombination model* is capable of describing the electric field, temperature, and photon energy dependent EHP creation energy in a-Se for high energy photons.

Chapter

6. Concluding remarks and future work

The objective of this work was to investigate the fundamental underlying physics of carrier generation, multiplication, and transport mechanisms in amorphous selenium as they pertain to its use as an X-ray photoconductor. The summary of this work and recommendations for future study are presented in this section.

6.1   Summary and Conclusions

There has been a substantial renewed interest in the electrical and optical properties of amorphous selenium since alloys of a-Se are an attractive X-ray photoconductor for medical imaging applications because large-area, uniform layers may be economically fabricated using conventional vacuum deposition techniques without damaging the AMA electronics. Amorphous selenium has confirmed its use as an X-ray photoconductor in newly developed X-ray image detectors and as an avalanche photoconductor in ultrahigh sensitivity video tubes known as HARPICONs.

In Chapter 3, an analytical model has been developed to study the possible physical mechanisms of the electric field strength and temperature dependent effective drift mobility of holes and electrons and impact ionization at extremely high electric fields in a-Se considering density of states distribution near the band edges, field enhancement release rate from the shallow traps, and carrier heating. The models for the effective drift mobility of holes have been evaluated considering both the Frenkel-Poole and thermally assisted tunneling release mechanisms from shallow trap levels combined with the microscopic mobility model. The lucky-drift model for a-Se has been developed based on the observed field dependent microscopic mobility. These developed models have been compared to experimental observations. It has been found that while the effective drift mobility increases with increasing temperature and field strength, the microscopic mobility and momentum relaxation mean free path in a-Se decreases with increasing electric field. This has helped in describing the electric field and temperature

dependent behaviours of impact ionization coefficient in a-Se. It has been shown also that the shallow hole traps in a-Se are neutral defects by considering thermally activated tunneling for the field-enhancement release rate. Also, the results revealed that the effective drift mobility at extremely high field strength is mainly controlled by the neutral defect states near the band edges when considering thermally activated tunneling for the field-enhancement release rate. The momentum relaxation mean free path in a-Se decreases with increasing electric field and decreasing temperature, which has remarkable effects on the field and temperature-dependent impact ionization coefficient in a-Se. The density of state function near the band edges, consisting of an exponential tail and a Gaussian peak, successfully described the electric field and temperature-dependent effective drift mobility characteristics in a-Se.

In Chapter 4, the physical mechanisms for wavelength and electric field dependent charge carrier photogeneration (optical excitation) in a-Se under high electric field strengths have been investigated. It has been proved in this work that the exact extension of the Onsager Theory (Noolandi-Hong model) of the photogeneration efficiency justifies the electric field, excitation wavelength dependent photogeneration efficiency in amorphous selenium. Furthermore, a formulation for calculating the excitation wavelength and electric field-dependent initial separation of the photogenerated and thermalized geminate electron and hole has been proposed, and applied to explain the field-dependent photogeneration efficiency in a-Se. Both the Noolandi-Hong model and the conventional Onsager model with field-dependent initial separation r_0 are able to explain excitation wavelength and field-dependent photogeneration efficiency in a-Se, though the Noolandi-Hong model shows a better and logical fitting with the experimental results.

In Chapter 5, an analytical model has been developed to show the electric field strength and temperature dependence of the charge extraction yield limited by the columnar recombination for a-Se for X-ray excitation. The model has been compared with previous columnar recombination models with widely varying field and temperature. In addition, the free electron-hole pair (EHP) creation energy has been calculated by incorporating the initial charge extraction yield and the charge collection efficacy of the free carriers. The results of the model have been compared with the recently published experimental results on temperature and field

dependent EHP creation energy. The proposed model with electric field at an angle of 30° to the column axis gives the best fit to the experimental data with reasonable fitting parameters. Although Jaffe's model with electric field parallel to the column axis gives the second best fit to the experimental results, the fitted values of b_g and d are too high and unreasonable because of unrealistic assumptions in Jaffe's formulation (i.e., emphasizes diffusion rather than drift even at high fields). The charge collection efficacy for free carriers has a significant effect on determining the EHP creation energy when the carrier mobility is too low (e.g. at low temperature and/or at low field in a-Se).

Moreover, a numerical model has been developed to describe the electron-hole pair creation energy in amorphous selenium by solving the three dimensional coupled continuity equations of electrons and holes, considering carrier drift, diffusion and bimolecular recombination between non-geminate electrons and holes. The numerical model is fit with the published experimental results on wide variations of X-ray energy, electric field and temperature, and the model showed a good agreement. The analyses of the results confirm that the proposed model gives the best possible explanations to the columnar recombination mechanisms in a-Se and the free EHP creation mechanisms at diagnostic X-ray exposures can be described by the columnar recombination.

In Summary, avalanche a-Se detector can be used for both direct and indirect conversion X-ray detectors. For a direct conversion, a multilayer structure that consists of an absorption layer followed by avalanche a-Se layer is needed [120]. Whereas, for indirect conversion, the avalanche a-Se layer can simply replace the photodiode in conventional indirect conversion X-ray detectors [121].

6.2 Future work

Although stabilized a-Se promises to be an excellent X-ray photoconductor for flat-panel X-ray image detectors, there are still a number of unresolved theoretical and practical issues. As noted above, there is very limited data on the temperature and energy dependence of the EHP creation energy W_{ehp} given that this quantity directly determines the overall efficiency of the

detector. Hence, additional measurements will help given the best fit to analytical measurements and will answer the scientific curiosity of what limits W_{ehp} and would allow a better device design.

Amorphous selenium at high electric field strengths exhibits avalanche multiplication that has been commercially implemented in super-sensitive TV pick-up tubes for optical excitation by Tanioka and Co-workers [76]. They have built high-gain avalanche rushing photoconductors (HARP) that have a much higher sensitivity than conventional TV pick up tubes. If such avalanche gains could be utilized in X-ray detectors for medical imaging, the patient X-ray dose can be highly reduced. Although a-Se shows carrier multiplication, any protype avalanche a-Se detector with experimental evaluation of improved image quality has yet to be made. This needs proper design of detectors [120, 121] and a systematic experimental evaluation of final image quality.

Few other photoconductors such as PbO and organic perovskites show better X-ray sensitivity than a-Se. Recent experiments show that amorphous PbO exhibits similar charge carrier transport and photogenation behavior to a-Se [122, 123]. The transport properties of amorphous selenium are similar to organic semiconductors [124]. The theoretical work in this thesis on charge carrier transport and photogenation in a-Se can also be applied to PbO and organic perovskites.

References

[1]   S. R. Ovshinski, "Amorphous semiconductors for microelectronics", *Proceedings of SPIE,* vol. 617, pp. 1-9, 1986.

[2]   N. F. Guler and E. D. Ubeyli, "Theory and applications of telemedicine", *Journal of Medical Systems,* vol. 26, pp. 199-220, 2002.

[3]   M. J. Yaffe and J. A. Rowlands, "X-ray detectors for digital radiology", *Physics in Medicine and Biology,* vol. 42, pp. 1-39, 1997.

[4]   J. A. Rowlands and J. Yorkston, "Flat panel detectors for digital radiography", in *Handbook of Medical Imaging,* vol. 1, edited by J. Beutel, H. L. Kundel, and R. L. V. Metter, SPIE Press, Washington, 2000.

[5]   V. N. r. Cooper, T. Oshiro, C. H. Cagnon, L. W. Bassett, T. M. McLeod-Stockmann, and N. V. Bezrukiy, "Evaluation of detector dynamic range in the x-ray exposure domain in mammography: a comparison between film-screen and flat panel detector systems", *Medical Physics,* vol. 30, pp. 2614-2621, 2003.

[6]   D. C. Hunt, O. Tousignant, and J. A. Rowlands, "Evaluation of the imaging properties of an amorphous selenium-based flat panel detector for digital fluoroscopy", *Medical Physics,* vol. 31, pp. 1166-75, 2004.

[7]   S. O. Kasap and J. A. Rowlands, "Direct-conversion flat panel X-ray image detectors", *IEE Proceedings - Circuits, Devices and Systems,* vol. 149, pp. 85-96, 2002.

[8]   A. R. Cowen, S. M. Kengyelics, and A. G. Davies, "Solid-state, flat-panel, digital radiography detectors and their physical imaging characteristics", *Clinical Radiology,* vol. 63, pp. 487-98, 2008.

[9]   J. M. Boone, "X-ray production, interaction, and detecting in diagnostic imaging", in *Handbook of Medical Imaging*, vol. 1, edited by J. Beutel, H. L. Kundel, and R. L. V. Metter, SPIE Press, Washington, 2000.

[10]   J. A. Rowlands and S. O. Kasap, "Amorphous Semiconductor Usher in Digital X-ray Imaging", *Physics Today,* vol. 50, pp. 24-30, 1997.

[11]   S. O. Kasap and J. A. Rowlands, "Review: X-ray photoconductors and stabilized a- Se for direct conversion digital flat-panel X-ray image detectors", *Journal of Materials Science: Materials in Electronics,* vol. 11, pp. 179-198, 2000.

[12]   S. O. Kasap, J. B. Frey, G. Belev, O. Tousignant, H. Mani, J. Greenspan*, et al.*, "Amorphous and Polycrystalline Photoconductors for Direct Conversion Flat Panel X-Ray Image Sensors", *Sensors,* vol. 11, pp. 5112-5157, 2011.

[13]   K. Jandieri, O. Rubel, S. D. Baranovskii, A. Reznik, J. A. Rowlands, and S. O. Kasap, "Lucky-drift model for impact ionization in amorphous semiconductors", *Journal of Materials Science: Materials in Electronics,* vol. 20, pp. 221-226, 2009.

[14]   A. Reznik, S. D. Baranovskii, O. Rubel, G. Juska, S. O. Kasap, Y. Ohkawa*, et al.*, "Avalanche multiplication phenomenon in amorphous semiconductors: a-Se vs a-Si: H.", *Journal of applied physics,* vol. 102, p. 053711, 2007.

[15]   K. Kikuchi, Y. Ohkawa, K. Miyakawa, T. Matsubara, K. Tanioka, M. Kubota*, et al.*, "Hole-Blocking mechanism in high-gain avalanche rushing amorphous photoconductor (HARP) film", *physica Status Solidi C,* vol. 8, pp. 2800-2803, 2011.

[16]   B. Fogal and S. O. Kasap, "Temperature dependence of charge carrier ranges in stabilized a-Se photoconductors", *Canadian Journal of Physics,* vol. 92, pp. 634-640, 2014.

[17]   S. A. Mahmood and M. Z. Kabir, "Dark current mechanisms in stabilized amorphous selenium based n-i detectors for x-ray imaging applications", *Journal of Vacuum Science & Technology A: Vacuum, Surfaces, and Films,* vol. 29, p. 031603, 2011.

[18]   S. Abbaszadeh, A. Tari, W. S. Wong, and K. S. Karim, "Enhanced Dark Current suppression of Amorphous selenium detector with use of IGZO hole blocking layer", *IEEE Transactions on Electron Devices,* vol. 61, p. 3355, 2014.

[19]   G. Juska, K. Arlauskas, J. Kocka, M. Hoheisel, and P. Chabloz, "Hot Electrons in Amorphous Silicon", *Physical Review Letters,* vol. 75, p. 2984, 1995.

[20]   J. B. Chevrier and B. Equer, "High electric-field amorphous silicon p-i-n diodes: effect of the p-layer thickness", *Journal of applied physics,* vol. 76, pp. 7415-7422, 1994.

[21]   W. Futako, T. Sugawara, T. Kamiya, and I. Shimizu, "High electric-field photocurrent of Vidicon and diode devices using wide band gap a-Si:H prepared with intentional control of silicon network by chemical annealing", *Journal of Organometallic Chemistry,* vol. 611, pp. 525-530, 2000.

[22]   M. Kubota, T. Kato, S. Suzuki, H. Maruyama, K. Shidara, K. Tanioka*, et al.*, "Ultrahigh-sensitivity new super-HARP camera", *IEEE Transactions on Broadcasting,* vol. 42, pp. 251-258, 1996.

[23]   M. M. Wronski, W. Zhao, A. Reznik, K. Tanioka, G. DeCrescenzo, and J. A. Rowlands, "A solid-state amorphous selenium avalanche technology for large area photon counting and photon starved imaging applications," *Medical Physics,* vol. 37, pp. 4982-4986, 2010.

[24]   M. Z. Kabir and S. O. Kasap, "Sensitivity of X-ray photoconductors: Charge trapping and absorption-limited universal sensitivity curves", *Journal of Vacuum Science & Technology A: Vacuum, Surfaces, and Films,* vol. 20, pp. 1082-1086, 2002.

[25]   O. Bubon, G. DeCrescenzo, J. A. Rowlands, and A. Reznik, "Amorphous Selenium (a-Se) Avalanche photosensor with metal electrodes", *Journal of Non-Crystalline Solids,* vol. 358, p. 2431, 2012.

[26]   G. Juska and K. Arlauskas, "Impact ionization and mobilities of charge carriers at high electric fields in amorphous selenium", *Physica Status Solidi A,* vol. 59, p. 389, 1980.

[27]   S. O. Kasap and C. Juhasz, "Time-of-flight drift mobility measurements on chlorine-doped amorphous selenium films", *Journal of Physics D: Applied Physics,* vol. 33, pp. 703-720, 1985.

[28]   N. Kramer and C. V. Berkel, "Reverse current mechanisms in amorphous silicon diodes", *Applied Physics Letters,* vol. 64, p. 1129, 1994.

[29]   O. Rubel, A. Potvin, and D. Laughton, "Generalized lucky-drift model for impact ionization in semiconductors with disorder", *Journal of Physics: Condensed Matter,* vol. 23, p. 055802, 2011.

[30]   S. McKenzie and M. G. Burt, "A test of the lucky-drift theory of the impact ionisation coefficient using Monte Carlo simulation", *Journal of Physics C: Solid State Physics,* vol. 19, pp. 1959-1973, 1986.

[31]   D. M. Pai and R. C. Enck, "Onsager mechanism of photogeneration in amorphous selenium", *Physical Review B,* vol. 11, pp. 5163-5174, 1975.

[32]   A. Reznik, K. Jandieri, F. Gebhard, and S. D. Baranovskii, "Non-Onsager mechanism of long-wave photogeneration in amorphous selenium at high electric fields", *Applied Physics Letters,* vol. 100, p. 132101, 2012.

[33]   J. C. Knights and E. A. Davis, "Photogeneration of charge carriers in amorphous selenium", *Journal of Physics and Chemistry of Solids,* vol. 35, pp. 543-544, 1974.

[34]   D. Mah, J. A. Rowlands, and J. A. Rawlinson, "Sensitivity of amorphous selenium to x-rays from 40 kVp to 18 MV: Measurements and implications for portal imaging", *Medical Physics,* vol. 25, pp. 444-456, 1998.

[35]   O. Bubon, K. Jandieri, S. D. Baranovskii, S. O. Kasap, and A. Reznik, "Columnar recombination for x-ray generated electron-holes in amorphous selenium and its significance in a-Se x-ray detectors", *Journal of applied physics,* vol. 119, p. 124511, 2016.

[36]   E. Fourkal, M. Lachaine, and B. G. Fallone, "Signal formation in amorphous-Se-based x-ray detectors", *Physical Review B,* vol. 63, p. 195204, 2001.

[37]   R. A. Street, Hydrogenated amorphous silicon: Cambridge University Press, London 1991.

[38]   A. Madan and M. P. Shaw, The Physics and Applications of Amorphous Semiconductors, Academic Press Inc., San Diego, 1988.

[39]   N. F. Mott, "Electrons in Disordered Structures", *Advances in Physics,* vol. 16, pp. 49-57, 1967.

[40]   P. W. Anderson, "Absence of Diffusion in Certain Random Lattices", *Physical Review,* vol. 109, pp. 1492-1505, 1958.

[41]   M. H. Cohen, H. Fritzsche, and S. R. Ovshinski, "Simple Band Model for Amorphous Semiconductor Alloys", *Physical Review Letters,* vol. 22, pp. 1065-1072, 1969.

[42]   J. M. Marshall and A. E. Owen, "Drift mobility studies in vitreous arsenic triselenide", *Philosophical Magazine,* vol. 24, pp. 1281-1290, 1971.

[43] M. Abkowitz, "Density of states in a-Se from combined analysis of xerographic potentials and transient transport data", *Philosophical Magazine Letters,* vol. 58, pp. 53-57, 1988.

[44] H. Z. Song, G. J. Adriaenssens, E. V. Emelianova, and V. I. Arkhipov, "Distribution of Gap States in Amorphous Selenium Thin Films", *Physical Review B,* vol. 59, pp. 10607-10613, 1999.

[45] L. Benkhedir, M. S. Aida, and G. J. Adriaenssens, "Defect Levels in the Band Gap of Amorphous Selenium", *Journal of non-crystalline solids,* vol. 344, pp. 193-198, 2004.

[46] L. Benkhedir, M. Brinza, and G. J. Adriaenssens, "Electronic Density of States in Amorphous Selenium", *Journal of Physics: Condensed Matter,* vol. 16, pp. S5253-S5264, 2004.

[47] N. Qamhieh, M. K. Benkhedir, M. Brinza, J. Willeken, and G. J. Adriaenssens, "Steady State Photoconductivity in Amorphous Selenium Glasses", *Journal of Physics: Condensed Matter,* vol. 16, pp. 3827-3833, 2004.

[48] K. Koughia, Z. Shakoor, S. O. Kasap, and J. M. Marshall, "Density of Localized Electronic Sates in a-Se from Electron Time-of-Flight Photocurrent Measurements", *Journal of Applied Physics,* vol. 97, pp. 033706-0337011, 2005.

[49] G. Lucovsky, Physics of selenium and tellurium, Springer-Verlag, New York, 1979.

[50] F. Gompf, "The phonon densities of states of trigonal, vitreous and red amorphous selenium", *Journal of Physics and Chemistry of Solids,* vol. 42, pp. 539-544, 1981.

[51] A. Rose, Electron Phonon Interaction, World Scientific, 1989.

[52] R. A. Zingaro and W. C. Cooper, Selenium, Van Nostrand Reinhold, 1974.

[53]   M. Kastner, D. Adler, and H. Fritzche, "Valence-alternation model for localized gap states in lone-pair semiconductors", *Physical Review Letters,* vol. 37, pp. 1504-1507, 1976.

[54]   D. Adler, "Amorphous semiconductors," *Scientific American,* vol. 236, pp. 36-48, 1977.

[55]   M. Kastner, *Amorphous and liquid semiconductors*, Seventh International Conference on Amorphous and Liquid Semiconductors, edited by W. E. Spear, University of Edinburgh, p. 504, 1977.

[56]   J. M. Marshall, "Carrier diffusion in amorphous semiconductors", *Report on Progress in Physics,* vol. 46, pp. 1235-1282, 1983.

[57]   W. E. Spear, "Electronic Transport and localization in low Mobility Solids and Liquids", *Advances in Physics,* vol. 23, pp. 523-543, 1974.

[58]   N. F. Mott and E. A. Davis, Electronic Processes in Non-Crystalline Materials, Clarendon Press, Oxford, 1971.

[59]   W. E. Spear, "Transit time measurements of charge carriers in amorphous selenium films", *Proceedings from the Physical Society of London,* vol. B70, pp. 669-675, 1957.

[60]   A. I. Rudenko and V. I. Arkhipov, "Drift and diffusion in materials with traps. I. Quasi equilibrium transport regime", *Philosophical Magazine B,* vol. 45, pp. 177-187, 1982.

[61]   M. Abkowitz, "Evidence of the defect origin of states which control photoelectric behavior of amorphous chalcogenides", *Journal of Non-Crystalline Solids,* vol. 66, pp. 315-320, 1984.

[62] M. Abkowitz and J. Markovics, "Evidence of equilibrium native defect populations in amorphous chalcogenides from analysis of xerographic spectra", *philosophical Magazine B,* vol. 49, pp. L31-L36, 1984.

[63] S. O. Kasap, K. V. Koughia, B. Fogal, G. Belev, and R. E. Johanson, "The influence deposition conditions and alloying on the electronic properties of amorphous selenium", *Semiconductors,* vol. 14, pp. pp.816-821, 2003.

[64] C. A. Klein, "Bandgap dependence and related features of radiation ionization energies in semiconductors", *Journal of applied physics,* vol. 39, pp. 2029-2038, 1968.

[65] G. F. Knoll, Radiation Detection and Measurement, John Wiley and Sons, New York, 2000.

[66] W. Que and J. A. Rowlands, "X-ray photogeneration in amorphous selenium: Geminate versus columnar recombination", *Physical Review B,* vol. 51, pp. 10500-10507, 1995.

[67] I. M. Blevis, D. C. Hunt, and J. A. Rowlands, "Measurement of x-ray photogeneration in amorphous selenium", *Journal of applied physics,* vol. 85, p. 7958, 1999.

[68] C. Haugen, S. O. Kasap, and J. A. Rowlands, "Charge transport and electron-hole pair creation energy in stabilized a-Se x-ray photoconductors", *Journal of Physics D: Applied Physics,* vol. 32, p. 200, 1999.

[69] N. Hijazi and M. Z. Kabir, "Mechanisms of charge photogeneration in amorphous selenium under high electric fields," *Journal of Materials Science: Materials in Electronics,* vol. 27, p. 7534, 2016.

[70] H. Naito, T. Iwai, M. Okuda, T. Matsuhita, and A. Sugimura, "Computer simulation study of tail-state distribution in amorphous selenium", *Journal of Non-Crystalline Solids,* vol. 114, p. 112, 1989.

[71]   P. A. Martin, B. G. Streetman, and K. Hess, "Electric field enhanced emission from non-coulombic traps in semiconductors", *Journal of applied physics,* vol. 52, p. 7409, 1981.

[72]   G. Vincent, A. Chantre, and D. Bois, "Electric field effect on the thermal emission of traps in semiconductors", *Journal of applied physics,* vol. 50, p. 5484, 1979.

[73]   V. F. Kozhevnikov, W. B. Payne, J. K. Olson, A. Allen, and P. C. Taylor, "Sound Velocity in liquid and glassy selenium", *Journal of Non-Crystalline Solids,* vol. 353, pp. 3254-3259, 2007.

[74]   W. Shockley, "Hot Electrons in Germanium and Ohm's law", *Bell System Technical Journal,* vol. 30, pp. 990-1034, 1951.

[75]   S. M. Sze and K. K. Ng, Physics of semiconductor devices, John Wiley and Sons, 2007.

[76]   K. Tanioka, J. Yamazaki, K. Shidara, K. Taketoshi, T. Kawamura, S. Ishioka*, et al.*, "An avalanche-mode amorphous selenium photoconductive layer for use as a camera tube target", *IEEE Electron Device Letters,* vol. 8, pp. 392-394, 1987.

[77]   K. Tsuji, T. Takasaki, T. Hirai, and K. Taketoshi, "Impact ionization process in amorphous selenium", *Journal of Non-Crystalline Solids,* vol. 114, p. 94, 1989.

[78]   A. Reznik, S. D. Baranovskii, O. Rubel, K. Jandieri, S. O. Kasap, Y. Ohkawa*, et al.*, "Avalanche multiplication in amorphous selenium and its utilization in imaging", *Journal of Non-Crystalline Solids,* vol. 354, pp. 2691-2696, 2008.

[79]   O. Rubel, S. D. Baranovskii, I. P. Zvyagin, P. Thomas, and S. O. Kasap, "Lucky-drift model for avalanche multiplication in amorphous semiconductors", *Physica Status Solidi C,* vol. 1, pp. 1186-1193, 2004.

[80] B. K. Ridley, "A model for impact ionisation in wide-gap semiconductors", *Journal of Physics C: Solid State Physics,* vol. 16, p. 4733, 1983.

[81] M. G. Burt, "An alternative expression for the impact ionization coefficient in a semiconductor derived using lucky drift theory", *Journal of Physics C: Solid State Physics,* vol. 18, p. L477, 1985.

[82] W. Shockley, "Problems related to p-n junctions in silicon", *Solid-State Electronics,* vol. 2, pp. 35-60, 1961.

[83] C. A. Lee, A. Logan, R. L. Batdorf, J. J. Kleimack, and W. Wiegmann, "Ionization Rates of Holes and Electrons in Silicon", *Physical Review,* vol. 134, p. 761, 1964.

[84] R. Chin, N. Holonyak, G. E. Stillman, J. Y. Tang, and K. Hess, "Impact Ionization in Multilayered Heterojunction Structures", *Electronics Letters,* vol. 16, pp. 467-469, 1980.

[85] C. R. Crowell and S. M. Sze, "Temperature Dependence of Avalanche Multiplication in Semiconductors", *Applied Physics Letters,* vol. 9, p. 242, 1966.

[86] V. I. Arkhipov and S. O. Kasap, "Is there avalanche multiplication in amorphous semiconductors?", *Journal of Non-Crystalline Solids,* vol. 266, pp. 959-963, 2000.

[87] S. O. Kasap, J. A. Rowlands, S. D. Baranovskii, and K. Tanioka, "Lucky drift impact ionization in amorphous semiconductors", *Journal of applied physics,* vol. 96, p. 2037, 2004.

[88] K. Koughia and S. O. Kasap, "Density of states of a-Se near the valence band", *Journal of Non-Crystalline Solids,* vol. 352, p. 1539, 2006.

[89] J. Berashevich, A. Mishchenko, and A. Reznik, "Two-step Photoexcitation Mechanism in Amorphous Se", *Physical Review Applied,* vol. 1, p. 034008, 2014.

[90]   M. Z. Kabir and N. Hijazi, "Temperature and field dependent effective hole mobility and impact ionization at extremely high fields in amorphous selenium", *Applied Physics Letters,* vol. 104, p. 192103, 2014.

[91]   A. Reznik, S. D. Baranovskii, O. Rubel, K. Jandieri, and J. A. Rowlands, "Photoconductivity in amorphous selenium blocking structures", *Physica Status Solidi C,* vol. 5, p. 790, 2008.

[92]   A. K. Bhatnagar, K. V. Reddy, and V. Srivastava, "Optical energy gap of amorphous selenium: effect of annealing", *Journal of Physics D: Applied Physics,* vol. 18, p. 149, 1985.

[93]   B. Vanhuyse, W. Grevendonk, G. J. Adriaenssens, and J. Dauwen, "Constant-dipole-matrix-element model for Faraday rotation in amorphous semiconductors", *Physical Review B,* vol. 35, p. 9298, 1987.

[94]   M. L. Benkhedir, M. Brinza, G. J. Adriaenssens, and C. Main, "Structure of the band tails in amorphous selenium", *Journal of Physics: Condensed Matter,* vol. 20, p. 215202, 2008.

[95]   M. Z. Kabir, S. O. Kasap, W. Zhao, and J. A. Rowlands, "Direct conversion X-ray sensors: Sensitivity, DQE & MTF", *IEE Proceedings - Circuits, Devices and Systems,* vol. 150, pp. 258-266, 2003.

[96]   A. Reznik, W. Zhao, Y. Ohkawa, K. Tanioka, and J. A. Rowlands, "Applications of avalanche multiplication in amorphous selenium to flat panel detectors for medical applications", *Journal of Materials Science: Materials in Electronics,* vol. 20, pp. 63-67, 2009.

[97]   S. Kasap, C. Koughia, J. Berashevich, R. Johanson, and A. Reznik, "Charge Transport in pure and stabilized amorphous selenium: re-examination of the density of states

distribution in the mobility gap and the role of defects", *Journal of Materials Science: Materials in Electronics,* vol. 26, pp. 4644-4658, 2015.

[98] M. Tachiya, "Breakdown of the Onsager theory of geminate ion recombination", *The Journal of Chemical Physics,* vol. 89, p. 6929, 1988.

[99] M. M. A. G. Jafar, M. H. Saleh, M. J. A. Ahmad, B. N. Bulos, and T. M. Al-Daraghmeh, "Retrieval of optical constants of undoped amorphous selenium films from an analysis of their normal-incidence transmittance spectra using numeric PUMA method", *Journal of Materials Science: Materials in Electronics,* vol. 27, p. 3281, 2016.

[100] L. Onsager, "Initial recombination of ions", *Physical Review,* vol. 54, p. 554, 1938.

[101] M. Wojcik and M. Tachiya, "Accuracies of the empirical theories of the escape probability based on Eigen model and Braun model compared with the exact extension of Onsager theory", *The Journal of Chemical Physics,* vol. 130, p. 104107, 2009.

[102] K. Falkowski, W. Stampor, P. Grygiel, and W. Tomaszewicz, "Sano-Tachiya-Noolandi-Hong versus Onsager modelling of charge photogeneration in organic solids", *Chemical Physics,* vol. 392, p. 122, 2012.

[103] J. Mort, "Geminate and non-geminate recombination in amorphous semicondcutors", *Journal de Physique Colloques,* vol. 42, pp. C4-433-C4-441 1981.

[104] W. Que, "Onsager theory of geminate recombination: A single series expansion", *Canadian Journal of Physics,* vol. 73, p. 248, 1995.

[105] J. Noolandi and K. M. Hong, "Theory of photogeneration and fluorescence quenching", *The Journal of Chemical Physics,* vol. 70, p. 3230, 1979.

[106] R. Kirkin, V. V. Mikhailin, and A. N. Vasil'ev, "Recombination of correlated electron-hole pairs with account of hot capture with emission of optical phonons", *IEEE Transactions on Nuclear Science,* vol. 59, pp. 2057-2064, 2012.

[107] J. C. Scott and G. Malliaras, "Charge injection and recombination at the metal-organic interface", *Chemical Physics Letters,* vol. 299, pp. 115-119, 1999.

[108] S. M. Arnab and M. Z. Kabir, "An analytical model for analyzing the current-voltage characteristics of bulk heterojunction organic solar cells", *Journal of applied physics,* vol. 115, p. 034504, 2014.

[109] M. Lundstrom, Fundamentals of Carrier Transport, Cambridge University Press, 2009.

[110] U. Neitzel, I. Maack, and S. Gunther-Kohfahl, "Image quality of a digital chest radiography system based on a selenium detector", *Medical Physics,* vol. 21, pp. 509-516, 1994.

[111] G. Jaffe, "Zur Theorie der Ionisation in Kolonnen," *Annalen der Physik (Leipzig),* vol. 42, p. 303, 1913.

[112] H. A. Kramers, "On a modification of Jaffe's Theory of Column-Ionization", *Physica,* vol. 18, pp. 665-675, 1952.

[113] C. Haugen and S. O. Kasap, "Langevin recombination of drifting electrons and holes in stabilized a-Se (Cl-doped a-Se: 0.3 % As)", *Philosophical Magazine,* vol. 71, pp. 91-96, 1995.

[114] M. Z. Kabir, E. V. Emelianova, V. I. Arkhipov, M. Yunus, G. Adriaenssens, and S. O. Kasap, "The effects of large signals on charge collection in radiation detectors: Application to amorphous selenium detectors", *Journal of applied physics,* vol. 99, p. 124501, 2006.

[115]   E. V. Emelianova, N. Qamhich, M. Brinza, G. J. Adriaenssens, S. O. Kasap, R. E. Johanson*, et al.*, "Density of localized states and charge carrier photogeneration in amorphous selenium", *Journal of Non-Crystalline Solids,* vol. 215, pp. 326-327, 2003.

[116]   M. Z. Kabir, "Effects of charge carrier trapping on polycrystalline PbO X-ray imaging detectors", *Journal of applied physics,* vol. 104, p. 074506, 2008.

[117]   N. Hijazi and M. Z. Kabir, "Modeling of Columnar recombination for high-energy photon generated electrons and holes in amorphous selenium", *Journal of Material Science: Materials in Electronics,* vol. 28, pp. 7036-7041, 2017.

[118]   G. Juska and K. Arlauskas, "Properties of Hot carriers in a-Si:H in comparison to a-Se", *Solid State Phenomena,* vol. 44-46, pp. 551-558, 1995.

[119]   M. F. Stone, W. Zhao, B. V. Jacak, P. O'Connor, B. Yu, and P. Rehak, "The x-ray sensitivity of amorphous selenium for mammography", *Medical Physics,* vol. 29, pp. 319-324, 2002.

[120]   S. M. Arnab and M. Z. Kabir, "Impact of Charge Carrier Trapping on Amorphous Selenium Direct Conversion Avalanche X-ray Detectors", *Journal of Applied Physics,* vol. 112, p. 134502, 2017.

[121]   S. M. Arnab and M. Z. Kabir, "Impact of Lubberts Effect on Amorphous Selenium Indirect Conversion Avalanche Detector for Medical X-ray Imaging", *IEEE Transaction on Radiation and Plasma Medical Sciences,* vol. 1, pp. 221-228, 2017.

[122]   O. Semeniuk, O. Grynko, G. Juska, and A. Reznik, "Amorphous lead oxide (a-PbO): suppression of signal lag via engineering of the layer structure", *Scientific Reports,* vol. 7, 2017.

[123] O. Semeniuk, O. Grynko, G. Decrescenzo, G. Juska, K. Wang, and A. Reznik, "Characterization of polycrystalline lead oxide for application in direct conversion X-ray detectors", *Scientific Reports,* vol. 7, 2017.

[124] Y. C. Kim, K. H. Kim, D. Y. Son, D. N. Jeong, J. Y. Seo, and Y. S. Choi, "Printable organometallic perovskite enables large area, low dose X-ray imaging", *Nature,* vol. 550, 2017.

List of Publications

A) Referred Journals Papers

1. Nour Hijazi, D. Panneerselvam, M. Z. Kabir, "Electron-hole pair creation energy in amorphous selenium for high energy photon excitation**",** Journal of Materials Science: Materials in Electronics-in press, 2017.

2. Nour Hijazi and M. Z. Kabir, "Modeling of Columnar recombination for high-energy photon generated electron-holes: application to amorphous selenium", Journal of Materials Science: Materials in Electronics, vol. 28, pp.7036-7041, 2017.

3. Nour Hijazi and M. Z. Kabir, "Mechanisms of charge photogeneration in amorphous selenium under high electric fields", Journal of Material Science: Materials in Electronics, vol. 27, pp.7534-7539, 2016.

4. N. Hijazi and M. Z. Kabir, "Mechanisms of temperature and field-dependent effective drift mobilities and impact ionization coefficients in amorphous selenium", Canadian Journal of Physics, vol. 93 (11), pp. 1407-1412, 2015.

5. M. Z. Kabir and N. Hijazi, "Temperature and field dependent effective hole mobility and impact ionization at extremely high fields in amorphous selenium", Applied Physics Letters, vol. 104, pp. 192103, 2014.

B) Referred Conference Papers

1. Nour Hijazi, D. Panneerselvam, M. Z. Kabir, "Modeling of electron hole pair creation energy for high energy photons in amorphous selenium"**,** CSSTC, Waterloo, Aug. 20-24, 2017.

2. N. Hijazi and M. Z. Kabir, "Modeling of Columnar recombination for high energy photon generated electron-holes: application to amorphous selenium", *ICOOPMA*, Montreal, June 13-17, 2016.

3. N. Hijazi and M. Z. Kabir, "Modeling of Temperature and Field Dependent Effective Hole Mobility at High Fields in Amorphous Selenium", Proc. IEEE Nuclear Science Symposium and Medical Imaging Conference, 2014.

C) Non-referred Conference Presentation

1. N. Hijazi and M. Z. Kabir, "Charge carrier transport and photogeneration at very high electric fields in amorphous selenium", *ECE-GSRC*, Concordia University, Montreal, 13, 2017.

Appendix A: Noolandi and Hong model formulation

Noolandi and Hong [105] generalized Onsager's model calculation of the geminate recombination probability to include the boundary condition of a partly absorbing sphere of finite radius at the origin. This solution was used to formulate a model of photogeneration and fluorescence quenching in organic solids. Noolandi and Hong obtained a formulation of the generalized escape probability defined by

$$R(r,\mu) = \frac{1}{\sqrt{r}} e^{(1/2)w(r,\mu)} \sum_{l=0}^{\infty} \beta_l z_{2l}(r) T_1)(\mu) \tag{A.1}$$

where $W(r, \mu)$ is the Wronskian of r and μ, and $\beta_l Z_{2l}$ is defined by

$$\sum_{l=0}^{\infty} \beta_l Z_{2l}(a)\{[\frac{z'_{2l}(a)}{z'_{2l}(a)} + \frac{1}{a^2} - \frac{1}{2a} - \frac{v_r}{D}]\delta_{lm} - \frac{F}{2} A_{lm}$$

$$= -\frac{v_r}{D} \frac{(2\pi)^{1/2}}{N_m} [T_m(1)(\frac{2}{F})^{1/2} Z_{1m}(a) + 2a_{m0} Z_{2m}(a)]\} \tag{A.2}$$

$$(m = 0,1,2,...)$$

The matrix element A_{lm} is defined by

$$A_{lm} = \int_{-1}^{1} d\mu \mu T_1(\mu) T_m(\mu) = 2\sum_{k=0}^{\infty} \frac{k+1}{(2k+1)(2k+3)} (a_{1k} a_{mk+1} + a_{1k+1} a_{mk}) \tag{A.3}$$

where $T_1(\mu)$ is the generalized Legendre function of l order defined by

$$T_1(\mu) = \sum_{n=0}^{\infty} a_{ln} P_n(\mu) = \sum_{n=0}^{\infty} a'_{ln} (\frac{2n+1}{2})^{1/2} P_n \tag{A.4}$$

$$a_{ln} = (\frac{2n+1}{2})^{1/2} a'_{ln}$$

where $a_{l,0}$ are the coefficients of the expansion of T_l functions expanded into series of Legendre polynomials and $[(2n+1)/2]^{1/2} P_n(\mu)$ are the orthonormalized Legendre polynomials. The coefficients a_{ln} can be obtained by diagonalization of matrix A whose elements are given by

$$A_{mn} = \frac{-m}{\sqrt{(2m-1)(2m+1)2}} \frac{F}{2}, n = m-1$$

$$A_{mn} = m(m+1), n = m$$

$$A_{mn} = \frac{-(m+1)}{\sqrt{(2m+1)(2m+3)}} \frac{F}{2}, n = m+1$$

$$A_{mn} = 0, otherwise$$

(A.5)

Appendix B: Numerical Model Simulation Setup

In the study of the investigation of possible physical mechanisms of X-ray generated free electron-hole pair creation energy in amorphous selenium at high electric field, it is important to compare the proposed analytical model by simulating the carrier continuity equations of the two charged species considering carrier drift, diffusion and bimolecular recombination between non-geminate electrons and holes. Only the case where the electric field is parallel to the column axis is considered in this work.

The simulation work was performed based on COMSOL MULTIPHYSICS 5.2 software, where the work was divided into three parts:

1. Finding the carrier concentrations of both electrons and holes by solving a system of two partial differential equations (PDE).
2. Finding the total number of holes that escaped the columnar recombination.
3. Finding the electron hole pair creation energy.

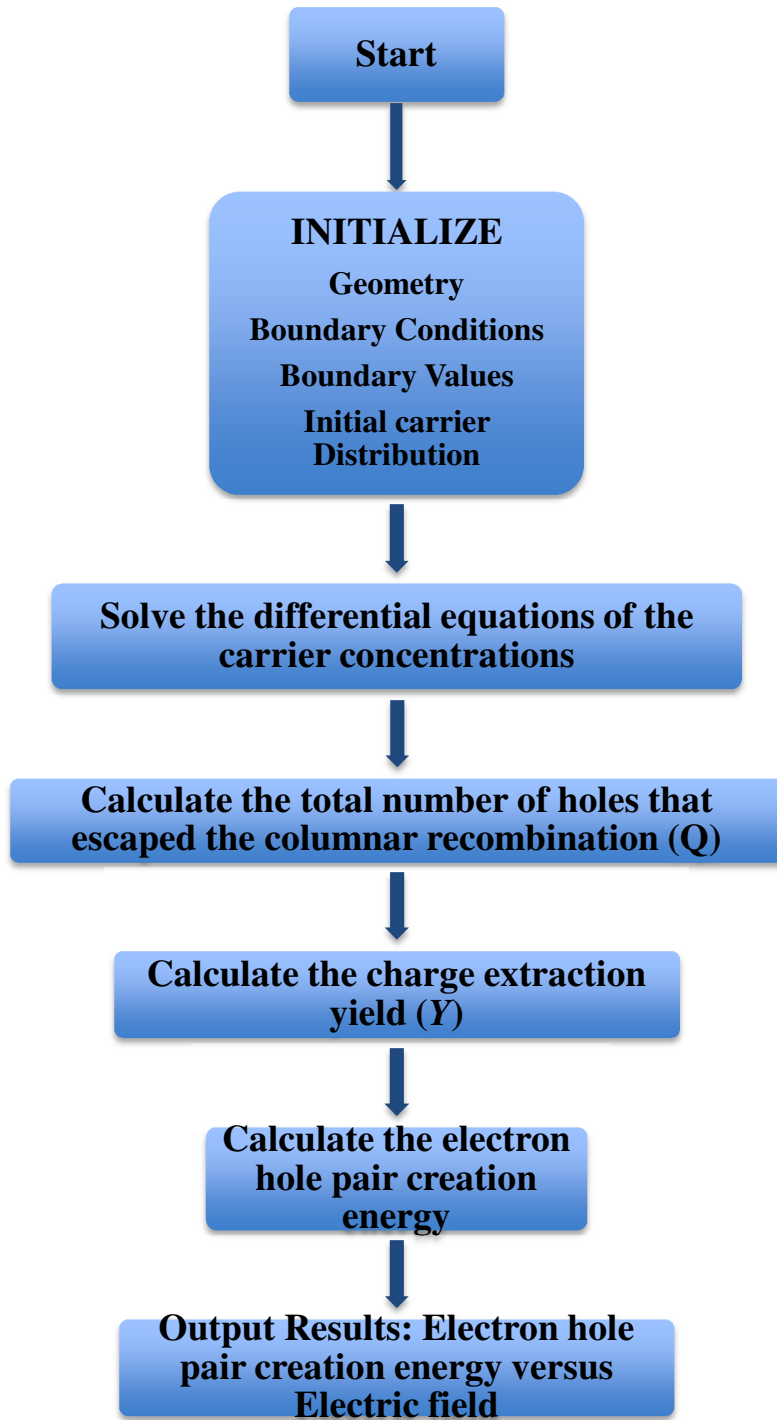The flowchart in Figure B-1 summarizes the solution procedure.

Figure B- 1 Electron hole pair creation energy based on carrier continuity equations Scheme Flowchart.

The settings for the parameters and variables are given in Table B-1 and Table B-2, respectively.

Table B- 1 Parameters

Name		Expression	Value
F	Electric Field	100e4[V/cm]	1E8 V/m
k	Boltzmann Constant	8.6174e-5[eV/K]	1.3807E−23 J/K
T	Temperature	293[K]	293 K
b_g	Radius of the cylinder	1.55e-6[cm]	1.55E−8 m
N_0	Ionization line density	3e7[1/cm]	3E9 1/m
r	Radius of the Gaussian distribution	1.55e-6[cm]	1.55E−8 m
d	Column length	10^ - 5[cm]	1E−7 m
C_0	Constant	5e-8[cm^3/s]	5E−14 m³/s
epsi	Permitivity of the photoconductor	6.3*8.854*1e-14[F/cm]	5.578E−11 F/m
q	Elementary charge	1.6*1E-19[C]	1.6E−19 C
muh_a	Coefficient of empirical hole mobility equation	0.127[cm^2/V/s]	1.27E−5 m²/(V·s)
muh_b	Coefficient of empirical hole mobility equation	0.745[cm^2/V/s]	7.45E−5 m²/(V·s)
muh_c	Coefficient of empirical hole mobility equation	48[V/um]	4.8E7 V/m
muh_d	Coefficient of empirical hole mobility equation	11.5[V/um]	1.15E7 V/m
mue_a	Coefficient of empirical electron mobility equation	0.004[cm^2/V/s]	4E−7 m²/(V·s)
mue_b	Coefficient of empirical electron mobility equation	0.13[cm^2/V/s]	1.3E−5 m²/(V·s)
mue_c	Coefficient of empirical electron mobility equation	110[V/um]	1.1E8 V/m
mue_d	Coefficient of empirical electron mobility equation	20[V/um]	2E7 V/m
L	Layer thickness	10^ - 5[cm]	1E−7 m
W_0	Average X-ray energy to	7[eV]	1.1215E−18 J

Name		Expression	Value
	create an EHP		
muh_F	Field dependent effective hole mobility	muh_a +(muh_b/(1+ exp(-(F- muh_c)/muh_d)))	8.6399E−5 m²/(V·s)
t_0	Initial transit time	d/(muh_F*F)	1.1574E−11 s

Table B- 2 Variables

Name	Description	Expression	Unit
De	Diffusion coefficient of electrons	mue(F)*k*T/q	m²/s
Dh	Diffusion coefficient of holes	muh(F)*k*T/q	m²/s
C_L	Langevin recombination coefficient	q*(mue(F) + muh(F))/epsi	m³/s
C_r	Recombination coefficient	(C_L*C0)/(C_L + C0)	m³/s
n0	Initial charge carriers	N0*exp(-(r1/(b^2)))/(pi*b^2)	1/m³
r1	Two dimensional radius	x^2 + y^2	m²
Qn	Collected charge of electrons	intg(n)	
Qp	Collected charge of holes	intg(p)	

The differential equations were set under the option of Mathematics, Coefficient from PDE (one for electrons and one for holes). Tables B-3 and B-4 summarize the settings of the coefficients equations respectively for electrons and holes.

Table B- 3 Settings of Coefficients PDE equation for electrons

$$e_a \frac{\partial^2 n}{\partial t^2} + d_a \frac{\partial n}{\partial t} + \nabla.(-c\nabla n - \alpha n + \gamma) + \beta.\nabla n + an = f$$

$$\nabla = [\frac{\partial}{\partial x}, \frac{\partial}{\partial y}, \frac{\partial}{\partial z}]$$

Description	Value
Diffusion coefficient	{{De, 0, 0}, {0, De, 0}, {0, 0, De}}
Absorption coefficient	C_r*p
Source term	0
Mass coefficient	0
Damping or mass coefficient	1
Conservative flux convection coefficient	{0, 0, 0}
Convection coefficient	{0, 0, -mue(F)*F}
Conservative flux source	{0, 0, 0}

Table B- 4 Settings of coefficients PDE equation for holes

$$e_a \frac{\partial^2 p}{\partial t^2} + d_a \frac{\partial p}{\partial t} + \nabla.(-c\nabla p - \alpha p + \gamma) + \beta.\nabla p + ap = f$$

$$\nabla = [\frac{\partial}{\partial x}, \frac{\partial}{\partial y}, \frac{\partial}{\partial z}]$$

Description	Value
Diffusion coefficient	{{Dh, 0, 0}, {0, Dh, 0}, {0, 0, Dh}}
Absorption coefficient	C_r*n
Source term	0
Mass coefficient	0
Damping or mass coefficient	1
Conservative flux convection coefficient	{0, 0, 0}
Convection coefficient	{0, 0, muh(F)*F}
Conservative flux source	{0, 0, 0}